1-1-2012

Evidence-Based Uncertainty Modeling of Constitutive Models with Application in Design Optimization

Shahabedin Salehghaffari

EVIDENCE-BASED UNCERTAINTY MODELING OF CONSTITUTIVE MODELS WITH APPLICATION IN DESIGN OPTIMIZATION

By

Shahabedin Salehghaffari

A Dissertation
Submitted to the Faculty of
Mississippi State University
in Partial Fulfillment of the Requirements
for the Degree of Doctor of Philosophy
in Computational Engineering
in the Bagely College of Engineering

Mississippi State, Mississippi

May 2012

EVIDENCE-BASED UNCERTAINTY MODELING OF CONSTITUTIVE MODELS

WITH APPLICATION IN DESIGN OPTIMIZATION

By

Shahabedin Salehghaffari

Approved:

Masoud Rais-Rohani Professor of Aerospace Engineering (Director of Dissertation)	Douglas J. Bammann Professor of Mechanical Engineering (Committee Member)
Esteban B. Marin Research Professor (Committee Member)	Tomasz Haupt Research Associate Professor (Committee Member)
Seth F. Oppenheimer Professor of Mathematics and Statistics (Committee Member)	Roger King Graduate Coordinator of Computational Engineering

Sarah A. Rajala
Dean of the Bagley College of Engineering

Name: Shahabedin Salehghaffari

Date of Degree: May 12, 2012

Institution: Mississippi State University

Major Field: Computational Engineering

Major Professor: Masoud Rais-Rohani

Title of Study: EVIDENCE-BASED UNCERTAINTY MODELING OF CONSTITUTIVE MODELS WITH APPLICATION IN DESIGN OPTIMIZATION

Pages in Study: 146

Candidate for Degree of Doctor of Philosophy

Phenomenological material models such as Johnson-Cook plasticity are often used in finite element simulations of large deformation processes at different strain rates and temperatures. Since the material constants that appear in such models depend on the material, experimental data, fitting method, as well as the mathematical representation of strain rate and temperature effects, the predicted material behavior is subject to uncertainty. In this dissertation, evidence theory is used for modeling uncertainty in the material constants, which is represented by separate belief structures that are combined into a joint belief structure and propagated using impact loading simulation of structures. Yager's rule is used for combining evidence obtained from more than one source. Uncertainty is quantified using belief, plausibility, and plausibility-decision functions. An evidence-based design optimization (EBDO) approach is presented where the non-deterministic response functions are expressed using evidential reasoning. The EBDO approach accommodates field material uncertainty in addition to the embedded uncertainty in the material constants. This approach is applied to EBDO of an externally stiffened circular tube under axial impact load with and without consideration of material

field uncertainty caused by spatial variation of material uncertainties due to manufacturing effects. Surrogate models are developed for approximation of structural response functions and uncertainty propagation. The EBDO example problem is solved using genetic algorithms. The uncertainty modeling and EBDO results are presented and discussed.

ACKNOWLEDGEMENTS

I would like to thank Dr. Masoud Rais-Rohani for his assistance and guidance toward successful completion of this dissertation. Also, I would like to thank Dr. Marin and Dr. Bammann for their technical advice on the plasticity models and Dr. Haupt and Dr. Oppenheimer for their helpful comments on the dissertation. Supports provided by Center for Advance Vehicular Systems (CAVS) and Aerospace Engineering Department at Mississippi State University are gratefully acknowledged. Also, the funding provided for this research by the NSF under Grant No. 0826547 is gratefully acknowledged.

TABLE OF CONTENTS

LIST OF TABLES

LIST OF FIGURES

FIGURE Page

CHAPTER I

INTRODUCTION

Research efforts in hierarchical modeling of process-structure-property relations have resulted in more sophisticated physics-based material models with the ability to characterize the evolution of material microstructure under a prescribed loading history. Such models are intended to enhance the response predictions of solids experiencing large inelastic deformations. With growing reliance on computational design of complex structures and limited physical testing, there is a greater need for inclusion of advanced material models with better predicative capabilities. However, reliance on these material models must be coupled with accurate modeling of the uncertainties in both the model predictions as well as in simulation results. Some of the formidable research challenges associated with the application of phenomenological and multiscale material models in a computational design framework include 1) uncertainty quantification of material models with consideration of both aleatory and epistemic uncertainties; 2) proper integration of advanced material models to simulate large deformation of structures; and 3) development of non-deterministic approaches and solution strategies for design optimization of complex systems in presence of uncertainty (Oden et al., 2006).

The objective of this dissertation is twofold: 1) to apply the principles of evidence theory to generate a more comprehensive representation, propagation, and measurement of uncertainty in constitutive models that emanate from lack of knowledge/insufficient data (epistemic uncertainty), inherent variability in material characteristics (aleatory

uncertainty), or formulations used for mathematical modeling of material behavior in the constitutive model (model-selection uncertainty), and 2) to advance the state-of-the-art in engineering design through development, application, and assessment of an evidence-based computational framework for uncertainty quantification and design optimization of structures with advanced material models. The main contributions of this dissertation are as follows:

- Development of a general uncertainty representation framework for construction of belief structures based on the available data on uncertain parameters. This includes the determination of agreement, conflict, and ignorance relationships among the intervals for basic belief assignment.
- Development of a metamodel-based approach for efficient propagation of uncertainties using a limited number of computationally expensive finite element simulations.
- Development of a new aggregation rule of evidence capable of dealing with conflict and ignorance between different information sources based on the available observations. The aggregation rule can be adopted to address model-selection uncertainty. It can be also adopted in uncertainty representation level where different information sources suggest different belief structures.
- Application of evidence theory for representation and modeling of field uncertainty in consideration of spatial variability in material properties due to manufacturing and material microstructure.
- Development and application of a computational tool for Evidence-Based Design Optimization (EBDO) of structures with consideration of all sources of material uncertainty.

- Development of a new physics-guided approach for fitting the material constants of advanced plasticity models with experimental stress-strain curves and determination of the uncertainties in the model constants.

1.1 Dissertation structure

This dissertation is organized into nine chapters. Figure 1.1 shows the flowchart of the evidential framework for uncertainty quantification of constitutive material models and application to optimization of structures under material model uncertainty. The flowchart offers a general layout of the process used for uncertainty modeling of constitutive models for polycrystalline ductile metals. Different aspects of this diagram are addressed in different chapters of this dissertation.

In Chapter 2, an overview of evidence theory is presented first and then a methodology for representation, propagation and measurement of uncertainty is presented. For representation of uncertainty, a methodology to construct belief structures in interval forms with assigned degree of belief based on available information on uncertain parameters is provided. Then, an approach for propagation of uncertainty is presented. This includes construction of a joint belief structure required for uncertainty propagation of a system response with dependence on multiple uncertain variables which is obtained by the Cartesian product of the belief structures of all uncertain variables. Furthermore, construction of a field joint belief structure to accommodate possible spatial variation of material properties that may considerably impact product performance is discussed. Then, a methodology based on design and analysis of computer experiments is used to reduce the computational complexity associated with uncertainty propagation. As shown in Figure 1.1, uncertainty measures (belief and plausibility) can be assessed for the sake of uncertainty

quantification (measurement) through comparison of the calculated propagated belief structure and the belief structure of structural response determined using all the available evidence (experimental, analytical and numerical).

In chapter 3, mathematical formulations of Johnson-Cook (JC) and Bammann-Chiesa-Johnson (BCJ) plasticity models are presented. Also, a new physics-guided numerical fitting approach for determination of the material constants of BCJ plasticity model is suggested.

In chapter 4, the methodology presented in chapter 2 is employed for uncertainty representation of two phenomenological plasticity models: (1) JC and (2) BCJ.

In chapter 5, the methodology presented in chapter 2 is applied for uncertainty propagation of JC and BCJ plasticity models through nonlinear transient dynamic finite element simulations of a thin-walled circular aluminum alloy (AA6061-T6) tube under axial impact load.

When faced with information or data from multiple sources of evidence, it is possible to encounter diverse belief structures. Since uncertainty can be represented and quantified only by a single belief structure, it is necessary to aggregate the body of evidence. This task becomes very challenging when information sources are in conflict. As shown in Figure 1.1, the aggregation of evidence appears in both uncertainty representation level, where there are multiple sources of experimental data, as well as uncertainty propagation level, where multiple formulations of constitutive models is suggested for simulation of large deformation processes. Chapter 6 aims to address this issue by development of a new aggregation rule of evidence that makes use of experimental observations or decision-making methods for determination of credibility factor of evidence (CFE) for conflicting evidence from different information sources. The

proposed aggregation rule is adopted for uncertainty modeling of a large deformation process represented by the Taylor impact test for which JC and Zerilli-Armstrong (ZA) plasticity models provide different answers.

The computational framework for optimization of structures under material form uncertainty using mathematical tools of evidence theory is discussed in chapter 7. A general optimization formulation for EBDO is suggested. This chapter discusses how the developed methodologies for uncertainty modeling of plasticity models can be adopted for assessment of evidence-based constraints. From the computational point of view, chapter 7 explains interactions between developed computational codes for uncertainty representation, propagation, quantification as well as optimization of structures under material form uncertainty. Computational framework for construction of a field joint belief structure to accommodate possible spatial variation of material properties that may considerably impact product performance is discussed in chapter 7 as well.

EBDO of externally stiffened crush tubes using the developed computational framework is presented in chapter 8. Optimization results of stiffened tubes under material form uncertainty with and without consideration of material field uncertainty is also provided.

Chapter 9 summarizes the work performed in this research. Recommendations for future research are also presented.

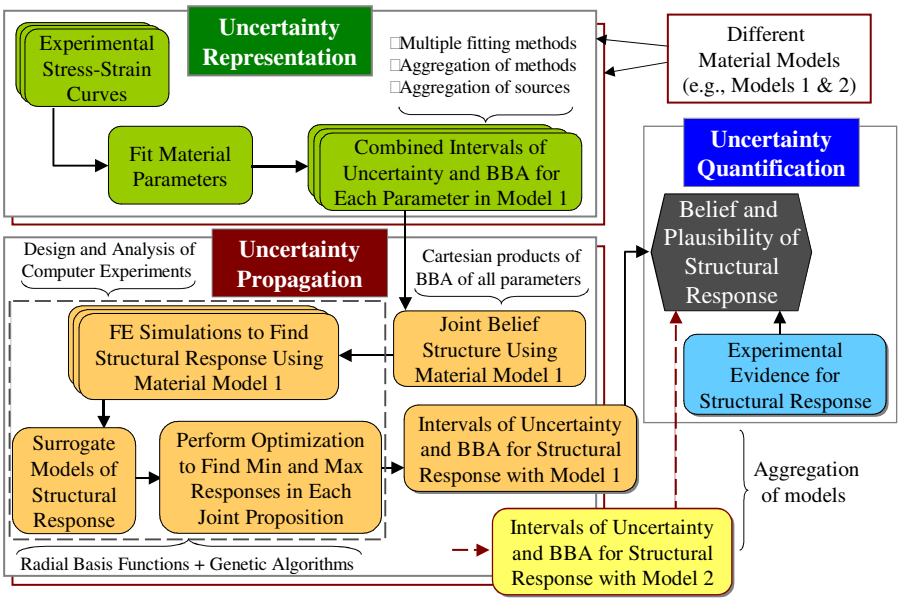

Figure 1.1 General framework for representation, propagation, and quantification of uncertainty in material models

1.2 Literature review

There are several plasticity and coupled plasticity-damage models for the macroscale (continuum) simulations of ductile solids and structures experiencing large inelastic deformation at high strain rates and temperatures. Simple *empirical phenomenological* models such as the power law, Johnson-Cook (JC) (Johnson and Cook, 1983) and modified Johnson-Cook (Holmquist and Johnson, 1991) models, as well as *physically-motivated* models, such as Zerilli-Armstrong (ZA) (Zerilli and Armstrong, 1987) and Usui (Shirakashi *et al.*1983) models, have been developed mainly for ease of computational implementation. These are *equation-of-state* models that represent the flow stress as a unique function of total strain, strain rate, and temperature, independent of the loading path. However, the addition of history dependent variables (internal state variables) is necessary to represent more accurately the material behavior, and, hence, improve the predictive capability of the simulations. These variables represent the current

state of the material, which includes strain rate and temperature history effects as well as coupling of rate- and temperature-dependence with material hardening. These models are considered *physics-based* (or microstructure-based) as they establish a direct relation between microstructure features (e.g., particle size variation and spatial distribution) and macroscopic behavior. Physics-based models include Mechanical Threshold Stress (MTS) (Follansbee and Kocks, 1988), Bammann-Chiesa-Johnson (BCJ) (Bammann, 1984; Bammann *et al.,* 1996), BCJ-damage (Horstemeyer, 2001), and Evolving Microstructural Model of Inelasticity (EMMI) (Marin *et al*., 2006).

Although all cited categories of models are quite diverse in their formulations and modeling capabilities, they share a common thread in their use of fitting parameters (constants) that in some cases (e.g., BCJ-damage) could approach nearly forty. These parameters, of course, take different values for different materials and associated alloys. The calculation of these parameters for any specific material requires a number of experiments on material specimens under different boundary conditions, strain rates and temperatures. Often, there is scarcity of data. Coupled with alternative methods for fitting the parameters and variations in the way certain terms (e.g., homologous temperature, dislocation hardening) are formulated in the material model, the resulting values for the parameters can change. In some instances, there could be a wide variation in one or more parameters, which leads to considerable uncertainty in the results of design analysis and optimization of structural systems based on these models.

In a recent Los Alamos National Lab study, Gray *et al.* (1994) examined both JC and ZA constitutive models and among their conclusions they mention "*One lesson that we learned here was that by fitting the JC model using a different range of data we could obtain quite different model constants*." Since simulation-based design and analysis of

structures rely on accurate constitutive models for prediction of material behavior, uncertainties in material models can lead to increased risk to the safety of the designed system.

Recent investigations (Helton, 1994, 1997; Oberkampf *et al.*, 2001) have noted the importance of distinguishing between variability (aleatory uncertainty) that originates from randomness inherent in the system (e.g., material mircrostructure) and incertitude (epistemic uncertainty) that arises from lack of data or insufficient knowledge (e.g., vagueness, ignorance) about the system. While epistemic uncertainty can be reduced by acquisition of additional data or knowledge, aleatory uncertainty cannot. Probability theory offers all the necessary tools for accurate representation and propagation of aleatory uncertainty. However, it is not equipped to accurately model epistemic uncertainty because it cannot properly account for ignorance. Attempts to lump aleatory and epistemic uncertainties together can lead to inaccurate estimation of true uncertainty in the system. (Oberkampf *et al.,* 2001, 2004)

Recent researches in computational design under uncertainty have employed different approaches to represent and propagate aleatory uncertainties in constitutive models (Rais-Rohani et al., 2010; Acar et al., 2010a; Solanki et al., 2009, 2010; Acar et al., 2009).

Evidence theory offers a general framework for separate modeling of epistemic and aleatory uncertainties that can be used in phenomenological material models of varying complexity. However, uncertainty representation and propagation under evidence theory are very different from and often more computationally intensive than the traditional probability theory. Its practical application to complex engineering systems is hampered by a number of challenges such as the lack of a systemic approach

for calculation of basic belief assignment for different propositions (pieces of evidence) in the frame of discernment, no unified approach for aggregation of evidence collected from different sources with varying degrees of conflict and ignorance, and the computational cost associated with uncertainty propagation in presence of high fidelity computer simulations involving non-monotonic responses.

Agarwal et al. (2004) employed surrogate models to generate continuous functions of uncertainty measures in evidence theory. Bae et al. (2004a) adopted the multi-point approximation (MPA) approach to reduce the computational cost of uncertainty propagation and quantification by focusing the computational resources on the failure domain instead of the whole design area. The focus of these limited number of studies have been primarily on propagation of uncertainties in simple systems or benchmark problems based on the assumed belief structure. However, uncertainty propagation of a complex physical system with a complicated belief structure and mathematical formulations is very computationally expensive and needs a cost-effective methodology capable of reducing the overall computational costs.

In the domain of design optimization under uncertainty, several approaches have been developed for mathematical modeling of uncertainty in design based on theory of probability, classical set, fuzzy set, fuzzy measure (evidential reasoning), and rough set (Klir, 1994); in these approaches, uncertainty is described in terms of likelihood of an event occurrence in a universal set of events, non-specificity inherent in each set of mutually exclusive alternatives, vagueness from imprecision of the conditions for the membership of an element into a set, plausibility and belief measures due to insufficient information, and imprecise representation of a crisp set, respectively.

With the rapidly growing interest in non-deterministic design approaches over the past two decades, we have seen the immergence of probabilistic design and reliability-based design

optimization (RBDO) as principal frameworks for decision-making and design optimization under uncertainty. In the case of aleatory uncertainty with individual random variables following any standard probability distribution function (sufficient data and knowledge), probability theory can be used to calculate fairly accurately failure probability for a single or multiple events.

Based on probabilistic definition of random variables and associated responses, an RBDO problem seeks to minimize an objective function $f(\boldsymbol{X},\boldsymbol{Y})$ subject to a set of probabilistic constraints in the form $P_{f_i} = P\left[G_i(\boldsymbol{X},\boldsymbol{Y}) \le 0\right] \le P_{a_i};\ i = 1, N_p$, side constraints on design variables $Y_k^l \le Y_k \le Y_k^u; k = 1, NDV$ with $\boldsymbol{X} = \{X_1, X_2, ..., X_n\}^T$ as vector of random variables. With failure probability analysis as a major challenge, multiple ways of formulating and solving an approximate RBDO problem have been developed (Enevoldsen and Sorensen, 1994; Frangopol, 1995; Tu et al., 1999; Du and Chen, 2004; Qu and Haftka, 2004; Rahman et al., 2004; Rais-Rohani and Xie, 2005;Rais-Rohani et al., 2010). Regardless of the approach, the solution of an RBDO problem is considerably more expensive than in deterministic (risk-ignoring) design optimization.

Recently, the application of RBDO methodology was extended to product design optimization using BCJ-damage material model (Solanki et al. 2010). By modeling the stochastic uncertainties in the material model and the loading conditions, the RBDO problem for a cast aluminum component was solved using the nested reliability index approach. The comparison of results with those based on linear piecewise plasticity model showed the importance of damage as a failure criterion and the effect of uncertainty in microstructure-based material on optimum design.

Recent advances in non-deterministic design approaches include the use of fuzzy measures in what is known as possibility-based design optimization (PBDO) (Nikolaidis *et al*. 2004; Choi *et al*. 2004). He and Qu (2008) compare PBDO and EBDO with RBDO

and conclude that generally the results found by EBDO tend to be more conservative than those based on PBDO and RBDO. As noted by Nikolaidis et al. (2004), possibility can be less conservative than probability in the context of risk assessment of systems with multiple failure modes (series system). The conservatism of possibility over probability is seen mainly in parallel systems (simultaneous occurrence of multiple failure modes). Due to its use of evidence theory, EBDO can address conflict in data or expert opinions whereas PBDO cannot. Thus, EBDO represents a powerful framework for design optimization under uncertainty due to lack of knowledge, insufficient data, or conflict in available evidence. It is worth noting that RBDO, PBDO, and EBDO represent completely different design philosophies, and for a general constrained design optimization problem, they yield different answers.

Recent applications of EBDO include the works of Agarwal et al. (2004), Mourelatos and Zhou (2006), and Alyanak et al. (2008). The optimization problem can be broadly described as an RBDO problem shown above but with design constraints cast in terms of belief, plausibility, plausibility-decision functions or uncertainty (i.e., plausibility – belief). Since constraints are typically imposed on limit states or failure conditions, a plausibility or plausibility-decision formulation would require less calculation than belief function evaluation. This is because the failure domain for each active constraint is usually smaller than the safe domain over the frame of discernment (Mourelatos and Zhou, 2006). As an example, constraints on failure plausibility in EBDO can be cast as $Pl\{G_i(\boldsymbol{X},\boldsymbol{Y})\le 0\}\le Pl_{a_i}$, where $G_i(\boldsymbol{X},\boldsymbol{Y})\le 0$ represents a failure criterion.

CHAPTER II

UNCERTAINTY MODELING FRAMEWORK USING EVIDENCE THEORY

Here, after a short review of the mathematical tools of evidence theory and aggregation rules of evidence, an evidential framework for modeling all aspects of uncertainty quantification (i.e., uncertainty representation, propagation and measurement) is provided. The uncertainty quantification framework will be adapted in the subsequent chapters to model uncertainty of plasticity models.

2.1 Evidence theory: basic principles and concepts

Evidence theory provides an alternative to the traditional probability theory by allowing less restrictive statements in representing uncertainty. Much of the fundamental work in this area was done by Dempster (1968) and Shafer (1976). A brief overview of evidence theory is provided in this section. However, for a more thorough description, the reader is referred to Yager (1967, 1967a).

Let X represent a set of elements. The power set $P(X)$ is the set of all possible subsets of X including the empty set. For example, if $X = \{a, b\}$, then $P(X) = \{\emptyset, \{a\}, \{b\}, X\}$. Evidence theory assigns a basic belief to each element of $P(X)$. Formally, $m: P(X) \rightarrow [0, 1]$ is called a basic belief assignment (BBA) or basic probability assignment (BPA) function with two properties: 1) basic belief of the empty set is zero: $m(\emptyset) = 0$, and 2) basic beliefs of the remaining members of the power set add up to 1: $\sum_{A \in P(X)} m(A) = 1$. Any subset x of X with non-zero BBA is called a focal element and represents the available belief or evidence that supports it. More formally, the BBA

function $m(x)$ of a given member of $P(X)$ expresses the proportion of all relevant and available evidence that supports the claim that the actual state belongs to *x* but not to any particular subset of $P(X)$. The value of $m(x)$ pertains only to the subset *x* and makes no additional claims about any other subsets of P(X), each of which, by definition, has its own basic belief (Dempster,1968; Shafer 1976). It is worth noting that the following is possible in evidence theory as opposed to probability theory (Yager, 1967, 1967a):

1. $m(\{X_1\}) + m(\{X_2\}) \neq m(\{X_1, X_2\}$.

2. $m(\{X_1\}) \geq m(\{X_2\})$ $even\ though$ $X_1 \subseteq X_2$.

3. $m(X) < 1$

From the BBA, the lower and upper bounds of an imprecise probability interval known in evidence theory as belief and plausibility, respectively, can be expressed as

$$Bel(A) \leq P(A) \leq Pl(A) \tag{2.1}$$

The belief function of set *A*, $Bel(A)$ is defined as the sum of all BBA of its subsets given as

$$Bel(A) = \sum_{C \subseteq A} m(C) \tag{2.2}$$

Conceptually, $Bel(A)$ represents the level of total confidence that supports trustworthiness of event *A*. The plausibility function of set *A*, $Pl(A)$, is defined as the sum of all the BBA of the sets *C* that intersect it

$$Pl(A) = \sum_{C \cap A \neq \emptyset} m(C) \tag{2.3}$$

Conceptually, $Pl(A)$ represents the extent to which it is possible to consider the trustworthiness of event *A* due to lack of knowledge or data (epistemic uncertainty). In fact, the gap between belief and plausibility of event *A (Pl(A)-Bel(A))* is a measure of epistemic uncertainty in reliable evaluation of event *A* as shown in Figure 2.1. This gap is also interpreted as the imprecision on the "true probability" of event *A* (Baynon et al.,

2000). In probability theory, the probability of an event and its complement add up to 1. However, as it can be seen in Figure 2.1, the sum of the belief of an event and its complement is less than 1 in evidence theory. The sum of belief of an event and its complement equals to 1 only when there is sufficient knowledge (no ignorance) about the event. Unlike probability theory, evidence theory suggests that the belief of an event and its complement plus the level of ignorance (epistemic uncertainty) should add up to one.

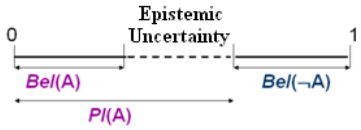

Figure 2.1 Relation between belief, plausibility and epistemic uncertainty

2.2 Aggregation rules of evidence

When the information or data comes from multiple sources of evidence, it is possible to encounter diverse belief structures with different assessments for the same frame of discernment. However, uncertainty can be represented only by a single belief structure. To reconcile this challenge, several approaches have been proposed for aggregation of evidence from all sources of information. The key to selecting a proper aggregation rule is to recognize how conflict and ignorance should be treated in a particular application. A number of aggregation rules have been reported in the literature (Dempster, 1968; Yager, 1987,1987a, 1994; Sents et al., 2000; Inagaki, 1991) with the two most popular ones briefly described below.

(a) Dempster's rule (1968) makes use of BBA in each subset of the universal set for each source of evidence and combines them to form a unique belief structure. Although these BBAs are defined on the same frame of discernment, all sources of

evidence are assumed to be independent. Dempster's rule combines two BBAs (i.e., $m_1$and m_2) derived from two sources of evidence as

$$m_{12}(A) = \frac{\sum_{B\cap C=A} m_1(B)m_2(C)}{1-K} \qquad when\ A \neq \emptyset \tag{2.4}$$

$$m_{12}(\emptyset) = 0 \tag{2.5}$$

with

$$K = \sum_{B\cap C=\emptyset} m_1\,(B)m_2(C) \tag{2.6}$$

where *K* represents the BBA of the conflict among the different sources of evidence, and its value is determined by adding the BBA products of all two disjointed subsets associated with the different sources of evidence. By placing the 1 - *K* (normalization factor) in the denominator of Eq. (2.4), Dempster's rule ignores completely the conflict between information obtained from the different sources and attributes the BBA associated with conflict to the null set. Therefore, when high level of conflict exists, Dempster's rule is not appropriate for combining evidence. Two pitfalls that are often cited for Dempster's rule of combination are as follows:

1. Dempster's rule assigns 100% uncertainty to a minority opinion when conflicting evidence exists. (Yager, 1987)

2. The combination of information from an evidence source that assigns a BBA to the base set (means complete ignorance is considered by this source of evidence) with that which does not consider ignorance results in BBA structure that does not assign BBA to the universal set. This action gives a false impression that precise probabilistic information dominates the belief.

(b) Yager's rule (1987,1987a) was developed to address some of the shortcomings of Dempster's rule. Yager introduced ground probability assignment (GPA), which for two BBAs ($m_1$and m_2) takes the form

$$q(A) = \sum_{B \cap C = A} m_1(B) m_2(C) \tag{2.7}$$

where *A* is the intersection of subsets *B* and *C*, and *q(A)* denotes the GPA of subset *A*. There is no normalization factor in Eq. (2.7). The combined structure *q(A)* can be also used to aggregate multiple pieces of evidence. If $m_1, m_{2,\ldots} m_n$ are the BBAs for *n* belief structures with $\mathrm{A_i}$ representing the focal element associated with the i^{th} BBA (m_i), then the *n* belief structures are combined as

$$q(A) = \sum_{\cap_{i=1}^{n} A_i = A} m_1(A_1) m_2(A_2) \ldots m_n(A_n) \tag{2.8}$$

Unlike Dempster's rule, GPA of greater than zero can be assigned to the null set in Yager's rule *(*$q(\emptyset) \geq 0$*)*. The procedure to calculate $q(\emptyset)$ is similar to that of *K* (conflict) in Eq. (2.6). The relationships between GPA and BBA of subset *A*, null set $\emptyset$ and the universal set *X* in Yager's rule of combination are given as

$$m^Y(A) = q(A) \tag{2.9}$$

$$m^Y(\emptyset) = 0 \tag{2.10}$$

$$m^Y(X) = q(X) + q(\emptyset) \tag{2.11}$$

The two major differences between Dempster's and Yager's rules of aggregation can be summarized as follows:

1. Yager's rule does not change the evidence through normalization as opposed to Dempster's rule.

2. Yager's rule allocates conflict to the universal set *X* as opposed to Dempster's rule that attributes conflict to the null set *(*$\emptyset$*)* . It is worth noting that in Yager's rule, the BBA associated with conflict is interpreted as the degree of ignorance.

The relationship between GPA defined by Yager's rule and BBA defined by Dempster's rule for the universal set *X* and subset *A* can be expressed as

$$m(X) = \frac{q(X)}{1 - q(\emptyset)} \tag{2.12}$$

$$m(A) = \frac{q(A)}{1-q(\emptyset)} \tag{2.13}$$

Given the Yager's rule's ability to more accurately deal with conflicting evidence, we have henceforth adopted this rule of aggregation unless otherwise noted.

2.3 Evidential framework for uncertainty representation

Here, the principles of evidence theory are used to develop a methodology for representing uncertainty using available data on uncertain variables. For practical application of this theory, however, it is necessary to address a number of unresolved issues. For example, in evidence theory, initial uncertainty is represented in terms of belief and plausibility. Experts' opinions or their combination with experimental data are necessary for the establishment of BBA, but an informative methodology to construct BBA using such information has not been established yet (Baynon, 2000). In many studies reported in the literature (Bae et al., 2004, 2006; Helton et al., 2004; Agarwal *et al*., 2004), researchers have focused primarily on uncertainty representation and propagation based on assumed belief structures (BBA).

This section describes the development of a general approach for developing BBA for each interval of uncertainty (subsets of a universal set) using available knowledge, data and opinions of experts based on the concepts of evidence theory. For this purpose, we first categorize different types of relationship between intervals of uncertainty and possible types of belief structures. Then, we will discuss how to represent possible values of uncertain variables in intervals using different sets of data, and apply the methodology presented in this section to construct a BBA for each interval of uncertainty.

2.3.1 Relationship types between two adjacent intervals of uncertainty

Two adjacent intervals of uncertainty can be categorized into one of the three different relationship states as described below:

a) Ignorance: When the number of data points (evidence) within one interval is far greater than that in its adjacent interval, the relationship between these two intervals is in the form of ignorance. As shown in Figure 2.2(a), the available data is mostly in favor of interval 1 and not 2. The smaller dataset in interval 2 can be viewed as providing some evidence of imprecision in considering only the dataset in interval 1. In other words, the smaller dataset in interval 2 may be interpreted as the imprecision on the true probability of interval 1 due to lack of knowledge or data.

Suppose the number of data points in intervals 1 and 2 are represented by *A* and *B* *(B<A)*, respectively. While *A* data points represent evidence in support of interval 1, *B* data points support the ignorance interval that spans over both intervals 1 and 2. Here, the criterion to have an ignorance relationship between intervals 1 and 2 is selected to be $\frac{B}{A} \leq 0.5$, although it is possible to reduce the upper bound to a different value. The BBA then takes the form

$$m(\{I_1\}) = \frac{A}{A+B} \tag{2.14}$$

$$m(\{I_1, I_2\}) = \frac{B}{A+B} \tag{2.15}$$

where I_1 and I_2 denote intervals 1 and 2, respectively. Based on the above BBA, belief and plausibility functions for I_1, I_2, and ignorance interval (i.e., I_1 and I_2) are given as

$$Bel(\{I_1\}) = \frac{A}{A+B} \qquad Pl(\{I_1\}) = 1 \tag{2.16}$$

$$Bel(\{I_2\}) = 0 \qquad Pl(\{I_2\}) = \frac{B}{A+B} \tag{2.17}$$

$$Bel(\{I_1, I_2\}) = 1 \qquad Pl(\{I_1, I_2\}) = 1 \tag{2.18}$$

Equations (2.14) and (2.15) are mathematical interpretation of ignorance between two adjacent intervals of uncertainty. Equation (2.16) assigns the probability of $\frac{A}{A+B}$ to I_1 due to the presence of A data points within this interval. There is a gap of $\frac{B}{A+B}$ between belief and plausibility of I_1 that comes from ignoring the dataset B in I_2. In fact, this gap $\frac{B}{A+B}$ is interpreted as the epistemic uncertainty or imprecise probability of I_1 being $\frac{A}{A+B}$. Equation (2.17) considers no probability for I_2 since the B data points within this interval are insufficient and can support only the ignorance interval. However, the gap $\frac{B}{A+B}$ between belief and plausibility of I_2 (interpreted as the amount of imprecision that the true probability of I_2 is zero) indicates that the true probability can extend to $\frac{B}{A+B}$ due to lack of knowledge or data. Equation (2.18) assigns probability of 1 to the ignorance interval with no gap between belief and plausibility since there is complete knowledge that this interval covers all data points.

b) Agreement: When there are nearly equal data points in two adjacent intervals, the two intervals can be combined into a single wider interval of uncertainty. This type of relationship is shown in Figure 2.2(b). Note that the combined interval of uncertainty due to the agreement relationship is completely different from the ignorance interval. Suppose the number of data within I_1 and I_2 are A and B $(B<A)$, respectively. Then, an agreement relationship exists if $\frac{B}{A} \geq 0.8$. There is no BBA for agreement relationship because only one combined interval is considered.

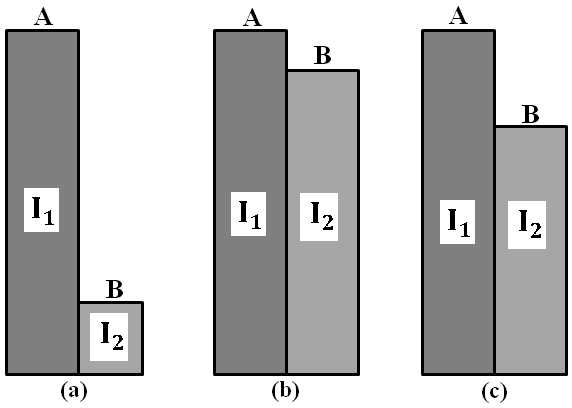

Figure 2.2 Relationship types between intervals of uncertainty: (a) ignorance, (b) agreement and (c) conflict

c) Conflict: When the ratio of data points in two adjacent intervals falls between the limits specified for the previous two relationships *(i.e.,* $0.5 < \frac{B}{A} < 0.8$*)*, the two intervals are said to be in conflict (Figure 2.2 (c)). In this case, the number of data points within intervals 1 and 2 is enough to support each one separately and no ignorance exists. Hence, the BBA for conflicting relationship can be expressed as

$$m(\{I_1\}) = \frac{A}{A+B} \tag{2.19}$$

$$m(\{I_2\}) = \frac{B}{A+B} \tag{2.20}$$

Based on the above BBA, belief and plausibility functions for I_1, I_2, and ignorance interval (I_1 and I_2) are given as

$$Bel(\{I_1\}) = \frac{A}{A+B} \qquad Pl(\{I_1\}) = \frac{A}{A+B} \tag{2.21}$$

$$Bel(\{I_2\}) = \frac{B}{A+B} \qquad Pl(\{I_2\}) = \frac{B}{A+B} \tag{2.22}$$

$$Bel(\{I_1, I_2\}) = 1 \qquad Pl(\{I_1, I_2\}) = 1 \tag{2.23}$$

Equations (2.19) and (2.20) are mathematical interpretation of conflict between two adjacent intervals of uncertainty. Equation (2.21) assigns the probability of $\frac{A}{A+B}$ to I_1 due to the evidence of A data points within it. Similarly, Eq. (2.22) assigns the probability of $\frac{B}{A+B}$ to I_2 due to the supporting evidence of B data points within that interval. There is

no gap between belief and plausibility in each interval. Since there is no imprecision due to lack of knowledge or data, true probability of I_1 is $(\frac{A}{A+B})$ and that for I_2 is $(\frac{B}{A+B})$.

2.3.2 Possible types of belief structure for all intervals of uncertainty

When considering all intervals of uncertainty for a particular parameter, one of three types of belief structure (Baysian, consonant, and general), as shown in Figure 2.3, can be encountered. In the Bayesian belief structure, all intervals of uncertainty are disjointed and treated as having conflict. Similar to the case of ignorance, all intervals of uncertainty in consonant belief structure are in ignorance. Intervals of uncertainty can be in both forms of ignorance and conflict in the case of general belief structure, which is more prevalent in uncertainty quantification of a physical system.

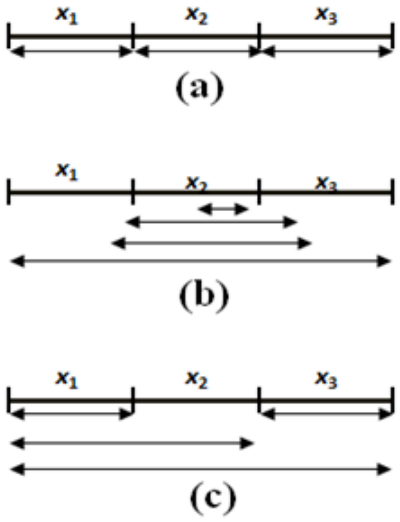

Figure 2.3 Different types of belief structure: (a) Bayesian, (b) consonant (c) general

2.3.3 A methodology to construct BBA for intervals of uncertainty

The ignorance, agreement, and conflict relationships between adjacent intervals of uncertainty may result in different types of belief structure depending on distribution of

data in the ignorance interval of uncertainty (universal set). The steps for BBA construction of uncertain data can be generalized as follows:

1. Collect all possible values of uncertain data (e.g., Yield stress value from testing different material samples) and determine the interval of uncertainty that represents the universal set.

2. Plot a histogram (bar chart) of the collected data. Note that the number of bars represents the number of disjointed intervals whose relationships should be established for BBA construction. Naturally, increasing the number of intervals (reducing the bounds on each interval) results in a more accurate belief structure while increasing its complexity and prolonging its computational time.

3. Identify adjacent intervals of uncertainty that are in agreement and combine them.

4. Identify the interval with the highest number of data points (I_m) and establish its relationship with each of the adjacent intervals to its immediate left and right (I_a). If the ignorance relationship should be used between I_m and I_a, the BBA follows Eqs. (2.14) and (2.15) and takes the form

$$m\{(I_m)\} = \frac{D_m}{D} \tag{2.24}$$

$$m\{(I_m, I_a)\} = \frac{D_a}{D} \tag{2.25}$$

where D represents the total number of data points, with D_m and D_a representing the number of data points in I_m and I_a, respectively. If the conflict relationship should be used, the BBA follows Eqs. (2.19) and (2.20) and takes the form

$$m\{(I_m)\} = \frac{D_m}{D} \tag{2.26}$$

$$m\{(I_a)\} = \frac{D_a}{D} \tag{2.27}$$

5. Consider the adjacent interval (I_c) to interval I_a with D_c number of data points. The aim is to consider data points of I_c for construction of BBA. Here, two different cases are possible:

a) I_a and I_m are in ignorance relationship: Since D_a supports only the ignorance interval that spans over both I_a and I_m and does not support I_a alone, I_a should not be compared with I_c whose data points (D_c) are to be considered in construction of BBA. Instead, in this case, relationship type of I_c should be determined with I_m.

If I_c and I_m are in ignorance relationship, the following BBA should be added to the former constructed in step 4

$$m\{(I_m, I_a, I_c)\} = \frac{D_c}{D} \tag{2.28}$$

Also in this case, in order to reduce members of the belief structure and to save computational time for uncertainty propagation stage, it is possible to combine ignorance data of I_a and I_c and consider the following BBA instead of those determined by Eqs. (2.25) and (2.28).

$$m\{(I_m, I_a, I_c)\} = \frac{D_a + D_c}{D} \tag{2.29}$$

If I_c and I_m are in conflict relationship, the following BBA should be added to the former constructed in step 4

$$m\{(I_c)\} = \frac{D_c}{D} \tag{2.30}$$

b) I_a and I_m are in conflict relationship: Since D_a is enough to support I_a, its relationship type should be determined with I_c whose data points (D_c) are to be considered in construction of BBA.

If I_c and I_a are in ignorance relationship, the following BBA should be added to the former constructed in step 4

$$m\{(I_c, I_a)\} = \frac{D_c}{D} \tag{2.31}$$

If I_c and I_a are in conflict relationship, the following BBA should be added to the former constructed in step 4

$$m\{(I_c)\} = \frac{D_c}{D} \tag{2.32}$$

This procedure can be repeated to consider data points in subsequent intervals for constructing the belief structure. It is important to note that in case of encountering an interval with conflicting data, that interval should be compared with next intervals in order to determine their relationship type instead of I_m. Following this methodology, it can be seen that based on distribution of data, all belief structures (Bayesian, consonant, and general) are possible. The methodology offers consonant belief structure if all intervals are in ignorance with I_m. On the other hand, it offers Bayesian belief structure as long as all disjointed intervals of histogram include sufficient data. In case of existing intervals with both sufficient and insufficient data, general belief structure will be suggested by the presented methodology. In the next section, we will provide an example for further clarification of the presented methodology.

2.4 Evidential framework for uncertainty propagation and measurement

Uncertainty propagation of a response with dependence on multiple uncertain variables requires the construction of a joint belief structure, which serves a similar role as the joint probability density function in probability theory. (Agarwal et al., 2004; Bae et al., 2004) A joint belief structure is obtained by the Cartesian product of the belief structures of all uncertain variables for a structural system. (Agarwal et al., 2004; Bae et al., 2004) This involves multiplication of the final BBA found for each subinterval of one uncertain variable with those of the other variables involved in the Cartesian product. A

portion of a simple joint belief structure for a hypothetical 3-variable space is shown in Figure 2.4 with double arrows showing the intervals for each variable. Three joint proposition "cells" are shown in Figure 2.4 with $BBA_1 = m(x_1)m(y_3)m(z_2)$, $BBA_2 = m(x_2)m(y_1)m(z_3)$, and $BBA_3 = m(x_3)m(y_2)m(z_1)$. It is worth noting that the joint proposition cells may not always be spaced as shown in Figure 2.4, with the possibility of one cell intersecting or possibly overlapping completely one or more other joint proposition cells.

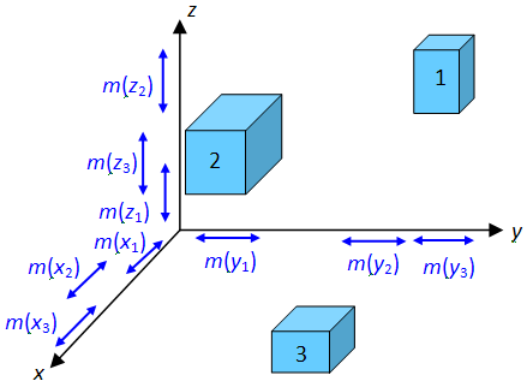

Figure 2.4 Example of a joint belief structure in 3-variable space

The discrete form of the joint belief structure prevents its modeling by a mathematical function, and for uncertainty propagation, it is necessary to evaluate the system response for every combination of uncertain parameter values within each cell. For response evaluations involving monotonic functions, analyses are performed only at the vertices of each joint proposition cell according to the vertex method of Dong and Shah (1987). Otherwise, it is necessary to search the entire continuous space within each cell to find the response interval. When problems comprise simple analytical functions, the evaluation of the response may not be very expensive, but computational complexity and cost can drastically increase when: 1) there are many uncertain parameters with each

defined in multiple piece-wise continuous bands or intervals; 2) response evaluation requires expensive high fidelity simulation; and 3) the response functions of interest are non-monotonic requiring the solution of numerous nonlinear optimization problems in search of the minimum and maximum response values in each joint proposition cell.

To alleviate the computational complexity, a methodology that relies on metamodes for propagation of represented uncertainties is introduced. First, using the design and analysis of computer experiments, separate surrogate models based on different formulation of a physical system are developed to relate their uncertain variables to their response. Then, several global optimizations using Genetic Algorithm (GA) is performed to find the upper and lower bounds of the response for each member of the constructed joint belief structure of uncertain variables. Note that due to the disjoint form of the constructed belief structure, an optimization problem with different sets of side constraints of uncertain variables must be setup in each cell.

Different formulations of a physical system result in different propagated belief structures for simulation responses. As a result, the choice of appropriate formulation of a physical system is subject to model selection uncertainty. For modeling model selection uncertainty and reducing the associated epistemic uncertainty, Yager's combination rule (1987, 1987a) is used to combine the propagated belief structures of different formulations of a physical system for simulation response into a single belief structure.

Finally, for the sake of uncertainty quantification, belief and plausibility of the simulation response are found using two different approaches. In the first approach, precision intervals for observed value of simulation response are constructed and the associated belief and plausibility are estimated using the determined propagated belief structure. In the second approach, a belief structure for simulation response is constructed

by first collecting all available evidence from experimental, analytical and numerical sources following the approach in section 2.3. Then, the belief and plausibility of the constructed belief structure for simulation response are estimated using the determined propagated belief structure.

2.5 Modeling field uncertainty

Field uncertainty describes spatial variation of the uncertain variables. This type of uncertainty can be encountered in a structural component or system where material or other properties vary from one location to another to the extent that the use of a single random variable for each parameter will produce inaccurate results. Representation and propagation of field uncertainty in materials using evidence theory is one main aspect of this dissertation.

Random field theory has been employed in a number of investigations (Xiaolei et al, 2009; Choi et al, 2007) to account for material field uncertainty. Instead, this dissertation introduces a field belief structure and joint field belief structure to accommodate field uncertainty using the framework of evidence theory.

Each cell of a joint field belief structure includes a number of sub-cells that are one possible member of the constructed joint belief structure for all uncertain variables. The number of sub-cells in each cell of the joint field belief structure is equal to the number of regions of the product that are more prone to be affected by spatial variation of uncertain variables. Each sub-cell that is a member of the constructed joint belief structure for uncertain variables is responsible for representation of uncertainty for each region of the product recognized potentially to have different representation of material uncertainties as opposed to the other regions. In fact, to consider field uncertainty, all

combinations of intervals in the belief structure of one uncertain variable in one region with those of all other variables in every other region must be considered. More details associated with field uncertainty will be presented later in chapter 8.

CHAPTER III

PLASTICITY MODELS

In this chapter, the JC and BCJ plasticity models are presented. Also, a physics-guided numerical fitting approach is presented for determination of material constants of BCJ plasticity model. These models describe the physical response of a metallic material under the influence of external loads.

3.1 Johnson-Cook plasticity model

The basic Johnson-Cook (JC) plasticity model gives a semi-empirical relationship for the von Mises flow stress that is formulated as: (Johnson and Cook, 1983; Holmquist and Johnson, 1991)

$$\sigma = [A + B\varepsilon^n][1 + Cln\dot{\varepsilon}^*][1 - T^{*m}] \tag{3.1}$$

where ε is the equivalent plastic strain and $\dot{\varepsilon}^* = \dot{\varepsilon}/\dot{\varepsilon}_o$ is the dimensionless plastic strain rate with $\dot{\varepsilon}_o = 1.0\ s^{-1}$. The constant *A* represents the yield stress of the material tested at room temperature and $\dot{\varepsilon}^* = 1 s^{-1}$, *B* and *n* represent strain hardening effects, whereas C and *m* control the strain rate and temperature effects, respectively. T^* is non-dimensional temperature given as: (Tanner et al., 1999)

$$T^* = \frac{T - T_{room}}{T_{melt} - T_{room}} \tag{3.2}$$

with an alternative form (Gottstein et al., 1983)

$$T^* = \frac{T}{T_{melt}} \tag{3.3}$$

All temperature quantities in Eqs. (3.2) and (3.3) are measured in units of Kelvin. In Johnson et al., 1985, authors adopted the formulation in Eq. (3.3) for the non-

dimensional temperature. However, in their previous studies (Johnson and Cook, 1983; Holmquist and Johnson, 1991) as well as others reported in the literature (Tanner et al., 1999), Eq. (3.2) was considered for the non-dimensional temperature. The choice of appropriate form of non-dimensional temperature, representing expert opinion, is subject to epistemic uncertainty, and it is not obvious which formulation would describe more accurately the physics of complicated inelastic material behavior. Here, we consider both formulations for non-dimensional temperature to address epistemic uncertainty associated with model selection.

It is worth noting that different formulations for capturing the strain rate effects have also been proposed. They include log-quadratic Huh-Kang, exponential Allen-Rule-Jones, and exponential Cowper-Symonds. (Hallquist, 1993) For more accurate representation of model selection uncertainty, all alternative formulations of JC should be considered. In an effort to limit the scope of this dissertation, alternative models of JC plasticity are confined only to the two forms of non-dimensional temperature and Eq. (3.1). Note that the focus is mainly on representation of uncertainty for different types of JC material models in intervals with assigned BBA.

3.2 Constitutive equations of BCJ plasticity model

The BCJ plasticity model (Bammann, 1984; Bammann et al. 1993, 1996) is a dislocation-based internal state variable (ISV) model that describes the rate- and temperature-dependent finite deformation behavior of ductile metals. The complete version of the model is envisioned to have a number of ISVs that should represent such material features as dislocation hardening, void-induced damage, plastic anisotropy, recrystallization and grain growth, as well as deformation-induced phase transformations.

The particular version of the model used in this work mainly accounts for the plasticity aspects of the material response, i.e., the kinetics of plastic flow and dislocation hardening. In essence, this particular version of the model a) introduces a dynamic yield surface whose evolution is governed by temperature, strain rate and stress state; and b) contains two plastic state variables representing isotropic and kinematic hardening which model, respectively, the size and location of the dynamic yield surface. The evolution equations of these variables assume that the material hardening processes such as storage of dislocations (isotropic hardening) and formation of cells and cell boundaries (kinematic hardening) are balanced by recovery processes such as dislocation cross slip and dislocation climb.

The basic formulation of the plasticity and temperature aspects of the model relies on an extended description of the large deformation kinematics using the multiplicative decomposition of the deformation gradient into thermal, plastic and elastic components (Marin et al., 2006). This kinematics coupled with a thermodynamic approach with ISVs, as proposed by Coleman and Gurtin (Coleman et al., 1967), gives the formulation of BCJ a strong mathematical basis that relies upon very well known principles of continuum mechanics. The 3-D model equations defined by Eqs. (3.4) through (3.8) below describes the elastic law, kinematics, and the plasticity (flow rule and hardening laws), and are valid for small elastic strains (typical in metals).

$$\underline{\sigma}^{\circ} = \underline{\dot{\sigma}} - \underline{W}^{e}\underline{\sigma} + \underline{\sigma}\,\underline{W}^{e} = \lambda tr\left(\underline{D}^{e}\right)\underline{I} + 2\mu\underline{D}^{e} \tag{3.4}$$

$$\underline{D}^{e} = \underline{D} - \underline{D}^{in} - \underline{D}^{th},\ \ \underline{W}^{e} = \underline{W} - \underline{W}^{P} \tag{3.5}$$

$$\underline{D}^{in} = \sqrt{\frac{2}{3}}\dot{\bar{\varepsilon}}^{p}\underline{N}, \qquad \dot{\bar{\varepsilon}}^{p} = f(T)\sinh\left[\frac{\left|\underline{\sigma}-\underline{\alpha}\right| - (R+Y(T))}{V(T)}\right] \tag{3.6}$$

$$\underline{\alpha}^{o} = \underline{\alpha} - \underline{W}^{e}\underline{\alpha} + \underline{\alpha}\underline{W}^{e} = h(T)\underline{D}^{in} - \left[r_{d}(T)\dot{\bar{\varepsilon}}^{p} + r_{s}(T)\right]\sqrt{\frac{2}{3}}\left\|\underline{\alpha}\right\|\underline{\alpha} \tag{3.7}$$

$$\dot{R} = H(T)\dot{\bar{\varepsilon}}^{p} - \left[R_{d}(T)\dot{\bar{\varepsilon}}^{p} + R_{s}(T)\right]R^{2} \tag{3.8}$$

Where $\bar{\sigma} = \sqrt{\frac{3}{2}}\left\|\underline{\xi}\right\|$, $\underline{N} = \frac{\underline{\xi}}{\left\|\underline{\xi}\right\|}$, $\underline{\xi} = \underline{\sigma'} - \frac{2}{3}\underline{\alpha}$, $\underline{\sigma'} = \underline{\sigma} - \sigma_m \underline{I}$ with $\sigma_m = 1/3\sigma_{kk}$. In Eq. (3.4), $\overset{\circ}{\underline{\sigma}}$ is an objective stress rate, λ and μ are the Lame´s constants, $\underline{\sigma}$ is the Cauchy stress, $\underline{W^e}$ is the elastic spin, $\underline{I}$ is the identity tensor, and $tr(\bullet)$ is the trace operator. Decomposing the skew symmetric and symmetric parts of the velocity gradient into elastic and plastic parts, one derives Eq. (3.5) that is written for the elastic stretching $\underline{D^e}$ and the elastic spin $\underline{W^e}$. In this equation, $\underline{D^{in}}$ is the deviatoric inelastic strain rate, $\underline{D^{th}}$ is the stretching rate due to the thermal expansion, and $\underline{W^P}$ is the plastic spin assumed to be zero here. Here, $\underline{D}$ and $\underline{W}$ denote the total deformation and spin which are defined by the boundary conditions. As shown by Eq. (3.6), the deviatoric inelastic flow rule $\underline{D^{in}}$ that encompasses the regimes of creep and plasticity is a function of the kinematic and isotropic ISVs $\underline{\alpha}$ and R, respectively, and the functions *f(T), V(T)* and *Y(T)* which have an Arrhenius-type temperature dependence. The evolution equations of $\underline{\alpha}$ and R are presented in a hardening-minus-recovery format by Eqs. (3.7) and (3.8) in which *h(T)* and *H(T)* are the hardening moduli, $r_d(T)$ and $R_d(T)$ are the functions describing dynamic recovery, $r_s(T)$ and $R_s(T)$ are the functions representing static recovery, and $\|(\bullet)\|$ is the norm operator. The temperature dependence of these material functions are summarized in Table 1, where the C_i, i = 1,18 are material constants or parameters. Note that these parameters include sources of uncertainty reflecting indirectly the variability and incertitude in the material microstructure. The BCJ plasticity model is implemented in LSDYNA as MAT_051 with the material constants in Table 3.1 defined as input parameters.

Table 3.1 Relationship between parameter functions and material constants of the BCJ plasticity model

$V(T) = C_1 exp\,(-C_2/T)$	$r_s(T) = C_{11} exp\,(-C_{12}/T)$
$Y(T) = C_3 exp\,(C_4/T)$	$R_d(T) = C_{13} exp\,(-C_{14}/T)$
$f(T) = C_5 exp\,(-C_6/T)$	$H(T) = C_{15} exp\,(C_{16}/T)$
$r_d(T) = C_7 exp\,(-C_8/T)$	$R_s(T) = C_{17} exp\,(-C_{18}/T)$
$h(T) = C_9 exp\,(C_{10}/T)$	

3.2.1 BCJ Equations for the Case of Uniaxial Stress

The unknown material constants of the BCJ model shown in Table 3.1 are determined by comparing model predictions to experimental data from specimens under uniform stress states (e.g. uniaxial stress-strain curves) at constant temperatures and strain rates. For the case of uniaxial stress (tension or compression) under isothermal conditions, the BCJ model equations reduce to

$$\dot{\sigma} = E(\dot{\varepsilon} - \dot{\varepsilon}^p) \tag{3.9}$$

$$\dot{\varepsilon}^p = f(T)\sinh\left[\frac{|\sigma-\alpha| - R - Y(T)}{V(T)}\right]\text{sign}(\sigma-\alpha) \tag{3.10}$$

$$\dot{\alpha} = h(T)\,\dot{\varepsilon}^p - \left[r_d(T)\left|\dot{\varepsilon}^p\right| + r_s(T)\right]\alpha^2\text{sign}(\alpha) \tag{3.11}$$

$$\dot{R} = H(T)\left|\dot{\varepsilon}^p\right| - \left[R_d(T)\left|\dot{\varepsilon}^p\right| + R_s(T)\right]R^2 \tag{3.12}$$

where σ is the only non-vanishing component of the Cauchy stress tensor; α, $\dot{\varepsilon}$, and $\dot{\varepsilon}_P$ are the normal components along the principal axis of tensors $\underline{\alpha}$, $\underline{D}$, and $\underline{D}^{in}$, respectively.

Here, we assume that shortly after the yield point, the plastic strain rate $\dot{\varepsilon}_P$ can be reasonably approximated by the total strain rate $\dot{\varepsilon}$, i.e., $\dot{\varepsilon} \approx \dot{\varepsilon}_P$ (viscoplasticity). Also, for each experimental stress-strain curve, the temperature T and strain rate $\dot{\varepsilon}$ are constant; hence, the variables are mainly functions of strain ε. Considering this fact and employing the chain rule of differentiation, one can show that for each experimental strain-stress curve, the time derivatives of α and R can be expressed as $\dot{\alpha} = \frac{d\alpha}{dt} = \dot{\varepsilon}\frac{d\alpha}{d\varepsilon}$, $\dot{R} = \frac{dR}{dt} = \dot{\varepsilon}\frac{dR}{d\varepsilon}$.

Considering these assumptions, Eqs. (3.10) to (3.12) can then be written as

$$\dot{\varepsilon}^p = f(T)\sinh\left[\frac{|\sigma-\alpha|-R-Y(T)}{V(T)}\right]\text{sign}(\sigma-\alpha) \tag{3.13}$$

$$\dot{\varepsilon}\frac{d\alpha}{d\varepsilon} = h\dot{\varepsilon} - \left[r_d|\dot{\varepsilon}| + r_s\right]\alpha^2\text{sgn}(\alpha) \tag{3.14}$$

$$\dot{\varepsilon}\frac{dR}{d\varepsilon} = H|\dot{\varepsilon}| - \left[R_d|\dot{\varepsilon}| + R_s\right]R^2 \tag{3.15}$$

The integration of Eqs. (3.14) and (3.15), with the initial values of α and R set to zero, yields

$$\alpha = \sqrt{\frac{h\dot{\varepsilon}}{(r_d\dot{\varepsilon}+r_s)}}\,tanh\left(\frac{\varepsilon\sqrt{h\dot{\varepsilon}(r_d\dot{\varepsilon}+r_s)}}{\dot{\varepsilon}}\right) \tag{3.16}$$

$$R = \sqrt{\frac{H\dot{\varepsilon}}{(R_d\dot{\varepsilon}+R_s)}}\,tanh\left(\frac{\varepsilon\sqrt{H\dot{\varepsilon}(R_d\dot{\varepsilon}+R_s)}}{\dot{\varepsilon}}\right) \tag{3.17}$$

Note that when closed form solutions of the differential constitutive equations are not possible, one will have to rely on the numerical integration of the equations to perform the calibration of the material constants. As the initial guess used to start such calibration procedure will affect the quality of the fitting, the approach presented in Section 3.2.2 may be used to minimize this effect.

By inverting the flow rule in Eq. (3.13) and substituting Eqs. (3.16) and (3.17), one obtains

$$\sigma = \sqrt{\frac{h\dot{\varepsilon}}{(r_d\dot{\varepsilon}+r_s)}}\tanh\left(\frac{\varepsilon\sqrt{h\dot{\varepsilon}(r_d\dot{\varepsilon}+r_s)}}{\dot{\varepsilon}}\right) + \sqrt{\frac{H\dot{\varepsilon}}{(R_d\dot{\varepsilon}+R_s)}}\tanh\left(\frac{\varepsilon\sqrt{H\dot{\varepsilon}(R_d\dot{\varepsilon}+R_s)}}{\dot{\varepsilon}}\right) + V\sinh^{-1}\left(\frac{\dot{\varepsilon}}{f}\right) + Y \tag{3.18}$$

Equation (3.18) describes the stress as a function of the ISVs, strain rate and temperature.

3.2.2 The New Physics-Guided Fitting Approach

The ability of the BCJ plasticity model to predict the mechanical behavior of metals under different temperatures and strain rates is strongly dependent upon the correct determination of its eighteen material constants. Recently, Guo et al. (2005) determined the BCJ material constants for Ti-6Al-4V titanium, AISI 52100 steel, and

6061-T6 aluminum alloy through nonlinear least-squares fitting of the BCJ model to experimental stress-strain data of the respective materials. One observation they made was that the arbitrary choice of starting values for the constants in the nonlinear fitting procedure does not guarantee the best fit. Considering that no physical bounds have been established for the eighteen material constants of BCJ plasticity model, the task of finding the best fit can be very tedious and present a source of uncertainty. To address this challenging task, Guo et al. (2005) began by fitting approximately three constants at a time while holding the others fixed, and monitored the fitting improvement by checking the maximum and average residual (fitting errors) as a reference to tune the constants in each attempt until a satisfactory fit was obtained. However, that fitting approach is tedious, nonphysical, and relies heavily on the numerical aspects of fitting. In fact, all constants can be fitted simultaneously with stress-strain data at different temperatures and strain rates with no physical interpretation of the fitting procedure. That approach also requires a large number of stress-strain curves, which may not be practical when faced with scarcity of data for a particular material. In this section, we introduce a physics-guided numerical fitting approach to address the difficulties in determining the constants of BCJ plasticity model.

For stress-strain curves at a constant temperature, the parameter functions of the BCJ model in Table 3.1 will have a fixed value for temperature. The proposed fitting approach suggests fitting of the parameter functions with two separate sets of stress-strain curves at low and high temperatures. While reducing the unknown constants from eighteen to nine, this procedure requires the duplication of the fitting process for sets of stress-strain curves at two different temperatures. Suppose that for an arbitrary parameter function *Y(T)* of the same general form as those in Table 3.1, i.e., $Y(\mathrm{T}) = \mathrm{C}_1 \exp(\mathrm{C}_2/\mathrm{T})$,

two values (say Y_1 and Y_2) are known through fitting the model with two different sets of stress-strain curves of various strain rates at low temperature T_1 and high temperature T_2. Then, constants C_1 and C_2 can be easily determined using the following equations:

$$C_2 = \frac{T_1 T_2}{T_2 - T_1} ln\left(\frac{Y_1}{Y_2}\right) \tag{3.19}$$

$$C_1 = Y_1 exp\left(\frac{-T_2}{(T_2 - T_1)} ln\left(\frac{Y_1}{Y_2}\right)\right) \tag{3.20}$$

Hence, using the above formulations, material constants that represent the material behavior at different temperatures and strain rates can be determined. This decreases uncertainty in the traditional fitting approach by considering the material behavior at different temperatures and reducing the number of constants that need to be fitted simultaneously.

In addition, the proposed fitting method suggests fitting the unknown constants of the evolution equations for the hardening variables (Eqs. (3.7) and (3.8)) and the equation for the flow stress (inverse of Eq. (3.6)) separately in different stages while keeping the physical link and flow of information among them. This reduces the fitting of nine parameters to three at a time in three stages, easing the process of fitting. Details of the physics-guided numerical fitting approach are provided below.

3.2.2.1 Evaluation of hardening parameters

Loading and unloading experiments on many ductile materials have shown that the flow stress in reverse direction softens sooner than that of forward direction, as shown in Figure 3.1, resulting in the reduction of reverse flow, a phenomenon known as Baushinger effect (Jordon et al., 2007). This behavior is mainly because the mechanical response of metals in plastic deformation is affected by deformation history in addition to the current stress state. The physics-guided fitting approach considers such effects in

computing the hardening constants through experimental evaluation of the ISVs α and R using forward-to-reverse yield data of materials at different temperatures and strain rates.

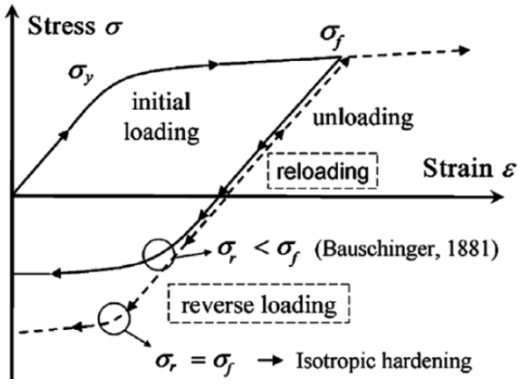

Figure 3.1 Quantification of $\sigma_f, \sigma_r, \sigma_y$ from experimental stress strain curve (Jordon et al., 2007)

The experimental values of ISVs α and R can be found through definition of the von-Misses yield surface for both forward and reverse loading as given by

$$\left|\sigma_f - \alpha\right| - R - \sigma_y = 0 \tag{3.21}$$

$$|\sigma_r - \alpha| - R - \sigma_y = 0 \tag{3.22}$$

where $\sigma_f, \sigma_r, \sigma_y$ are the forward yield, reverse yield, and initial yield stress, respectively (see Figure 3.1). As σ_f - $\alpha > 0$ and σ_r - $\alpha < 0$ ($\sigma_r < 0$), one can derive from the Eqs. (3.21) and (3.22) the expressions for α and R as

$$\alpha = \frac{\sigma_f + \sigma_r}{2} \tag{3.23}$$

$$R = \frac{\sigma_f - \sigma_r}{2} - \sigma_y \tag{3.24}$$

The constants of the hardening evolution equations are derived as follows:

Step 1: Collect forward-to-reverse yield data of material at different strains and strain rates at a low temperature T_1.

Step 2: Quantify experimental values of hardening parameters α and R using Eqs. (3.23) and (3.24) and the collected data in Step 1.

Step 3: Fit Eqs. (3.16) and (3.17) individually using the α and R values found in Step 2 and the nonlinear least-squares fitting approach to determine values of the hardening functions h, r_s, r_d, H, R_s and R_d for T_1. When closed form expressions of ISVs a and R are not easy to obtain, initial guesses for hardening functions should be made. Then, differential equations of a and R should be solved numerically to obtain their plots as a function of strain. Finally, these estimated plots should be compared with the corresponding experimental plots. In case a good match is not found, another set of values for hardening functions should be selected and the process should be repeated until a good match is obtained.

Step 4: Repeat Steps 1 to 3 for a high temperature T_2; and

Step 5: Use Eqs. (3.19) and (3.20) along with the derived parameters of the evolution equations at temperatures T_1 and T_2 to solve for the corresponding material constants (C7 to C18).

3.2.2.2 Evaluation of flow parameters

After computing the twelve hardening constants, the additional six constants for the flow rule are determined using four stress-strain curves under monotonic loading: two (low and high strain rates) at a low temperature and the other two (also low and high strain rates) at a high temperature. Note that the parameters of the hardening evolution equations in Eq. (3.18) are known from the fitting procedure above. Then, the unknown parameters to be fitted in Eq. (3.18) are *Y, V* and *f*. The step-by-step procedure to determine the constants of flow rule equation is as follows:

Step 1: Fit Eq. (3.18) with two stress-strain curves of high and low strain rates simultaneously using a genetic algorithm-based multi-functional nonlinear least-squares fitting at low temperature T_1 to determine unknown parameters of *Y, V* and *f*.

Step 2: Repeat Step 1 for high temperature T_2.

Step 3: Use Eqs. (3.19) and (3.20) along with derived parameters of flow rule equation at temperatures T_1 and T_2 to solve for the corresponding material constants (C_1 to C_6).

3.2.2.3 Determination of BCJ constants for AL 7075-T651

As an illustrative example of the presented fitting approach, the material constants of 7075-T651 aluminum alloy are determined using the experimental data provided in (Lee et al., 2000; Renolds et al., 2000; Jordon et al., 2007; Guo et al., 2009). Forward-to-reverse yield of this alloy at different strains, temperatures, and strain rates as shown by Table 3.2 are used to estimate the experimental values of α and R. Fitting the hardening evolution equations of the BCJ model using the data in Table 3.2 yields the corresponding material constants C_7 to C_{18} as shown in Table 3.3. The material constants C_1 to C_6 of the flow rule are computed using four stress-strain curves at different strain rates and temperatures (see Figure 3.2). Figure 3.2 compares the generated stress-strain curves by the BCJ model using the derived constants in Table 3.3 with experimental data that are used in the fitting process. As expected, the generated curves and those from the experiments match very well. As an additional check, the computed constants in Table 3.3 are used to predict the experimental stress-strain curves at other temperatures and strain rates. The predicted and experimental responses curves are shown in Figure 3.3. As observed, there is a fairly good agreement between experimental and predicted curves.

This verifies the accuracy of the BCJ material constants using the presented fitting approach.

Table 3.2 Evaluation of state variables α and R at different strains, temperatures and strain rates.

ε	σ_y(MPa)	σ_f(MPa)	σ_r(MPa)	α(MPa)	R(MPa)
T=297 K, $\dot{\varepsilon}$ = 0.1					
0.01	454	521	- 439	41	26
0.03	454	549	- 390	79.5	15.5
0.05	454	583	- 363	110	19
T=673 K, $\dot{\varepsilon}$ = 0.01					
0.04	60.3	65.3	- 60.3	2.5	2.5
0.31	60.3	63.3	- 61.4	0.95	2.05
0.55	60.3	61.8	- 59.2	1.3	0.2

Table 3.3 Calculated BCJ material constants for 7075-T651 aluminum alloy.

C_1 (MPa)	C_2 (K)	C_3 (MPa)	C_4 (K)	C_5 (1/s)	C_6 (K)	C_7 (1/MPa)	C_8 (K)	C_9 (MPa)
312.86	154.78	27.2	818.26	6914.10	233.39	9.00	1632.34	148.36
C_{10} (K)	C_{11} (s/MPa)	C_{12} (K)	C_{13} (1/MPa)	C_{14} (K)	C_{15} (MPa)	C_{16} (K)	C_{17} (s/MPa)	C_{18} (K)
942.28	100.67	2517.12	98.53	171.56	8950.63	279.18	7363.75	3316.82

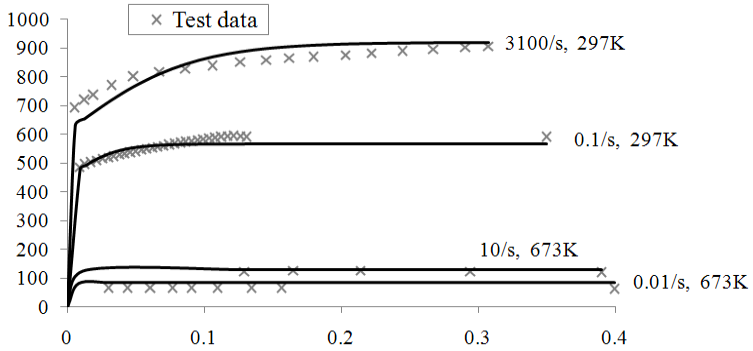

Figure 3.2 Comparison of the fitted curves and the corresponding experimental data

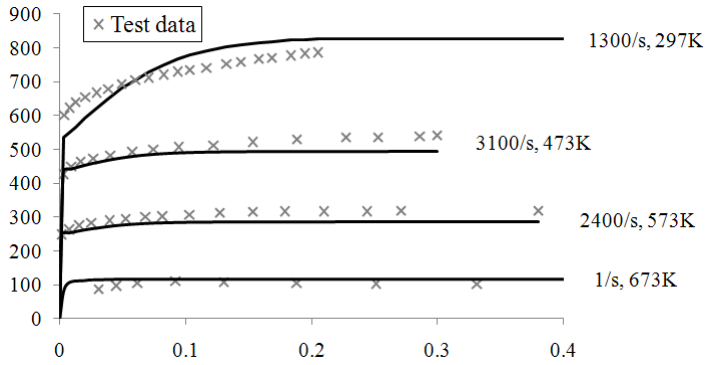

Figure 3.3 Comparison of the predicted curves and the corresponding experimental data

The proposed fitting approach will be used in Chapter 4 to derive all possible material constants of BCJ plasticity model for AL 7075-T651 material for the sake of uncertainty representation.

CHAPTER IV

UNCERTAINTY REPRESENTATION OF PLASTICITY MODELS

In this chapter, the evidence-based framework presented in chapter 2 is used to represent epistemic uncertainty in constitutive models by focusing on JC and BCJ plasticity models. To this end, different formulations of JC material model along with multiple sources of experimental data and alternate approaches for fitting the model constants have been considered. Also, the introduced physics-guided fitting approach in chapter 3 is used to derive all possible material constants of BCJ plasticity model for uncertainty representation.

4.1 Sources of uncertainty in plasticity models

Due to the complicated dynamic material behavior, plasticity models (including JC) involve epistemic uncertainty. Three major sources of uncertainty addressed specifically in this dissertation are as follows:

a) Uncertainty in test data: Various tests have been suggested for finding the material constants of plasticity models for a particular material. These tests include torsion, tension, compression, biaxial, or tri-axial loading conditions. Besides the type of test, the testing equipment and the measurement instruments used can also influence the test data. Different sets of stress-strain curves that vary in range of strain rate and temperature often produce different model constants, which—in turn—affect the accuracy of the resulting JC model. Here, we consider three different sources of experimental data, and all available stress-strain curves generated by each experimental

source for different temperatures and strain rates are taken into account to obtain a complete range of values for all model constants.

b) Uncertainty in fitting method: Model constants should be found in such a way that the plasticity model fits experimental stress-strain curves of the material in different strain rates and temperatures. However, different fitting methods may yield different model constants. Here, we consider two different methods as suggested in the literature.

c) Model selection uncertainty: This type of uncertainty arises from the fact that in large deformation simulation, a single constitutive material model should be chosen from a set of existing alternative models as the most appropriate choice for analysis. However, there is no evidence to support the idea that the selected material model for a specific large deformation simulation provides more reliable results. As mentioned earlier, JC plasticity model can be represented by Eq. (3.1) or one of its variants resulting in an epistemic uncertainty about the formulation that provides more reliable results. In order to address this issue, two different forms of JC material model are considered.

4.1.1 Sources of experimental stress-strain curves

Obtaining a valid test data that accurately represents dependency of mechanical properties of a material on strain rate and temperature requires a test system that is capable of a) producing the required dynamic loads; b) obtaining the stress state at a desired point of a specimen; and c) measuring the stress and stress rates at the selected point (Hoge, 1966). Various testing techniques have been suggested to address each of these requirements. However, the resulting test data is always subject to uncertainty. Here, we consider three different experimental sources for modeling uncertainty in test data for 6061-T6 Aluminum alloy.

For experimental source 1, compression data at high rates are obtained using a split Hopkinson pressure bar (SHPB) apparatus (Nicholas, 1982) The technique considers the transmission of a stress wave through the specimen that is sandwiched between two elastic bars to obtain high-rate stress-strain curves. Holt et al. (1967) describe the method of analysis with discussion of error in strain rate, as well as stress and strain measurements. As for quasi-static and intermediate rate compression data, an MTS servo-controlled hydraulic testing machine was used to provide the stress-strain curves (Nicholas, 1982). Johnson and Holmquist (1989) provide torsion and tension test data for both quasi-static and dynamic loading cases at low and high temperatures.

Data (Hoge, 1963) for dynamic tensile loads are used for experimental source 2. As reported by Hoge (1966), a Dynapak metalworking machine that is modified into a test fixture and is capable of producing the required dynamic loads for uniaxial and certain biaxial tensile loads is used to obtain dynamic stress-strain curves. Also, the static tests (Hoge, 1966) were done on a Baldwin universal testing machine.

As for experimental source 3, dynamic data provided by Lee et al. (2000) is used. Dynamic compression tests with SHPB were carried out at room temperature under strain rates ranging from 1000 s^{-1} to 4000 s^{-1} (Lee et al., 2000). Tension experimental data (Gray et al., 1994) for both dynamic and static tests are also used as part of experimental source 3.

Table 4.1 summarizes the testing conditions for all three experimental sources used for determination of constants in JC model.

Table 4.1 Testing conditions for three experimental sources of data

Curve #	*Experimental Source 1*			Curve #	*Experimental Source 1*(*Continued*)		
	Type	Strain Rate (s^{-1})	Temperature (K)		Type	Strain Rate (s^{-1})	Temperature (K)
1	Tension	634	605	11	Torsion	11	293
2	Tension	627	505	12	Torsion	1	293
3	Tension	624	472	13	Torsion	0.001	293
4	Tension	622	293	14	Torsion	0.1	293
5	Torsion	99	293	15	Compression	800	293
6	Torsion	48	293	16	Compression	0.008	293
7	Torsion	39	293	17	Compression	40	293
8	Torsion	239	293	18	Compression	2	293
9	Torsion	130	293	19	Compression	0.1	293
10	Torsion	126	293	-	-	-	-
	Experimental Source 2				*Experimental Source 3*		
1	Tension	4.8e-5	297	1	Compression	1000	298
2	Tension	28	297	2	Compression	2000	298
3	Tension	65	297	3	Compression	3000	298
4	Tension	1e-05	533	4	Compression	4000	298
5	Tension	18	533	5	Tension	5.7E-04	373
6	Tension	130	533	6	Tension	1500	373
7	Tension	1e-05	644	7	Tension	5.7E-04	473
8	Tension	23	644	8	Tension	1500	473
9	Tension	54	644	-	-	-	-

4.1.2 Fitting methods of material constants

The following two fitting methods have been broadly adopted in the literature (Johnson and Cook, 1983; Holmquist and Johnson, 1991) for deriving the constants of JC plasticity model:

a) Method 1: In this method, the constants are fit simultaneously. Three stress-strain curves are selected from the available set of curves corresponding to each experimental source listed in Table 4.1. Curve *a* corresponds to low strain rate/room temperature (isothermal stress-strain curve) to consider flow stress behavior at constant temperature and strain rate, curve *b* corresponds to high strain rate/room temperature, and curve *c* corresponds to high temperature/low-to-medium strain rate condition. (Holmquist and Johnson, 1991) From curve *a*, three points are chosen, one corresponding to the yield point, one corresponding to the initial stage of work hardening, and one corresponding to

high strain level. Additionally, one point is selected from curve *b* and another from curve *c*, both corresponding to the initial stage of work hardening. The result is five equations in five unknowns that are solved simultaneously to find the constants in Johnson-Cook model in Eq. (3.1).

b) Method 2: In this method, the constants are fit in three separate stages. First, the yield and strain hardening constants (*A, B, n*) are obtained from isothermal tests at relatively low strain rates. Then, the strain rate constant, *C* is determined from curves at different strain rates. Finally, the thermal softening constant, *m* is determined from test data at various temperatures. In all stages, the nonlinear least squares method is used to find the respective constants. Johnson and Cook (1983) provide detailed information on the fitting approach to determine the five constants.

4.1.3 Determination of uncertainty intervals for five model constants

To recap, we have multiple stress-strain curves from three sources of experimental data, two models of JC based on the use of Eq. (3.2) or (3.3) for non-dimensional temperature, and two methods for fitting the constants in Eq. (3.1). For accurate uncertainty quantification, all possible combinations of stress-strain curves stemming from different experimental sources (as listed in Table 4.1), models of non-dimensional temperature, and fitting methods must be considered when deriving the constants in Eq. (3.1). Here, models 1 and 2 refer to Eqs. (3.2) and (3.3), respectively. Table 4.2 lists the number of feasible sets of constants (*A, B, n, C,* and *m*) that can be derived from the selected combination of factors (i.e., experimental source, model, and method). Each feasible set represents a piece of evidence that will be used in the representation of epistemic uncertainty as discussed later.

Following the selection of the feasible sets of constants, it is necessary to construct histograms to help identify the number of data points in each disjoint interval for a specific constant. The choice of intervals is based on adequate separation of the large dataset to reveal the significance of the number of data points (evidence) within each interval. In Tables 4.3 and 4.4, the number of intervals along with the range and quantity of data points within each interval are specified in lieu of plotting individual histograms. Intervals with substantially small number of data points are excluded in Tables 4.3 and 4.4 for brevity, although all data points are included in the actual analysis.

Table 4.2 Combination of factors and resulting number of feasible sets of constants

Experimental Source 1 Model 1		Experimental Source 2 Model 1		Experimental Source 3 Model 1	
Method 1	Method 2	Method 1	Method 2	Method 1	Method 2
4220	2853	50	38	52	60
Model 2		Model 2		Model 2	
3470	2852	40	38	36	60

Table 4.3 Distribution of intervals and range of values for constants of Johnson-Cook model 1

Interval	Experimental Source 1		Experimental Source 2		Experimental Source 3	
	Range	Data No.	Range	Data No.	Range	Data No.
Constant A, Fitting Method 1						
1	[90.40, 127.18]	210	[144.53, 165.70]	4	[227.00, 253.15]	24
2	[127.18, 163.96]	120	[208.05, 229.22]	30	[331.61, 357.76]	20
3	[163.96, 200.74]	245	[229.22, 250.40]	10	[357.76, 383.91]	8
4	[200.74, 237.51]	1395	[250.40, 271.57]	6	-	-
5	[237.51, 274.29]	1330	-	-	-	-
6	[274.29, 311.07]	920	-	-	-	-
Constant A, Fitting Method 2						
1	[254.00, 260.5]	688	[222.00, 241.33]	20	[227.00, 244.00]	24
2	[260.50, 267.00]	555	[260.67, 280.00]	18	[312.00, 329.00]	36
3	[273.50, 280.00]	909	-	-	-	-
4	[280.00, 286.50]	411	-	-	-	-
5	[286.50, 293.00]	290	-	-	-	-
Constant B, Fitting Method 1						
1	[11.51, 99.30]	3425	[6.37, 76.77]	34	[38.96, 121.35]	24
2	[99.30, 187.09]	610	[76.77, 147.19]	12	[121.35, 203.74]	16
3	[187.09, 274.89]	95	[147.19, 217.59]	2	[203.74, 286.13]	4
4	[274.89, 362.68]	45	[499.23, 569.64]	2	[368.52, 450.91]	4

Table 4.3 (Continued)

5	[11.51,1416.20]	45	-	-	[615.69, 698.08]	4
Constant B, Fitting Method 2						
1	[100.86, 113.55]	1847	[324.51, 341.00]	21	[127.62, 133.36]	30
2	[113.55, 126.24]	467	[439.94, 456.43]	17	[167.81, 173.35]	30
3	[138.93, 151.2]	362	-	-	-	-
4	[164.31, 177.00]	177	-	-	-	-
Constant n, Fitting Method 1						
1	[0, 0.618]	3620	[0, 0.0398]	34	[0, 0.2588]	6
2	[0.618, 1.235]	435	[0.0398, 0.0797]	6	[0.2588, 0.5175]	12
3	[1.235, 1.853]	100	[0.0797, 0.1195]	2	[0.5175, 0.7763]	20
4	[1.853, 2.470]	15	[0.1195, 0.1594]	2	[1.2938, 1.5525]	4
5	[2.470, 4.940]	50	[0.1992, 0.2390]	6	-	-
Constant n, Fitting Method 2						
1	[0.127, 0.179]	329	[0.4450, 0.4664]	17	[0.5467, 0.5735]	30
2	[0.179, 0.230]	1369	[0.5520, 0.5730]	21	[0.6811, 0.7080]	30
3	[0.281, 0.333]	1162	-	-	-	-
Constant C, Fitting Method 1						
1	[0, 0.057]	3235	[0.005, 0.0297]	40	[0.0078, 0.0152]	36
2	[0.057, 0.111]	410	[0.029, 0.054]	6	[0.0152, 0.023]	8
3	[0.111, 0.170]	135	[0.226, 0.250]	4	[0.023, 0.0299]	4
4	[0.170, 0.227]	165	-	-	[0.074, 0.0813]	4
5	[0.227, 0.284]	15	-	-	-	-
6	[0.284, 0.341]	60	-	-	-	-
7	[0.341, 0.397]	150	-	-	-	-
8	[0.454, 0.511]	15	-	-	-	-
9	[0.511, 0.568]	35	-	-	-	-
Constant C, Fitting Method 2						
1	[0, 0.009]	1017	[0.0034, 0.011]	12	[0.0052, 0.0173]	30
2	[0.009, 0.018]	944	[0.019, 0.026]	6	[0.0173, 0.029]	6
3	[0.018, 0.026]	605	[0.019, 0.034]	6	[0.042, 0.054]	2
4	[0.026, 0.035]	235	[0.049, 0.056]	5	[0.054, 0.066]	8
5	[0.035, 0.044]	52	[0.056-, 0.064]	5	[0.066, 0.078]	14
6	-	-	[0.072, 0.0792]	4	-	-
Constant m, Fitting Method 1						
1	[0.623, 0.966]	975	[0.675, 1.074]	6	[0.488, 0.689]	32
2	[0.966, 1.309]	1460	[1.074, 1.474]	28	[1.091, 1.263]	16
3	[1.309, 1.652]	610	[1.474, 1.873]	6	[1.494, 1.693]	4
4	[1.652, 1.995]	1175	[2.272, 2.671]	6	-	-
5			[2.671, 3.071]	4	-	-
Constant m, Fitting Method 2						
1	[0.897, 2.273]	1740	[0.285, 1.046]	8	[0.633, 0.699]	25
2	[2.273, 3.649]	907	[1.046, 1.807]	9	[0.699, 0.765]	4
3	[3.649, 5.026]	171	[1.807, 2.568]	21	[0.765, 0.831]	5
4	[5.026, 6.402]	29	-	-	[0.831, 0.897]	2
5	[6.402, 7.779]	5	-	-	[0.897, 0.963]	8
6	[7.779, 9.155]	1	-	-	[0.963, 1.030]	16

Table 4.4 Distribution of intervals and range of values for constants of Johnson-Cook model 2

Interval #	Experimental Source 1		Experimental Source 2		Experimental Source 3	
	Interval	Data No	Interval	Data No	Interval	Data No
Constant A, Fitting Method 1						
1	[107.1, 191.3]	150	[145.9, 167.4]	4	[226.6, 233.8]	28
2	[191.3, 149.2]	125	[210.5, 232.1]	32	[233.8, 241.0]	4
3	[149.2, 233.3]	1340	[253.6, 275.1]	4	[262.7, 269.9]	4
4	[233.3, 275.4]	940	-	-	-	-
5	[275.4, 317.5]	835	-	-	-	-
6	[317.5, 359.6]	80	-	-	-	-
Constant A, Fitting Method 2						
1	[254.0, 260.5]	688	[222.0, 241.3]	20	[227.0, 244.0]	24
2	[260.5, 267.0]	555	[260.7, 280.0]	18	[312.0, 329.0]	36
3	[273.5, 280.0]	908	-	-	-	-
4	[280.0, 286.5]	411	-	-	-	-
5	[286.5, 293.0]	290	-	-	-	-
Constant B, Fitting Method 1						
1	[14.96, 91.36]	2850	[42.26, 55.38]	28	[34.98, 49.57]	8
2	[91.36, 167.8]	450	[55.38, 68.49]	2	[49.57, 64.16]	24
3	[167.8, 244.2]	130	[68.49, 81.6]	4	[137.1, 151.7]	4
4	[244.2, 320.6]	25	[81.6, 94.7]	2	-	-
5	[320.6, 1237.3]	15	[94.7, 107.8]	2	-	-
6			[134.0, 147.2]	2	-	-
Constant B, Fitting Method 2						
1	[100.9, 113.6]	1846	[324.5, 341.0]	21	[127.6, 133.4]	30
2	[113.6, 126.2]	467	[439.9, 456.4]	17	[167.8, 173.4]	30
3	[138.9, 151.6]	362	-	-	-	-
4	[164.3, 177.0]	177	-	-	-	-
Constant n, Fitting Method 1						
1	[0.0, 0.615]	3060	[0.0, 0.0398]	30	[0.0, 0.118]	28
2	[0.615, 1.230]	255	[0.0398, 0.08]	2	[0.236, 0.354]	4
3	[1.230, 1.845]	80	[0.08, 0.1195]	2	[0.590, 0.708]	4
4	[1.845, 2.64]	10	[0.1991, 0.239]	6	-	-
5	[2.64, 3.255]	30	-	-	-	-
6	[3.255, 4.921]	35	-	-	-	-
Constant n, Fitting Method 2						
1	[0.127, 0.179]	322	[0.445, 0.466]	17	[0.547, 0.574]	30
2	[0.179, 0.230]	1368	[0.552, 0.573]	21	[0.681, 0.708]	30
3	[0.281, 0.333]	1162	-	-	-	-
Constant C, Fitting Method 1						
1	[0.0, 0.065]	2340	[0.005, 0.033]	24	[0.002, 0.029]	8
2	[0.065, 0.130]	750	[0.033, 0.061]	10	[0.029, 0.056]	12
3	[0.130, 0.195]	110	[0.061, 0.089]	2	[0.056, 0.083]	12
4	[0.195, 0.260]	20	[0.229, 0.257]	2	[0.136, 0.163]	4
5	[0.260, 0.649]	250	[0.257, 0.285]	2	-	-
Constant C, Fitting Method 2						
1	[0.0, 0.01]	1265	[0.0034, 0.011]	12	[0.005, 0.017]	30
2	[0.01, 0.022]	1056	[0.0186, 0.0262]	6	[0.0173, 0.029]	6
3	[0.022, 0.033]	442	[0.0262, 0.0337]	6	[0.042, 0.054]	2
4	[0.033, 0.044]	89	[0.0489, 0.0564]	5	[0.054, 0.066]	8
5	-	-	[0.0564, 0.064]	5	[0.066, 0.078]	14
6	-	-	[0.0716, 0.0792]	4	-	-
Constant m, Fitting Method 1						
1	[1.014, 1.486]	1535	[1.1166, 1.806]	30	[0.935, 1.191]	4
2	[1.486, 1.959]	390	[1.806, 2.486]	4	[1.191, 1.448]	28
3	[1.959, 2.431]	315	[3.166, 3.845]	2	[2.217, 2.474]	4

Table 4.4 (Continued)

4	[2.431, 2.903]	690	[3.845, 4.525]	2	-	-
5	[2.903, 3.325]	540	[4.525, 5.205]	2	-	-
Constant m, Fitting Method 2						
1	[1.39, 3.06]	1423	[0.316, 1.147]	7	[1.031, 1.133]	3
2	[3.06, 4.74]	987	[1.147, 1.979]	3	[1.133, 1.235]	4
3	[4.74, 6.41]	302	[1.979, 2.809]	21	[1.235, 1.340]	11
4	[6.41, 8.08]	106	[2.809, 3.641]	7	[1.340, 1.440]	13
5	[8.08, 9.76]	29	-	-	[1.440, 1.541]	13
6	[9.76, 11.43]	5	-	-	[1.541, 1.643]	13

4.1.4 Construction of belief structure for five model constants

The methodology introduced in chapter 2 is used to construct BBA for individual intervals of uncertainty for each constant. Tables 4.5 and 4.6 show the constructed BBA for uncertainty intervals of constants in JC models 1 and 2, respectively.

The charts in Figure 4.1 depict the process of constructing BBA for constants *A, n* and *m* using the 4220 data points corresponding to experimental source 1 and method 1 in Table 4.3. Among all intervals for constant *A*, interval 4 has the largest number of data points and is in agreement with interval 5 (see Figure 4.1(a)). Hence, intervals 4 and 5 are combined into a single interval resulting in m ([200.74, 274.29]) = 0.646. Comparing the data points in interval 6 with the average of those in intervals 4 and 5, we find conflict that requires a separate BBA with m ([274.29, 311.07]) = 0.218. Intervals 1, 2, and 3 are in ignorance with intervals 4 and 5. Here, it is possible to have either a single ignorance interval that extends from interval 1 to 5 or two separate intervals, one covering intervals 1, 2, 3, 4, and 5 with another covering intervals 3, 4, and 5 as shown in Figure 4.1(a). Here, the second choice is selected resulting in the following BBA structure: m ([163.96, 274.29]) = 0.218 and m ([90.4, 274.29]) = 0.078 (see Table 4.5).

In Figure 4.1(b), interval 1 has the highest number of data points for constant *n*, and the other disjointed intervals are in ignorance relationship with it. Since ignorance

interval 2 includes significantly larger number of data as opposed to the other intervals with ignorance data, two ignorance BBAs are selected, one covering intervals 1, 2 with value of m = 0.103 and the other covering all intervals with value of m = 0.039 (see Table 4.5). Although it is possible to have one BBA covering all intervals with value of m = 0.142 (sum of 0.103 and 0.039), the divided BBA gives a more precise representation of epistemic uncertainty. To consider data points of interval 1, a BBA of 0.858 is assigned to it (see Table 4.5).

In Figure 4.1(c), the highest data points belong to interval 2 with m = 0.345. Of its two adjacent intervals, interval 2 is in conflict with 1 and ignorance with 3 (see Table 4.5). Data points in interval 4 should be compared by interval 2 as its adjacent interval (interval 3) includes ignorance data. It is noticed that data points of interval 4 are in conflict relationship with interval 2 and the associated conflict BBA is found to be 0.278 as noted in Table 4.5.

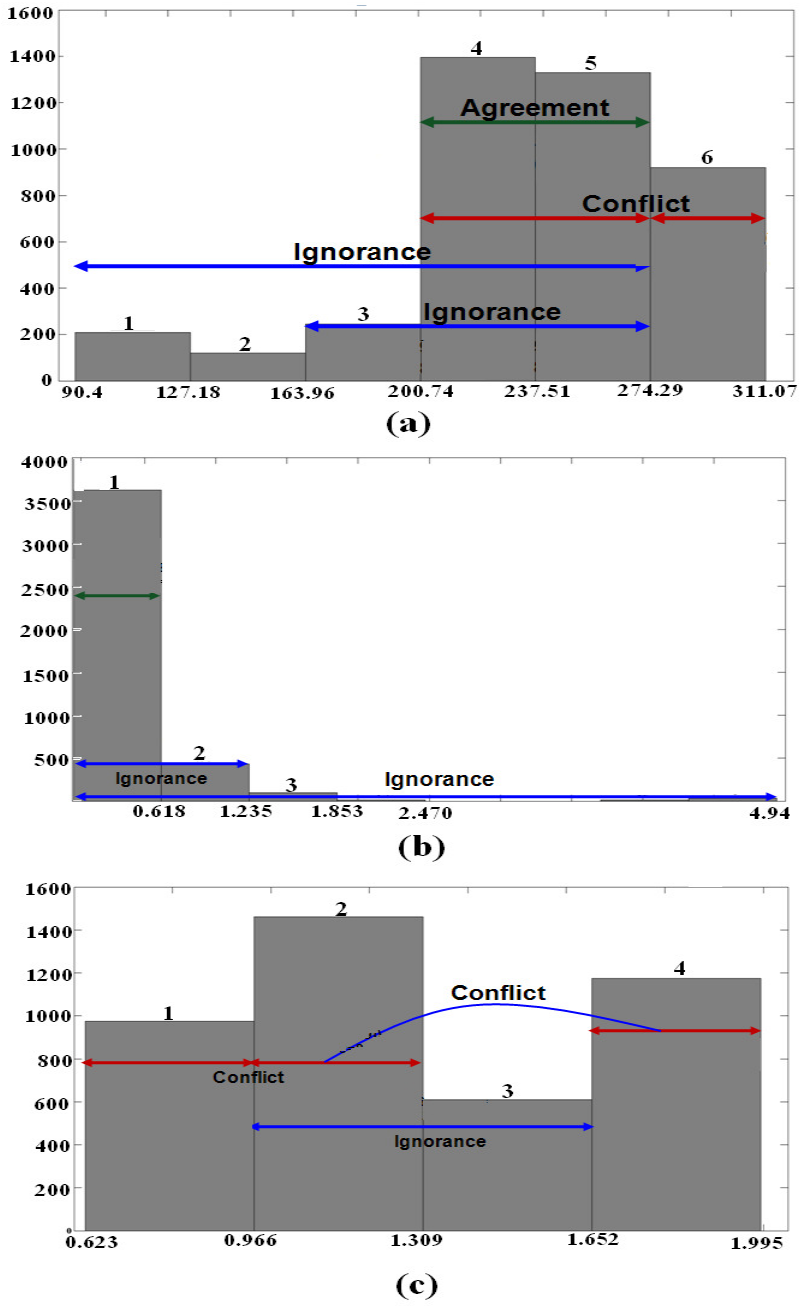

Figure 4.1 Histograms showing intervals of uncertainty for (a) A, (b) n and (c) m for the combination of source 1, method 1, and model 1

Table 4.5 Distribution of intervals and BBA values for constants of Johnson-Cook model 1

Interval #	Experimental Source 1		Experimental Source 2		Experimental Source 3	
	Interval	BBA	Interval	BBA	Interval	BBA
			Constant A, Fitting Method 1			
1	[200.74, 274.29]	0.646	[208.05, 229.22]	0.6	[227, 253.15]	0.462
2	[274.29, 311.07]	0.218	[208.05, 250.4]	0.2	[331.61, 357.76]	0.385
3	[163.96, 274.29]	0.058	[208.05, 271.57]	0.12	[331.61, 383.91]	0.153
4	[90.4, 274.29]	0.078	[144.53, 229.22]	0.08		
			Constant A, Fitting Method 2			
1	[254, 267]	0.436	[222, 241.33]	0.526	[227, 244]	0.4
2	[273.5, 280]	0.319	[260.67, 280]	0.478	[312, 329]	0.6
3	[273.5, 286.5]	0.144	-	-	-	-
4	[273.5, 293]	0.102	-	-	-	-
			Constant B, Fitting Method 1			
1	[11.51, 99.3]	0.812	[6.37, 76.77]	0.68	[39.958, 121.35]	0.462
2	[11.51, 187.09]	0.145	[6.37, 147.19]	0.24	[121.35, 203.74]	0.308
3	[11.51, 1416.2]	0.043	[6.37, 569.64]	0.08	[121.35, 698.08]	0.23
			Constant B, Fitting Method 2			
1	[100.86, 113.55]	0.647	[324.51, 341]	0.553	[127.62, 133.36]	0.5
2	[100.86, 126.24]	0.164	[439.94, 456.43]	0.447	[167.81, 173.35]	0.5
3	[100.86, 177]	0.189	-	-	-	-
			Constant n, Fitting Method 1			
1	[0, 0.618]	0.858	[0, 0.0398]	0.68	[0, 0.2588]	0.308
2	[0, 1.235]	0.103	[0, 0.239]	0.32	[0.2588, 0.5175]	0.231
3	[0, 4.94]	0.039	-	-	[0.5175, 0.7763]	0.385
4	-	-	-	-	[0.5175, 1.5525]	0.076
			Constant n, Fitting Method 2			
1	[0.127, 0.230]	0.113	[0.445, 0.4664]	0.447	[0.5467, 0.5735]	0.5
2	[0.179, 0.230]	0.48	[0.552, 0.573]	0.553	[0.6811, 0.708]	0.5
3	[0.281, 0.333]	0.407	-	-	-	-
			Constant C, Fitting Method 1			
1	[0, 0.057]	0.767	[0.005, 0.0297]	0.8	[0.0078, 0.0152]	0.692
2	[0, 0.111]	0.097	[0.005, 0.0542]	0.12	[0.0078, 0.0812]	0.308
3	[0, 0.568]	0.136	[0.005, 0.2504]	0.08	-	-
			Constant C, Fitting Method 2			
1	[0, 0.018]	0.687	[0.0034, 0.011]	0.316	[0.0052, 0.0173]	0.5
2	[0.018, 0.026]	0.212	[0.0034, 0.0792]	0.684	[0.0052, 0.029]	0.1
3	[0.018, 0.044]	0.101	-	-	[0.042, 0.078]	0.167
4	-	-	-	-	[0.066, 0.078]	0.233
			Constant m, Fitting Method 1			
1	[0.623, 0.966]	0.231	[1.074, 1.4737]	0.56	[0.488, 0.689]	0.615
2	[0.966, 1.309]	0.346	[0.675, 1.8729]	0.24	[1.091, 1.2626]	0.308
3	[0.966, 1.652]	0.144	[1.074, 3.0706]	0.2	[1.091, 1.6948]	0.077
4	[1.652, 1.995]	0.278	-	-	-	-
			Constant m, Fitting Method 2			
1	[0.897, 2.273]	0.61	[0.285, 2.568]	0.447	[0.6326, 2.699]	0.417
2	[2.273, 3.649]	0.318	[1.807, 2.568]	0.553	[0.6326, 0.897]	0.183
3	[0.897, 9.155]	0.072	-	-	[0.897, 1.03]	0.133
4	-	-	-	-	[0.963, 1.03]	0.267

Table 4.6 Distribution of intervals and BBA values for constants of Johnson-Cook model 2

Interval #	Experimental Source 1		Experimental Source 2		Experimental Source 3	
	Interval	Data No	Interval	Data No	Interval	Data No
Constant A, Fitting Method 1						
1	[107.1, 191.3]	150	[145.9, 167.4]	4	[226.6, 233.8]	28
2	[191.3, 149.2]	125	[210.5, 232.1]	32	[233.8, 241.0]	4
3	[149.2, 233.3]	1340	[253.6, 275.1]	4	[262.7, 269.9]	4
4	[233.3, 275.4]	940	-	-	-	-
5	[275.4, 317.5]	835	-	-	-	-
6	[317.5, 359.6]	80	-	-	-	-
Constant A, Fitting Method 2						
1	[254.0, 260.5]	688	[222.0, 241.3]	20	[227.0, 244.0]	24
2	[260.5, 267.0]	555	[260.7, 280.0]	18	[312.0, 329.0]	36
3	[273.5, 280.0]	908	-	-	-	-
4	[280.0, 286.5]	411	-	-	-	-
5	[286.5, 293.0]	290	-	-	-	-
Constant B, Fitting Method 1						
1	[14.96, 91.36]	2850	[42.26, 55.38]	28	[34.98, 49.57]	8
2	[91.36, 167.8]	450	[55.38, 68.49]	2	[49.57, 64.16]	24
3	[167.8, 244.2]	130	[68.49, 81.6]	4	[137.1, 151.7]	4
4	[244.2, 320.6]	25	[81.6, 94.7]	2	-	-
5	[320.6, 1237.3]	15	[94.7, 107.8]	2	-	-
6			[134.0, 147.2]	2	-	-
Constant B, Fitting Method 2						
1	[100.9, 113.6]	1846	[324.5, 341.0]	21	[127.6, 133.4]	30
2	[113.6, 126.2]	467	[439.9, 456.4]	17	[167.8, 173.4]	30
3	[138.9, 151.6]	362	-	-	-	-
4	[164.3, 177.0]	177	-	-	-	-
Constant n, Fitting Method 1						
1	[0.0, 0.615]	3060	[0.0, 0.0398]	30	[0.0, 0.118]	28
2	[0.615, 1.230]	255	[0.0398, 0.08]	2	[0.236, 0.354]	4
3	[1.230, 1.845]	80	[0.08, 0.1195]	2	[0.590, 0.708]	4
4	[1.845, 2.64]	10	[0.1991, 0.239]	6	-	-
5	[2.64, 3.255]	30	-	-	-	-
6	[3.255, 4.921]	35	-	-	-	-
Constant n, Fitting Method 2						
1	[0.127, 0.179]	322	[0.445, 0.466]	17	[0.547, 0.574]	30
2	[0.179, 0.230]	1368	[0.552, 0.573]	21	[0.681, 0.708]	30
3	[0.281, 0.333]	1162	-	-	-	-
Constant C, Fitting Method 1						
1	[0.0, 0.065]	2340	[0.005, 0.033]	24	[0.002, 0.029]	8
2	[0.065, 0.130]	750	[0.033, 0.061]	10	[0.029, 0.056]	12
3	[0.130, 0.195]	110	[0.061, 0.089]	2	[0.056, 0.083]	12
4	[0.195, 0.260]	20	[0.229, 0.257]	2	[0.136, 0.163]	4
5	[0.260, 0.649]	250	[0.257, 0.285]	2	-	-
Constant C, Fitting Method 2						
1	[0.0, 0.01]	1265	[0.0034, 0.011]	12	[0.005, 0.017]	30
2	[0.01, 0.022]	1056	[0.0186, 0.0262]	6	[0.0173, 0.029]	6
3	[0.022, 0.033]	442	[0.0262, 0.0337]	6	[0.042, 0.054]	2
4	[0.033, 0.044]	89	[0.0489, 0.0564]	5	[0.054, 0.066]	8
5	-	-	[0.0564, 0.064]	5	[0.066, 0.078]	14
6	-	-	[0.0716, 0.0792]	4	-	-
Constant m, Fitting Method 1						
1	[1.014, 1.486]	1535	[1.1166, 1.806]	30	[0.935, 1.191]	4
2	[1.486, 1.959]	390	[1.806, 2.486]	4	[1.191, 1.448]	28
3	[1.959, 2.431]	315	[3.166, 3.845]	2	[2.217, 2.474]	4

Table 4.6 (Continued)

4	[2.431, 2.903]	690	[3.845, 4.525]	2	-	-
5	[2.903, 3.325]	540	[4.525, 5.205]	2	-	-
Constant m, Fitting Method 2						
1	[1.39, 3.06]	1423	[0.316, 1.147]	7	[1.031, 1.133]	3
2	[3.06, 4.74]	987	[1.147, 1.979]	3	[1.133, 1.235]	4
3	[4.74, 6.41]	302	[1.979, 2.809]	21	[1.235, 1.340]	11
4	[6.41, 8.08]	106	[2.809, 3.641]	7	[1.340, 1.440]	13
5	[8.08, 9.76]	29	-	-	[1.440, 1.541]	13
6	[9.76, 11.43]	5	-	-	[1.541, 1.643]	13

4.1.5 Final representation of uncertainty in Johnson-Cook constants

As indicated in Tables 4.5 and 4.6, consideration of all the factors that influence uncertainty in the JC constants results in different belief structures. However, the uncertainty in each constant must be represented by only a single belief structure that accounts for the aforementioned factors that contribute to it. Here, the Yager's combination rule (1987, 1987a) of evidence as discussed in Section 2.2 is adopted. Conceptually, Yager's rule assigns a BBA to the intersection of two intervals of uncertainty from different sources of evidence. Intervals of uncertainty that are in agreement between different sources are treated as valid evidence. In the case of no intersection (conflict between two intervals of uncertainty from different sources), Yager's rule allocates the associated conflicting BBA to the universal set. In fact, Yager's rule considers conflict between two uncertainty intervals as ignorance or lack of knowledge, and—as a result—assigns a BBA to ignorance interval (universal set). Here, for single representation of uncertainty, the following steps are performed:

1- For each model and experimental source, Yager's rule is used to combine belief structures associated with different fitting methods for individual constants of JC model.

2- Belief structures of all experimental sources are combined to find a single (final) belief structure for each constant in models 1 and 2, separately.

The combined belief structure following step 1 together with the final BBA values obtained from step 2 are listed in Tables 4.7 and 4.8 for JC models 1 and 2, respectively. To reduce the size of each table, the final BBA values shown in bottom rows of Tables 4.7 and 4.8 correspond to the intervals identified in column 1 and separated by commas.

Table 4.7 Combined and final BBA for constants of Johnson-Cook model 1

Element#	Interval	BBA	Interval	BBA	Interval	BBA
			Constant A			
1, 5, 9	[260.67, 267.00]	0.0158	[227.00, 229.22]	0.0336	[227.00, 280.00]	0.0320
2, 6, 10	[254.00, 267.00]	0.1159	[227.00, 241.33]	0.0158	[90.40, 383.91]	0.5832
3, 7	[273.50, 274.29]	0.1502	[260.67, 271.57]	0.0044	-	-
4, 8	[274.29, 280.00]	0.0419	[227.00, 244.00]	0.0072	-	-
			Constant B			
1, 4, 7	[100.85, 113.55]	0.0517	[167.81, 173.35]	0.2097	[439.93, 456.43]	0.0134
2, 5, 8	[100.85, 126.24]	0.0131	[100.85, 177.00]	0.0151	[38.95, 569.64]	0.3451
3, 6, 9	[127.62, 133.36]	0.2097	[324.50, 341.00]	0.0166	[6.37, 698.08]	0.1255
			Constant n			
1, 3	[0.1269, 0.2303]	0.0879	[0.2810, 0.3333]	0.3166	-	-
2, 4	[0.1787, 0.2303]	0.3734	[0, 1.5525]	0.2221	-	-
			Constant C			
1, 5, 9	[0.0077, 0.0113]	0.1303	[0.0077, 0.0183]	0.0145	[0.0177, 0.0300]	0.0176
2, 6, 10	[0.0051, 0.0113]	0.0601	[0.0051, 0.0183]	0.1301	[0.0420, 0.0443]	0.0003
3, 7, 11	[0.0077, 0.0154]	0.1951	[0.0177, 0.0263]	0.0446	[0.0177, 0.0443]	0.0015
4, 8, 12	[0.0077, 0.0175]	0.0724	[0.0177, 0.0292]	0.0021	[0, 0.08126]	0.3315
			Constant m			
1, 7, 13	[0.8967, 0.9663]	0.0309	[1.0740, 1.4740]	0.0491	[1.0908, 1.6950]	0.0043
2, 8, 14	[1.0908, 1.2626]	0.0559	[1.0908, 1.6520]	0.0013	[0.6747, 1.6949]	0.0161
3, 9, 15	[1.0908, 1.3090]	0.0051	[0.9657, 1.6520]	0.0192	[0.6324, 0.6890]	0.0364
4, 10, 16	[1.0740, 1.3090]	0.0278	[1.6517, 1.6950]	0.0025	[0.6230, 1.6949]	0.0464
5, 11, 17	[0.9657, 1.3090]	0.0463	[1.6517, 1.6949]	0.0372	[0.285, 9.155]	0.6054
6, 12	[1.0908, 1.4740]	0.0034	[0.6747, 0.6890]	0.0126	-	-

Table 4.8 Combined and final BBA for constants of Johnson-Cook model 1

Element#	Interval	BBA	Interval	BBA	Interval	BBA
			Constant A			
1, 4, 7	[254.00, 267.00]	0.0811	[226.56, 232.05]	0.1174	[227.00, 241.01]	0.0120
2, 5, 8	[273.50, 280.00]	0.1048	[227.00, 233.79]	0.0838	[226.56, 280.00]	0.1616
3, 6, 9	[227.00, 232.05]	0.0783	[227.00, 244.00]	0.0120	[107.13, 359.56]	0.3491
			Constant B			
1, 4, 7	[100.85, 113.55]	0.1094	[100.85, 167.76]	0.0232	[14.96, 1237.30]	0.0080
2, 5	[100.85, 126.24]	0.0278	[100.85, 173.35]	0.0088	-	-
3, 6	[127.62, 133.36]	0.0474	[42.26, 173.35]	0.7754	-	-
			Constant n			
1, 3	[0.1269, 0.2303]	0.0879	[0.2810, 0.3333]	0.3166	-	-
2, 4	[0.1787, 0.2303]	0.3734	[0.0000, 0.7081]	0.2221	-	-
			Constant C			
1, 5, 9	[0.0051, 0.0113]	0.0421	[0.0047, 0.0223]	0.3094	[0.0047, 0.0443]	0.0047
2, 6, 10	[0.0047, 0.0113]	0.1756	[0.0051, 0.0292]	0.0028	[0.0023, 0.163]	0.3101
3, 7	[0.0051, 0.0175]	0.0759	[0.0047, 0.0331]	0.066	-	-
4, 8	[0.0051, 0.0223]	0.0124	[0.0420, 0.0443]	0.0011	-	-
			Constant m			
1, 7, 13	[1.3897, 1.4479]	0.2532	[1.3897, 2.4311]	0.0129	[1.1912, 1.5406]	0.0035
2, 8, 14	[1.3897, 1.4863]	0.0849	[2.4310, 2.4739]	0.0151	[1.1166, 1.8063]	0.0356
3, 9, 15	[1.5404, 1.6427]	0.0116	[1.2350, 1.4479]	0.1475	[1.9782, 2.4739]	0.0055
4, 10, 16	[1.3897, 1.5406]	0.0100	[1.1912, 1.4479]	0.0243	[1.1166, 2.4739]	0.0119
5, 11, 17	[1.3897, 1.8063]	0.0162	[1.1166, 1.4479]	0.0026	[1.0140, 2.4739]	0.0164
6, 12, 18	[1.9782, 2.4311]	0.0025	[1.2350, 1.5406]	0.0184	[0.3157, 11.43]	0.3282

4.2 Uncertainty representation of BCJ Plasticity Model

As shown in Table 4.9, depending on the selected sets of stress-strain curves at different strain rates and temperatures, the proposed fitting approach suggested in chapter 3 produces different values for some of the BCJ material constants for 7075-T651 aluminum alloy. Note that for all sets of material constants in Table 4.9, experimental data provided by Table 3.2 is used for determination of hardening constants (i.e., C_7 through C_{18}) that take the same values as those in Table 3.3. However, different sets of stress-strain curve as shown in Table 4.10 are used to fit the constants of BCJ flow equation, resulting in different sets of constants (i.e., C_1 through C_6) in Table 4.9. This variability in the calculated material constants is mainly because of the uncertainty in the experimental procedure used to obtain the stress-strain curves, inherent variability in material properties, existing uncertainty in the numerical nonlinear least-squares fitting

process, and incertitude or lack of knowledge in accurate modeling of the dynamic behavior of the material using the mathematical formulation of the BCJ plasticity model.

Considering the impact of BCJ material constants on simulation responses associated with a large deformation process (i.e., deep drawing, vehicle crash), it is necessary to quantify their uncertainty.

Table 4.9 BCJ material constants for 7075-T651 aluminum alloy obtained using different sets of stress-strain curves.

No	C_1 (MPa)	C_2 (K)	C_3 (MPa)	C_4 (K)	C_5 (1/s)	C_6 (K)
1	312.86	154.78	27.21	818.26	6914.10	233.39
2	406.37	182.63	22.67	890.84	7025.54	215.31
3	276.89	67.17	148.32	322.39	5829.39	155.30
4	304.34	167.24	31.88	670.20	7847.90	291.88
5	282.30	169.66	201.96	118.12	6697.24	249.90
6	368.68	247.98	178.41	250.38	8064.66	269.79
7	262.77	87.46	69.57	520.44	6229.10	186.33
8	339.31	205.59	137.33	317.34	6819.30	256.35
9	340.20	180.33	90.16	427.97	7532.25	293.39
10	333.46	167.69	35.31	736.58	7136.29	254.78
11	280.73	216.85	32.62	748.36	7398.12	258.42

Table 4.10 Testing conditions for the collected experimental data.

Curve No.	Ref. No.	Temperature (K)	Strain Rate (s^{-1})	Curve No.	Ref. No.	Temperature (K)	Strain Rate (s^{-1})
1	16	297	3100	9	15	673	10
2	16	297	2400	10	15	673	1
3	16	297	1300	11	15	673	0.1
4	14	297	0.1	12	15	673	0.01
5	15	573	10	13	15	723	10
6	15	573	1	14	15	723	1
7	15	573	0.1	15	15	723	0.1
8	15	573	0.01	16	15	723	0.01

Here, the available data for the BCJ material constants (see Table 4.9) is insufficient for assigning a particular probability density function (PDF) to each one, and

our knowledge of the constants and modeling the dynamic material behavior of metals is imprecise. Hence, based on the nature of uncertainty in the BCJ plasticity model and the capabilities of evidence theory, we adopted this theory for uncertainty modeling of the BCJ plasticity model. Following the methodology presented in chapter 2 for construction of belief structures of uncertain variables and using the available data on BCJ material constants given by Table 4.9, separate belief structures for material constants of BCJ plasticity model is constructed and provided by Table 4.11.

Table 4.11 Belief structures of material constants of BCJ flow equation for 7075-T651 aluminum alloy

Interval No.	C_1		C_2		C_3	
	Range	BBA	Range	BBA	Range	BBA
1	[262.03, 310.17]	5/11	[127.9, 187.83]	6/11	[22.30, 81.94]	6/11
2	[310.17, 358.31]	4/11	[67.95, 187.83]	2/11	[22.30, 141.57]	2/11
3	[310.17,406.45]	2/11	[187.83, 247.8]	3/11	[141.57, 201.2]	3/11
	C_4		C_5		C_6	
1	[633.9, 890.34]	5/11	[6574, 7319]	5/11	[241.2, 291.5]	7/11
2	[375.85, 890.34]	2/11	[7319, 8064]	4/11	[155.8, 291.5]	4/11
3	[118.6, 375.85]	4/11	[5829, 7319]	2/11		

CHAPTER V

UNCERTAINTY PROPAGATION AND QUANTIFICATION OF PLASTICITY MODELS

For the purpose of uncertainty quantification, the represented uncertainties in material constants should be propagated through the plasticity models in simulation of a large deformation process. Uncertainty propagation implies determination of the uncertainty intervals of the structural responses caused by incertitude in the material constants. The results from propagation will be used for an eventual estimation of belief and plausibility of each response for measuring the corresponding epistemic uncertainty.

Two illustrative examples are considered for uncertainty propagation. In the first example, the represented uncertainties in JC plasticity model are propagated through non-linear crush simulation of a 6061-T6 aluminum alloy circular tube under axial impact load, whereas in the second example, the uncertainties in BCJ plasticity model are propagated through non-linear simulation of a 7075-T651 aluminum alloy solid circular cylinder commonly referred to as Taylor impact test (Rule, 1997).

5.1 Uncertainty propagation of Johnson-Cook plasticity models

Using design and analysis of computer experiments, separate surrogate models based on JC Models 1 and 2 are developed. Then, a joint belief structure for the five material constants is established and used to determine the belief structure for the crush length based on each JC model. Finally, a global optimization technique is used to find the upper and lower bounds of crush length as described next.

5.1.1 Design and Analysis of Computer Experiments

Since repeated nonlinear transient dynamic finite element analysis (FEA) for the range of uncertain variables and associated belief structures would be computationally expensive, it is necessary to develop a surrogate model of each response to facilitate the uncertainty propagation process.

Radial Basis Functions (RBF) has been used successfully for fitting a wide range of response functions with different forms of nonlinearly and dimensionality. (Fang et al. 2005, 2008) Given the normalized values of design variable vector and the corresponding finite-element based responses (crush length) at n sampling (training) points, a multiquadric form of RBF approximation is used to approximate the true response function $f(\boldsymbol{Y})$ as

$$f'(\boldsymbol{Y}) = \sum_{i=1}^{n} \lambda_i \phi(\boldsymbol{r}_i) \tag{5.1}$$

where $r_i = \|\boldsymbol{Y} - \boldsymbol{Y}_i\| = \sqrt{(\boldsymbol{Y} - \boldsymbol{Y}_i)^T (\boldsymbol{Y} - \boldsymbol{Y}_i)}$ represents the normalized radial distance from an arbitrary design point to the ith training point with $\lambda_i,\ i = 1,n$ as the unknown interpolation coefficients given $\phi(\boldsymbol{r}_i) = \sqrt{\boldsymbol{r}_i^2 + c^2}$ and $0 < c \le 1$. Vector $\boldsymbol{Y}$ is found by normalizing each element of uncertain design variable vector $\boldsymbol{X}^T = [A,B,n,C,m]$ (material constants) by the respective upper bound value.

Here, Latin hypercube sampling (LHS) technique is adopted to generate 50 training points as identified in Table 5.1. Intervals of uncertainty (universal set) for all uncertain material constants (determined in chapter 4) in JC models 1 and 2 are considered in selecting the bounds on uncertain variables.

Four error metrics are used for assessment of metamodel accuracy. Since RBF is an interpolation model, five randomly selected test points within the global bounds of

each uncertain variable (see Table 5.2) are used for evaluation of R^2 and RSME statistics defined as

$$R^2 = 1 - SSE/SST \tag{5.2}$$

$$RMSE = \sqrt{SSE/m} \tag{5.3}$$

with SSE (sum of square errors) and SST (total sum of squares) calculated as

$$SSE = \sum_{i=1}^{m} [f_i - \hat{f}_i]^2 \tag{5.4}$$

$$SST = \sum_{i=1}^{m} [f_i - \bar{f}]^2 \tag{5.5}$$

where m is the number of test points, f_i is the finite element-based response value at ith test point, $\hat{f}_i$ is the corresponding approximate value calculated by the RBF model, and $\bar{f}$ is the mean value of f_i. Generally speaking, the larger the value of R^2 and the smaller the value of RMSE, the better the fit. In addition to these statistics, RBF model accuracy is also measured by finding the prediction error sum of squares (PRESS) and R^2 for prediction ($R^2_{prediction}$) at the training points. These statistics are calculated as

$$PRESS = \sum_{i=1}^{n-1} [f_i - \hat{f}_{(i)}]^2 \tag{5.6}$$

$$R^2_{Prediction} = 1 - PRESS/SST \tag{5.7}$$

where, $\hat{f}_{(i)}$ is the predicted value at the ith training point using the RBF model created by (n - 1) design points that exclude the ith point.

Table 5.1 Training points used in generating the RBF metamodels for crush length

Point No.	Johnson-Cook Model 1						Johnson-Cook Model 2					
	A (MPa)	B (MPa)	n	C	m	Crush Length (mm)	A (MPa)	B (MPa)	n	C	m	Crush Length (mm)
1	371.93	373.4	1.204	0.0116	3.91	8.26	277.13	1137.52	0.56351	0.0908	1.45	5.98
2	347.97	204.0	1.1089	0.0199	1.19	8.79	112.28	937.951	0.23118	0.1597	0.769	4.98
3	353.96	34.603	0.9188	0.0365	5.35	7.95	127.74	289.363	0.17339	0.1302	0.316	2.4
4	240.15	486.33	0.5386	0.005	4.81	9.47	349.26	913.006	0.15894	0.1564	3.038	3.1
5	306.04	472.22	0.0317	0.0083	0.83	5.03	132.89	139.689	0.40457	0.1368	5.079	10.852
6	186.24	246.35	1.0456	0.0531	4.27	12.55	122.58	1037.73	0.28898	0.0646	7.121	6.197
7	216.19	698.08	1.3941	0.063	3	10.66	210.16	538.82	0.08669	0.0974	5.533	4.14
8	144.31	161.65	0.7604	0.0746	7.16	14.14	266.83	14.96	0.10114	0.1236	2.811	6.81
9	114.36	62.836	1.1723	0.01	3.18	26.23	318.35	439.037	0.0289	0.0253	2.584	4.64

Table 5.1 (Continued)

10	276.09	91.069	0.0951	0.0431	0.47	7.82	179.25	513.874	0.37567	0.0941	8.028	7.43
11	90.4	627.5	1.5525	0.068	6.08	19.86	174.1	239.471	0.21673	0.0121	6.894	10.524
12	162.28	20.48	0.2852	0.0779	5.72	12.61	220.47	888.06	0.39012	0.0876	0.996	6.11
13	192.23	571.03	0.5703	0.0232	7.34	12.62	235.92	1062.68	0.36122	0.0384	3.265	6.12
14	210.2	387.52	0.697	0.0481	7.71	10.35	184.4	763.331	0.708	0.0515	3.945	10.108
15	132.33	105.19	1.4258	0.0249	8.43	21.22	241.07	39.9057	0.07224	0.1105	7.575	7.27
16	335.99	302.82	1.0772	0.0597	9.16	7.25	271.98	164.634	0.6502	0.081	6.44	7.76
17	96.39	585.15	0.3168	0.0315	7.53	9.35	328.65	663.549	0.13004	0.1171	2.357	3.51
18	222.18	556.91	0.0634	0.0166	4.99	5.04	313.2	788.277	0.66465	0.0154	8.255	7.458
19	228.17	528.68	0.4119	0.0813	1.37	7.03	143.19	264.417	0.20229	0.1433	7.348	7.032
20	270.1	288.7	1.3307	0.0398	7.89	9.70	163.8	613.657	0.18784	0.1072	10.07	5.24
21	150.3	429.87	0.8871	0.0149	6.62	15.03	308.04	414.091	0.11559	0.0613	5.987	4.78
22	318.02	260.47	0.2535	0.0299	8.79	6.94	107.13	1162.46	0.43347	0.163	1.223	6.56
23	174.26	48.72	0.7287	0.0464	2.46	14.00	261.68	1187.41	0.01445	0.0449	0.543	4.773
24	180.25	359.28	0.602	0.0796	3.54	10.06	251.38	863.114	0.46237	0.0318	9.843	7.24
25	108.37	514.57	0.1901	0.0265	2.64	7.98	168.95	688.494	0.44792	0.1466	2.13	6.74
26	365.94	189.88	1.3624	0.0547	6.8	7.014	297.74	563.766	0.26008	0.0187	9.616	4.81
27	294.06	345.17	0.9505	0.0017	5.9	10.29	215.31	389.146	0.24563	0.1335	1.904	5.59
28	300.05	655.73	0.8238	0.0348	6.98	8.23	205.01	64.8514	0.69355	0.1204	11.2	8.89
29	156.29	443.98	1.299	0.0514	0.65	15.59	359.56	89.7971	0.27453	0.0023	10.52	8.41
30	324.01	274.58	0.6654	0.0663	2.82	6.96	158.65	838.169	0.59241	0.104	5.76	8.43
31	204.21	415.75	0.2218	0.0415	1.55	7.32	302.89	638.603	0.52016	0.0581	1.677	6.66
32	246.14	175.77	1.1406	0.0010	8.07	13.54	323.5	987.843	0.50571	0.022	4.399	6.48
33	252.13	147.54	1.4891	0.0647	4.45	9.53	153.49	463.983	0.04335	0.1499	3.491	3.68
34	377.92	119.3	1.2357	0.0498	1.91	6.98	138.04	588.711	0.57796	0.0482	9.389	11.08
35	138.32	401.63	0.4753	0.0216	0.28	17.24	194.71	1087.63	0.0578	0.0843	5.306	2.96
36	341.98	599.26	0.1267	0.0564	1.01	4.34	225.62	1212.35	0.63576	0.0548	4.172	7.7
37	264.11	316.93	0.8555	0.0332	1.73	9.67	282.29	488.929	0.002	0.1138	7.802	3.11
38	282.08	133.42	0.9822	0.058	2.1	8.58	230.77	189.58	0.34678	0.1269	8.482	6.8
39	312.03	683.96	1.2673	0.0033	3.72	9.694	246.22	364.2	0.31788	0.0777	10.75	6.72
40	383.91	76.953	0.0010	0.0133	3.36	7.263	292.59	1012.79	0.49127	0.1532	4.853	4.77
41	198.22	613.38	1.4574	0.0381	8.97	12.61	287.44	738.386	0.33233	0.0712	3.718	5.48
42	359.95	641.61	0.3802	0.0713	6.26	5.2	148.34	813.223	0.6791	0.14	9.163	8.62
43	330	542.8	0.7921	0.0066	2.28	8.36	199.86	1237.3	0.60686	0.0417	8.936	8.22
44	258.12	6.37	0.1584	0.0182	6.44	11.65	256.53	713.44	0.62131	0.0679	6.214	7.48
45	288.07	458.1	0.5069	0.0282	5.17	7.89	344.11	214.526	0.41902	0.1007	4.626	5.56
46	168.27	232.23	1.5208	0.073	8.61	13.36	333.8	1112.57	0.30343	0.0285	6.667	4.99
47	234.16	218.12	1.0139	0.0763	4.63	9.31	117.43	339.254	0.54906	0.0089	8.709	15.99
48	120.35	669.85	0.6337	0.0448	4.09	11.57	338.95	962.897	0.53461	0.0351	11.43	6.34
49	126.34	500.45	0.4436	0.0614	8.25	10.57	354.41	314.309	0.47682	0.0056	10.98	7.7
50	102.38	331.05	0.3485	0.0697	5.53	11.79	189.56	114.743	0.14449	0.0745	10.3	8.91

Table 5.2 Test points used for accuracy evaluation of constructed RBF metamodels

Point	Johnson-Cook Model 1						Johnson-Cook Model 2					
	A (MPa)	B (MPa)	n	C	m	Crush Length (mm)	A (MPa)	B (MPa)	n	C	m	Crush Length (mm)
1	237.15	6.37	0.3881	0.0609	6.94	9.89	107.13	626.13	0.531	0.0425	8.65	11.23
2	310.53	352.23	0.0010	0.0203	4.72	5.2	233.35	14.96	0.354	0.1228	3.09	7.87
3	237.16	352.23	0.7763	0.0406	4.72	9.99	233.35	626.13	0.354	0.0827	5.87	6.25
4	90.40	179.30	1.1644	0.0406	2.50	26.25	170.24	931.72	0.177	0.0023	5.87	5.28
5	163.78	525.15	0.7763	0.0001	0.29	18.78	296.45	320.55	0.001	0.0827	0.32	7.12

5.1.2 Description of the FE Models

Axial crush simulations of all samples (Tables 5.1 and 5.2) are performed using explicit FEA code LS-DYNA, version 971. A rigid plate of 127-g mass is attached to 6161-T6 cylindrical tube of 76.2-mm length, 2.41-mm thickness and 11.495-mm mean radius. The tube and the attached mass traveling at an initial speed of 101.3 m/s collide into a rigid barrier perpendicular to the tube axis. The constructed FE model is shown in Figure 5.2, where a "single-surface" interface with friction coefficient of 0.1 is adopted to prevent penetration of contacting elements into the tube elements due to excessive deformation. Shell elements are used in all computer simulations. The sensitivity of the simulated results to mesh density was analyzed and element size of 1x1 mm was found to be suitable for valid simulation results. The material properties of the tube are modeled by JC material model. For each sample in the training set, material constants are selected from Table 5.1. Figures 5.3a and 5.3b show the collapsed shapes of the test samples for JC material Models 1 and 2, respectively. The differences in the results are due to the selected values of the material constants in Table 5.2. The response of interest is the crush length representing the amount by which the tube length is reduced after impact.

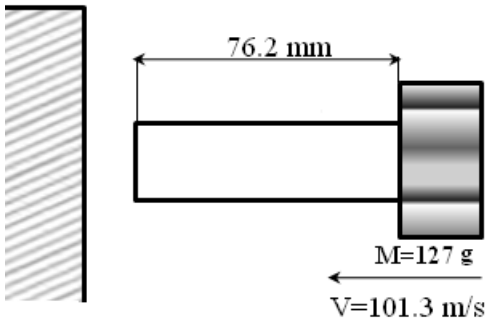

Figure 5.1 Finite element model of the impacted tube

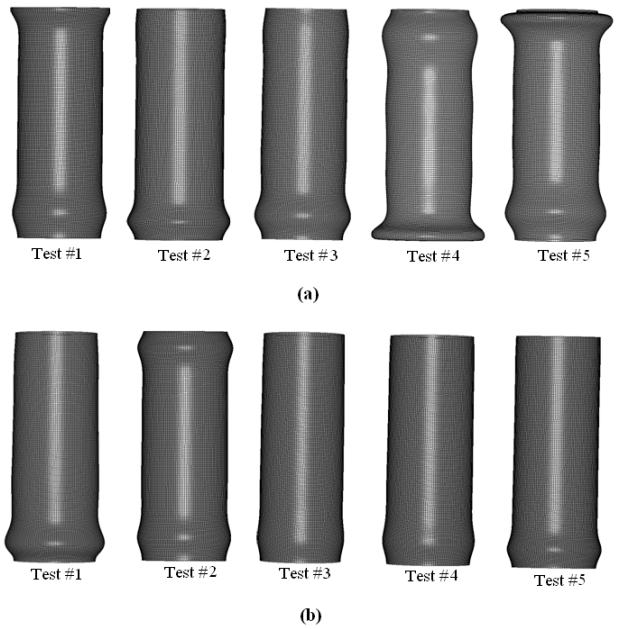

Figure 5.2 Collapsed shapes of selected test samples for (a) Johnson-Cook model 1 and (b) Johnson-Cook model 2 (Not to scale)

5.1.3 Evaluation of RBF Model Accuracy

The parameter c in $\phi(\boldsymbol{r}_i)$ can be used to fine-tune the RBF model to increase accuracy of the approximate crush length. For JC Models 1 and 2, c = 1 and 0.45, respectively, gave the most accurate mathematical models for the crush length. The error estimates are given in Table 5.3. As it can be seen, large values for R^2 and $R^2_{Prediction}$ and small values for RMSE and PRESS indicate acceptable level of accuracy for the constructed RBF-based surrogate models. The RBF models used for propagation do not need to have very high level of accuracy as they are principally used for a preliminary estimation of response bounds within each joint proposition cell.

Table 5.3 Error estimation of RBF metamodels for crush length

Crush Length	Assessment at test points		Assessment at training points	
	R^2	RMSE	$R^2_{\text{prediction}}$	PRESS
Model 1	0.926	2.04	0.802	174.67
Model 2	0.910	0.745	0.790	61.62

5.1.4 Construction and propagation of joint belief structure

In this case, the constructed joint belief structure contains 69,120 and 45,360 Cartesian products for Models 1 and 2, respectively. It is important to note that in each Cartesian product, the material constants are defined in interval form, and the difference in the number of Cartesian products is due to the difference in the belief structures of the two models.

Propagation of uncertainty requires the determination of the maximum and minimum values (bounds) of the response for each Cartesian product of the constructed joint belief structure, where each uncertain constant can take any value within the corresponding subinterval range. Thus, for Model 1, it would be necessary to solve 69,120 problems once for the minimum and again for the maximum crush length.

Since the GA based solution for each optimization problem takes about an hour on a desktop computer, we chose to develop four separate surrogate models representing the maximum and minimum crush lengths for Models 1 and 2. In each surrogate model, the crush length is related to 10 input variables representing the lower and upper bounds of the five material constants corresponding to a particular Cartesian product.

Using LHS, we selected 50 random samples from the set of 69,120 Cartesian products for Model 1 and another 50 from the 45,360 Cartesian products for Model 2. In each random sample, the material constants appear in interval form that represent the lower and upper bounds of design variables in an optimization problem for finding the minimum and maximum values of crush length. For clarity, we can define the design space for each Cartesian product as $([A1, A2], [B1, B2], [n1, n2], [C1, C2], [m1, m2])_k$, where k = 1, 50.

With the GA toolbox in MATLAB as the optimizer, an initial population of 20 random design points was selected consistently with the specified bounds for each material constant in the kth Cartesian product. This optimization problem was solved once for the minimum crush length and another time for the maximum crush length using a cross-over fraction of 0.8.

With 100 maximum and minimum crush length responses found, the coefficients ($\lambda_i, i = 1, 50$) for each RBF metamodel were calculated. Using the multiple error metrics discussed earlier, the accuracy of each metamodel was verified (see Table 5.4). These metamodels were then used for propagating the interval of uncertainty for each material constant to the interval of uncertainty in the crush length for all 69,120 Cartesian products for Model 1 and 45,360 Cartesian products for Model 2.

For all Cartesian products in Model 1, the overall minimum and maximum crush lengths were found to be 3.4 mm and 39.5 mm, respectively, whereas for Model 2, the overall minimum and maximum values were 2.2 mm and 22.0 mm, respectively.

It should be noted that the BBA of each interval of uncertainty for crush length equals to that of the corresponding Cartesian product of the joint belief structure. Comparing the predicted maximum crush lengths for all Cartesian products (and the minimum crush lengths) revealed very small difference in most of them. Hence, when the difference between the minimum crush lengths and that of the maximum crush lengths in two Cartesian products was less than 1.0 mm, the Cartesian products were treated as one with BBA equal to the sum of BBA of the underlying products. As a result of this size reduction, the belief structure for crush length was reduced significantly from 69,120 to 91 for Model 1 and from 45,360 to 95 for Model 2. Of course, the amount of reduction in belief structure size depends on the tolerance value selected. The reduced propagated

(crush length) belief structure for Models 1 and 2 are given in Table 5.5. Note that for the purpose of belief and plausibility estimation discussed later, unreduced propagated belief structures are used. Although the gap between the lower and upper crush-length bounds in Table 5.5 is rather large, it is important to consider the associated BBA values, which are fairly low for each JC model. Therefore, the available evidence that supports each interval is very weak in this analysis. When the two models are combined, we notice that some intervals take significantly larger BBA values than others, and those with larger BBA values correspond to smaller intervals. For example, if we were to narrow the interval of uncertainty to a single interval with the highest BBA value, then we find the range of crush length to be 9.51 mm to 10.93 mm with BBA of 0.261.

Table 5.4 Error estimation of RBF models for maximization and minimization of the approximate crush length

Metamodel Response	Model 1		Model 2	
	$R^2_{prediction}$	PRESS	$R^2_{prediction}$	PRESS
Maximization	0.940	55.79	0.988	1.93
Minimization	0.966	7.89	0.940	5.74

Table 5.5 The propagated belief structure for Johnson-Cook Models 1 and 2 and their combination

Model 1		Model 2		Combined Model	
Range	BBA	Range	BBA	Range	BBA
[13.99, 15.95]	0.009431	[9.47, 10.93]	0.045388	[13.99,14.74]	0.005583
[13.17, 14.61]	0.007563	[9.03, 13.45]	0.055012	[13.99, 14.54]	0.000202
[10.91, 18.24]	0.033319	[8.85,11.58]	0.054113	[13.99,14.38]	0.000157
[12.59, 15.91]	0.003343	[8.33,13.36]	0.038754	[13.99, 14.01]	7.2E-05
[11.57, 13.81]	0.004432	[8.40, 9.64]	7.93E-05	[13.17,13.45]	0.00784
[9.51, 16.97]	0.028821	[8.12,12.40]	0.011502	[10.91, 10.93]	0.077246
[10.12, 10.79]	0.000946	[8.18,11.01]	0.002686	[9.51, 10.93]	0.261086
[9.00, 15.01]	0.009644	[6.97,11.38]	0.043206	[9.51, 9.64]	0.000947
[9.50, 12.98]	0.000947	[6.30,13.98]	0.013549	[9.03, 13.45]	0.101881
[8.67, 18.69]	0.015109	[10.22,11.42]	0.03591	[9.00,11.58]	0.004288
[13.61, 17.32]	0.002217	[9.24,10.21]	1.46E-05	[9.00, 9.64]	0.001903
[15.23, 17.46]	0.000977	[10.90,11.98]	0.014088	[8.85,11.58]	0.059156
[11.80, 19.87]	0.007205	[10.17,14.74]	0.008382	[8.67, 13.36]	0.041995
[11.55, 12.31]	0.000255	[10.21,12.08]	0.016900	[8.67, 9.64]	0.00775
[11.26, 15.25]	0.000221	[9.24, 14.67]	0.045736	[8.33,13.36]	0.128838
[9.58, 20.16]	0.009467	[8.82, 12.57]	0.004124	[8.40, 9.64]	0.00958

Table 5.5 (Continued)

[12.74, 23.37]	0.004654	[7.67,15.24]	0.035874	[8.12, 12.40]	0.032792
[9.69, 25.76]	0.037882	[8.49, 14.96]	0.019122	[8.18,11.01]	0.003325
[11.32, 22.33]	0.010651	[8.30,17.27]	0.008438	[8.13, 10.29]	4.01E-05
[11.38, 23.66]	0.001552	[7.64,17.23]	0.032285	[9.17, 9.36]	0.000203
[8.87, 24.15]	0.025406	[7.47, 13.05]	0.001535	[7.97, 11.38]	0.020676
[8.67, 21.55]	0.004062	[5.87, 15.44]	0.049601	[7.97,10.57]	5.67E-09
[8.06, 26.15]	0.021253	[6.60, 15.88]	0.005598	[7.32,11.38]	0.101184
[9.17, 9.36]	0.000255	[5.36, 17.62]	0.008526	[7.32,10.57]	4.17E-08
[8.56, 11.56]	0.001004	[8.13, 10.29]	1.05E-05	[8.12, 9.71]	8.08E-06
[7.97, 17.35]	0.011646	[7.83, 11.70]	0.00083	[7.85, 9.71]	7.28E-05
[9.98, 22.12]	0.000137	[9.52, 12.47]	0.011275	[8.12, 8.26]	1.1E-06
[7.32, 22.97]	0.033658	[7.02, 15.11]	0.002832	[7.76, 8.26]	1.22E-05
[10.95, 16.71]	6.24E-05	[5.19, 15.77]	0.015653	[6.97, 6.97]	0.04568
[8.11, 13.01]	0.007017	[7.60, 13.71]	0.011834	[6.71, 11.27]	0.004522
[7.85, 9.71]	0.000158	[7.14,12.19]	0.011662	[6.71,10.57]	6.14E-09
[7.76, 8.26]	2.06E-05	[6.45,12.19]	0.002872	[6.52,12.64]	0.001863
[6.95, 6.97]	2.87E-07	[10.73,12.81]	0.03957	[6.52, 12.19]	0.00106
[6.71, 11.27]	0.004083	[9.53,11.63]	0.0029	[6.52, 11.50]	3.34E-06
[7.12, 14.38]	0.027256	[8.50,15.82]	0.057995	[6.52, 10.57]	3.16E-09
[6.52, 12.64]	0.006478	[6.95,17.52]	0.005954	[6.30, 13.98]	0.004915
[7.31, 20.28]	0.009225	[5.87,16.13]	0.001082	[5.91, 15.44]	0.031229
[7.27, 21.61]	0.001259	[5.83,14.63]	0.00073	[5.91, 14.63]	0.003437
[6.64, 18.31]	0.008533	[6.21, 11.50]	1.52E-05	[6.21, 11.50]	6.11E-06
[5.91, 21.09]	0.055656	[5.15,14.54]	0.020327	[5.91, 10.57]	0.002192
[7.27,15.82]	0.007726	[5.75,10.57]	4.87E-07	[6.45, 8.40]	7.91E-06
[5.91, 22.59]	0.023555	[4.91, 13.72]	0.009404	[5.68, 17.62]	0.002467
[6.45, 8.40]	2.83E-06	[5.48,11.97]	2.98E-06	[5.68, 15.77]	0.001695
[6.46, 9.92]	3.78E-05	[4.07,11.89]	0.000466	[5.68,14.54]	0.000981
[5.68,19.61]	0.003278	[3.23, 14.61]	0.000513	[5.75,10.57]	0.001029
[5.65, 13.95]	0.003419	[6.78, 13.07]	2.73E-08	[5.51,16.49]	0.005855
[5.51, 16.49]	0.005231	[5.45, 12.93]	9.94E-05	[5.51,15.77]	0.001057
[5.95, 25.31]	0.073116	[4.41, 15.72]	0.000354	[5.51,14.54]	0.001357
[5.15, 23.99]	0.032062	[5.53, 18.29]	0.01515	[5.51,13.72]	0.000822
[4.48, 21.51]	0.004432	[4.58, 17.17]	0.01718	[5.51,11.97]	4.93E-05
[5.05, 18.09]	0.000354	[4.57, 18.21]	0.003089	[5.36,17.62]	0.000809
[5.20, 12.02]	4.47E-05	[3.50,15.86]	0.000217	[5.19,15.77]	0.003765
[4.91, 10.40]	1.46E-07	[2.80, 18.18]	0.000208	[5.15,14.54]	0.00197
[5.21, 27.09]	0.01893	[7.82, 14.38]	0.016196	[5.15,13.72]	0.000648
[4.46, 25.75]	0.002268	[9.90, 14.01]	0.002206	[5.15,11.89]	3E-05
[3.81, 23.29]	8.60E-06	[8.20, 16.53]	0.018845	[4.91,13.72]	0.000469
[4.34, 19.63]	0.000209	[7.26, 16.47]	0.011844	[4.48,11.89]	0.001889
[3.09, 24.71]	0.001615	[7.14, 14.40]	1.44E-06	[6.30,10.40]	1.98E-09
[2.26, 17.50]	4.26E-05	[4.74, 12.10]	1.81E-05	[5.87,10.40]	7.53E-09
[5.54, 28.60]	0.005072	[11.56 12.57]	0.001066	[5.36,10.40]	3.62E-09
[4.82, 8.85]	3.81E-09	[10.73,15.64]	0.010895	[5.19,10.40]	5.25E-09
[15.93, 18.79]	0.000221	[10.02,15.58]	0.014977	[4.91,10.40]	8.52E-09
[14.02, 18.77]	0.000142	[8.53, 18.18]	0.012800	[4.07, 11.89]	0.00018
[13.10, 21.28]	0.000123	[7.81, 18.13]	0.014695	[3.81, 14.61]	1.1E-08
[14.18, 26.16]	0.000136	[10.04, 3.17]	0.001037	[3.85,12.56]	6.81E-11
[10.61, 27.72]	0.01803	[8.53, 14.21]	0.002157	[6.30, 8.85]	5.17E-11
[12.75, 26.02]	0.000601	[9.35, 15.56]	0.008113	[5.87, 8.85]	1.97E-10
[8.63, 27.96]	0.056871	[11.45,13.44]	0.001444	[5.36, 8.85]	9.44E-11
[11.36, 25.14]	0.000669	[7.09, 18.41]	0.011847	[5.19, 8.85]	1.37E-10
[7.35, 24.59]	0.000241	[5.62, 13.66]	1.83E-06	[4.91, 8.85]	2.22E-10
[6.93, 29.47]	0.034767	[6.45, 16.84]	0.000182	[2.22, 36.53]	0.013171
[5.71, 31.08]	0.000776	[5.73, 18.98]	0.000448		
[7.23, 27.63]	0.001192	[5.74, 16.82]	0.000546		
[9.34, 29.33]	0.019535	[4.71, 18.88]	0.014123		

Table 5.5 (Continued)

[10.68, 29.12]	0.000297	[3.53, 16.65]	2.21E-05
[9.88, 30.71]	0.001532	[10.76,13.46]	9.68E-05
[8.50, 30.97]	0.008745	[3.85, 12.56]	7.92E-06
[10.12, 38.56]	0.014672	[5.05, 16.44]	5.84E-06
[8.32, 38.38]	0.085286	[4.63, 12.84]	3.43E-06
[8.94, 36.97]	0.001817	[4.23, 14.00]	0.003213
[7.54, 37.07]	0.032268	[7.92, 19.63]	0.029201
[8.30, 32.83]	2.56E-05	[7.31, 21.56]	0.015858
[7.12, 35.73]	0.000322	[7.26, 20.06]	0.006405
[6.90, 32.48]	1.21E-05	[6.57, 19.86]	0.000107
[5.69, 36.60]	0.043014	[6.50, 21.50]	0.001532
[5.51, 35.11]	0.054824	[4.40, 21.11]	0.007828
[4.17, 34.64]	0.030593	[7.97, 20.28]	5.72E-06
[4.05, 32.96]	0.005287	[8.01, 18.84]	0.008258
[3.98, 16.54]	2.50E-06	[4.91, 19.73]	0.001238
[4.38, 36.53]	0.000665	[2.18, 17.35]	0.000131
[4.15, 29.32]	3.12E-05	[5.80, 20.13]	0.000168
		[5.00, 21.97]	0.000139
		[4.12, 21.89]	9.57E-07
		[3.02, 19.13]	0.000129
		[2.22, 21.37]	6.31E-05

5.2 Uncertainty quantification of Johnson-Cook material models

5.2.1 Belief and plausibility estimation for experimental precision intervals

To evaluate the belief and plausibility of the estimated crush length based on JC material model, the propagated intervals of uncertainty with assigned BBA for crush length should be compared to those obtained through experiments. Florance and Goodier (1968) reported an experimental crush length of 13.9 mm for cylindrical tubes with the same material and geometric properties as those used in our crush simulations.

Since the propagated uncertainty is determined in interval form with corresponding BBA, the experimental results should also be defined in interval form for comparison purposes. Here, we define precision intervals for experimental crush length data ranging from 90% to 50% as shown in column 1 of Table 5.6, where 90% implies a bound of ±10% from the 13.9 mm nominal value.

In order to measure epistemic uncertainty of JC material models, we add BBA of those propagated intervals covered by experimental precision interval to find the value of

belief measure and add BBA of those intervals intersecting the experimental precision interval to find the value of plausibility measure.

The estimated belief and plausibility of JC Models 1 and 2 as well as the combined model for different experimental precision intervals are provided in Table 5.6. As indicated, Model 1 offers higher belief for high experimental precision intervals than Model 2. However, for low precision intervals, the reverse is true. Results also indicate that while JC material models are suitable for simulating dynamic material behavior, they include considerable epistemic uncertainty as noted by the large gap between belief and plausibility for each model. Interestingly, the combined model offers higher belief and lower plausibility (i.e., less epistemic uncertainty) for all experimental precision intervals than each individual model. This verifies the fact that multi-model prediction reduces the contribution of model form uncertainty. Table 5.7 provides information on total numbers of propagated uncertainty intervals in belief and plausibility analysis.

Table 5.6 Estimated belief, plausibility and plausibility decision for Johnson-Cook Models 1 and 2 and their combination

Precision Interval	Precision (%)	Model 1			Model 2			Combined Model		
		Bel	Pl	Pl_dec	Bel	Pl	Pl_dec	Bel	Pl	Pl_dec
[12.51,15.29]	90	0.004	0.993	0.177	0.000	0.769	0.205	0.011	0.752	0.244
[11.12,16.68]	80	0.021	0.999	0.339	0.011	0.978	0.468	0.038	0.953	0.522
[9.73,18.07]	70	0.046	1.000	0.482	0.145	1.000	0.746	0.226	1.000	0.814
[8.34,19.46]	60	0.103	1.000	0.604	0.454	1.000	0.906	0.622	1.000	0.950
[6.95,20.85]	50	0.162	1.000	0.703	0.767	1.000	0.969	0.890	1.000	0.988

Table 5.7 Total numbers of propagated uncertainty intervals supporting belief and plausibility for different models

Precision Interval	Precision (%)	Model 1		Model 2		Combined Model	
		Belief	Plausibility	Belief	Plausibility	Belief	Plausibility
[12.51,15.29]	90	698	59299	0	21830	243	5568
[11.12,16.68]	80	9883	64347	1036	41369	1106	6920
[9.73,18.07]	70	20872	67496	9556	45175	2431	7479
[8.34,19.46]	60	32374	68828	24912	45360	4336	7843
[6.95,20.85]	50	41900	69110	38301	45360	6356	7892

5.2.2 Belief and plausibility estimation for observed belief structures

As different forms of JC plasticity model resulted in different material constants, different sources of information (e.g., analytical, numerical and experimental approaches) may offer different values for crush length of the 6061-T6 tube model considered here. Recognizing that each source of information includes an element of uncertainty, it would be impossible to have full confidence in its accuracy. Therefore, construction of an informative belief structure for crush length is necessary before it can be used for uncertainty quantification of JC models or estimation of uncertainty measures (belief and plausibility). Although construction of experimental precision intervals for crush length is useful for estimation of belief and plausibility, it is not sufficiently informative as it relies on only one set of experimental results.

In this section, we consider three sources of information for the crush length, the experimentally measured value obtained by Florance and Goodier in (1968), the analytical value provided by Karagiozovaa and Jones in (2000), and the numerical value found here by using the experimentally validated material constants (see Table 5.8) reported by Johnson et al. (1996) for a model that matches the one labeled as Model 1. All three values are given in Table 5.9, and the simulation-based crush mode using the reported constants in Table 5.8 is shown in Figure 5.3.

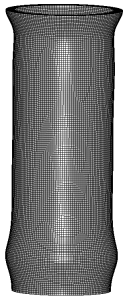

Figure 5.3 Collapsed shape of the 6061-T6 tube with experimentally validated published set of Johnson-Cook material constants

Table 5.8 Johnson-Cook model constants obtained from SHPB tests

Material	T_m(K)	A (MPa)	B (MPa)	C	n	m
AL6061-T6	855	324	114	0.002	0.42	1.34

Table 5.9 Experimental, analytical and numerical values for crush length of 6061-T6 tube

Crush Length (mm)	Experimental	Analytical	Numerical
	13.9	13.1	12.03

Here, the methodology developed in chapter 2 is used for construction of the crush length belief structure, where identification of the relationship types (conflict, agreement and ignorance) between intervals of uncertainty for crush length is the key for constructing a belief structure for it. However, the body of evidence (see Table 5.9) for crush length contains too small a dataset to reveal differences in distribution of data points within intervals of uncertainty. In fact, identification of relationship types between disjointed intervals of uncertainty for crush length involves epistemic uncertainty due to lack of data.

Figure 5.4 shows three possible belief structures for the crush length, where symbols N, A and E denote numerical, analytical and experimental data points, respectively. Belief structure 1 considers conflict relationship among the three intervals of uncertainty corresponding to experimental, numerical and analytical data points. In belief structure 2, experimental and analytical intervals of uncertainty are in conflict relationship with each other and in ignorance relationship with the numerical interval of uncertainty. This is because intervals of analytical and experimental data points are close to each other but separated at a distance with the numerical interval. Instead of considering 4 disjointed uncertainty intervals, two intervals are considered for belief structure 3, where one interval includes the combined analytical and experimental data

points whereas the other spans the universal set. Hence, interval of numerical data is considered to be in ignorance relationship with its adjacent interval as it includes fewer data points than the rest.

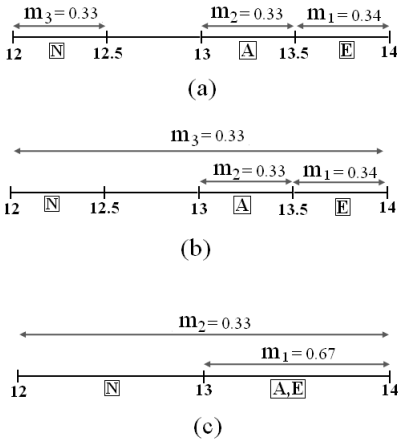

Figure 5.4 Alternate belief structure (a) 1, (b) 2 and (c) 3 for crush length based on numerical, analytical, and experimental results

For estimation of belief and plausibility measures, a consolidated belief structure for crush length is needed that includes all the available evidence as captured in Figure 5.4. To achieve this detailed belief structure, Yager's combination rule is used. Table 5.10 shows the three individual belief structures along with the combined belief structure for crush length.

Table 5.10 Intervals and associated BBA values for crush length belief structures 1 through 3 and their combination.

Interval #	Belief structure 1		Belief structure 2		Belief structure 3	
	Range	BBA	Range	BBA	Range	BBA
1	[13.5, 14.0]	0.3400	[13.5, 14.0]	0.3400	[13.0, 14.0]	0.6700
2	[13.0, 13.5]	0.3300	[13.0, 13.5]	0.3300	[12.0,14.0]	0.3300
3	[12.0,12.5]	0.3300	[12.0,14.0]	0.3300		
Combined (final) belief Structure						
1, 3, 5	[13.5, 14.0]	0.2278	[12.0, 12.5]	0.0359	[12.0, 14.0]	0.22
2, 4	[13.0, 13.5]	0.2178	[13.0, 14.0]	0.2985	-	-

Assuming A_i represents the ith focal element of belief structure M with BBA of m_i, the belief and plausibility of M can be estimated as

$$Bel(M) = \sum_{i=1}^{i=n} m_i \sum_{c_k \subseteq A_i} m(c_k) \tag{5.8}$$

$$Pl(M) = \sum_{i=1}^{i=n} m_i \sum_{c_k \cap A_i \neq \Phi} m(c_k) \tag{5.9}$$

where n is the number of focal elements of M, c_k is the kth focal element of the propagated belief structure C with BBA of $m(c_k)$. The range of k can be up to 69,120 for Model 1, 45,360 for Model 2, and 7,957 for the combined case. For the crush tube problem, n takes the value of 3, 3, and 2 for crush length belief structures 1, 2, and 3, respectively, whereas for the combined belief structure, n is 5 (see Table 5.10). The inner summations in Eqs. (5.8) and (5.9) represent the belief and plausibility of each element of the crush length belief structure, respectively. The estimated belief and plausibility of belief structures for crush length in Table 5.10 are given in Table 5.11. Note that the estimation of belief and plausibility of the combined belief structure for crush length is more suitable for quantification of epistemic uncertainty embedded in JC material models. Comparison between Tables 5.6 and 5.11 indicates that the uncertainty measures of the consolidated BBA are closer to the 90% experimental precision interval than the rest.

Table 5.11 Estimated belief, plausibility and plausibility decision of all possible belief structures along with the combined belief structure for crush length of 6061-T6 tube.

Model Type	Belief structure 1			Belief structure 2		
	Bel	Pl	Pl_dec	Bel	Pl	Pl_dec
Model 1	0.000	0.980	0.033	0.000	0.982	0.065
Model 2	0.000	0.715	0.049	0.000	0.715	0.094
Combined	0.001	0.693	0.054	0.001	0.700	0.106
Model Type	Belief structure 3			Combined Belief		
	Bel	Pl	Pl_dec	Bel	Pl	Pl_dec
Model 1	0.000	0.986	0.087	0.000	0.982	0.018
Model 2	0.000	0.729	0.121	0.000	0.710	0.089
Combined	0.009	0.736	0.138	0.001	0.703	0.102

5.2.3 Plausibility decision function (Pl_dec) estimation

Tables 5.6 and 5.11 show that a large gap exists between the belief and plausibility of experimental precision intervals or belief structures for crush length. This gap, which is indicative of the amount of epistemic uncertainty embedded in JC material models, makes it difficult to evaluate simulation accuracy of JC material models with only belief and plausibility measures.

Using the generalized insufficient reason principle, Savage (1972) Bae et al. (2006) introduced plausibility decision function (*Pl_dec*) as a supplemental measure to make decision for model evaluation under epistemic uncertainty when the resulting bound between belief and plausibility is too large. *Pl_dec* of the belief structure *M* can be determined by the following equation:

$$Pl\_dec(M) = \sum_{i=1}^{i=n} m_i \sum_{c_k \subseteq A_i} m(c_k) + \sum_{i=1}^{i=n} m_i \sum_{c_k \cap A_i \neq \Phi} m(c_k) \frac{|A_i \cap c_k|}{|c_k|} \quad (5.10)$$

Using Eq. (5.10), *Pl_dec* is calculated for precision intervals and belief structures of crush length with results shown in Tables 5.6 and 5.11. Note that the experimental precision intervals in Table 5.6 can be considered as a belief structure with only one focal element.

As can be seen in Tables 5.6 and 5.11, estimated *Pl_dec* values are considerably closer to belief than plausibility. This implies that the propagated information favors complement of belief function. Hence, in this case, further precaution should be taken for assessing reliability of simulation responses due to the existing uncertainties.

5.3 Uncertainty propagation and measurement of BCJ plasticity model

A nonlinear FEA of Taylor impact test of a 7075-T651 aluminum alloy solid circular cylinder is used for propagation of the represented uncertainty in Table 4.11. The

final deformed length and radius of the cylinder are used as the two main measures of plastic deformation in this case (see Figure 5.5).

As in the case of JC plasticity, we rely on design and analysis of computer experiments for uncertainty propagation by using the following steps:

1. LHS technique is adopted to generate 60 separate samples (training points) for material constants C_1 to C_6 of BCJ plasticity model. The universal set that spans over the constructed belief structures for all six uncertain material constants of BCJ flow equation as shown in Table 4.11 are considered in selecting the bounds for generation of the random samples (uncertain material constants).

2. For each training point, we performed FE simulation of Taylor impact test on the solid cylinder with a 30-mm length and 4.85-mm radius colliding with a velocity of 267 m/s into a rigid plate using an explicit nonlinear FE code LS-DYNA, v 971. The deformed shape of one sample after Taylor impact simulation is shown in figure 5.5 by considering a quarter model of the solid cylinder. The derived hardening constants of BCJ plasticity model (constants C_7 to C_{18}) in Table 5.10 are used in all FE simulations while flow constants (C_1 to C_6) are determined by the generated training points.

3. With 60 training points and their responses identified in steps 1 and 2, accurate surrogate models based on RBF are developed to establish an explicit relationship between material constants of BCJ flow equation and the final deformed radius and length. Since RBF is an interpolation model, ten randomly selected design points (different from any of the training points) within the global bounds of the material constants of BCJ flow equation are used as test points for the evaluation of error statistics to ensure sufficient accuracy of the constructed RBF-based surrogate models.

4. Finally, with each joint proposition providing the bounds or side constraints for material constants of flow equation for BCJ plasticity model, a global optimization (i.e., Genetic Algorithm) technique is applied to the constructed RBF metamodels to find the minimum and maximum values of structural response (radius and length of the deformed cylinder). This procedure is repeated for all the joint propositions of material constants to find the corresponding belief structure for deformed radius and length of cylinder. Hence, the propagated belief structure for structural response is obtained.

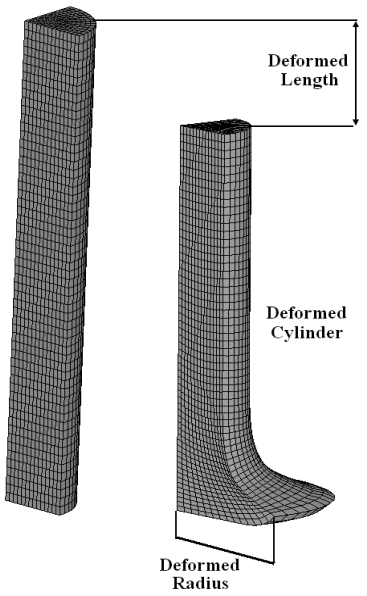

Figure 5.5 Taylor impact simulation model showing the original and the deformed geometries.

Uncertainty quantification requires assessment of uncertainty measures (belief, plausibility) for a defined target proposition set using the obtained propagated belief structure. Konokman et al. (2011) reported an experimental deformed length of 26.40 mm and radius of 5.76 mm for the cylinder with the same material and geometric properties as those used here for Taylor impact simulations. Here, we define 90% and

95% precision intervals for experimental deformed length and radius the cylinder and consider them as target proposition set for estimation of uncertainty measures.

To quantify the uncertainty of the BCJ plasticity model, we add BBA of those propagated intervals covered by experimental precision intervals to find belief and add BBA of those intervals intersecting the experimental precision interval to determine plausibility, respectively. The estimated belief and plausibility for 90% and 95% experimental precision intervals for both deformed radius and length are provided in Table 5.12. As indicated, the estimated values of belief and plausibility for experimental precision intervals of deformed length are slightly higher than those of the deformed radius. Also as expected, for both deformed length and radius, the estimated values of uncertainty measures of 90% precision intervals are higher than those of 95% precision intervals. The gap between belief and plausibility for experimental precision intervals is indicative of epistemic uncertainty embedded in the BCJ plasticity model. The high estimated values of plausibility for precision intervals (target proposition sets) indicate that the presented approach is valid for determination of the BCJ material constants. It also verifies the accuracy of the model to simulate a large deformation process.

Table 5.12 Estimated belief and plausibility for experimental precision intervals of deformed length and radius

Precision (%)	Deformed Length (mm)		Deformed Radius (mm)	
	Bel	Pl	Bel	Pl
90	0.004	0.928	0.001	0.897
95	0.002	0.899	0.001	0.891

CHAPTER VI

AGGREGATION RULE OF EVIDENCE FOR UNCERTAINTY MODELING AND DECISION MAKING

When faced with information or data from multiple sources of evidence, it is possible to encounter diverse belief structures. Since uncertainty can be represented and quantified only by a single belief structure that should reflect the diversity of information and expert opinions, it is necessary to aggregate the body of evidence. However, there is no unified approach for evidence aggregation, but a number of aggregation rules have been reported in the literature (Sents et al., 2002; Yager, 1987, 1987a; Inagaki, 1991). Despite the diversity in their formulation, all cited aggregation rules offer a unique belief structure when there is no conflict or ignorance between different information sources. However, in presence of high degree of conflict or ignorance, the combined belief structure can be quite diverse.

In the area of uncertainty modeling of large deformation process, the issue of combining evidence from different sources can appear in both uncertainty representation and quantification stages. As for uncertainty representation, different sources of experimental data, the approach they follow to provide stress-strain data at high temperature and strain rates, and the method used for fitting the material constants provide wide variation in one or more material parameters (Gray et al., 1994). In the case of uncertainty propagation and quantification, the choice of available plasticity models (Johnson and Cook, 1985, 1983; Bammann et al., 1993, Brown et al. 2006; Hallquist,

1993; Shirakashi, 1983) is quite diverse in the way a particular physical effect such as temperature or strain rate is mathematically modeled, and this diversity results in different propagated belief structures.

This topic falls under the area of model-selection uncertainty, and many researchers have relied on the Bayesian approach to address it in the recent years. For example, Edwards (1984) and Guedes Soares (1997) used this approach to combine several competing probability distribution types to describe a random variable, whereas Zhang and Mahadevan (2000) used the Bayesian approach to combine multiple competing limit-state formulations simultaneously for the same problem. Park and Grandhi (2010) developed a Bayesian framework to quantify model probability using measured deviations between experimental data and that of model predictions. However, Bayesian framework can model both parametric and model-selection uncertainties when uncertain variables are defined by probability distribution functions (Droguett and Mosleh, 2008). Commonly, a uniform distribution is assumed for prior probabilities of different models and posterior model probabilities are calculated based on experimental observations. For each new observation, the estimated posterior model probabilities are treated as prior and updated for estimation of the next posterior probabilities.

In this chapter, a new aggregation rule of evidence is developed for more accurate uncertainty modeling of large deformation processes. In the previous chapters, Yager's (1987, 1987a) aggregation rule of evidence along with a general uncertainty representation, propagation and quantification framework were employed to address this issue. However, it is recognized that the application of Yager's rule that allocates belief function of conflict to the universal set (complete ignorance) results in a huge gap between the estimated belief and plausibility (epistemic uncertainty) that hampers

decision-making in product design. To reconcile this challenge, the proposed evidence aggregation rule makes use of GPA suggested by Yager (1987, 1987a) along with a newly defined Credibility Factor of Evidence (CFE). Observed experimental evidence on simulation responses as well as uncertain parameters are considered for calculation of the CFE used for combination of different belief structures.

6.1 The proposed aggregation rule of evidence

Inagaki (1991) introduced a more advanced combination rule of evidence that takes advantage of the GPA function (q) that Yager defined in (Yager, 1987a) to define a continuous parameterized class of combination operations which subsumes both Dempster's rule and Yager's rule. Like Inagaki rule, the proposed combination rule makes use of GPA and is expressed as

$$q(A) = \sum_{B\cap C=A} m_1(B)m_2(C), \quad m^S(A) = q(A) \tag{6.1}$$

$$Q(B) = \sum_{B\cap C=\emptyset} N\, m_1(B)m_2(C), \quad m^S(B) = Q(B) \tag{6.2}$$

$$m^s(\emptyset) = 0 \tag{6.3}$$

Equation (6.1) determines the aggregated BBA when information sources are not in conflict while Equation (6.2) indicates the functionality of the presented aggregation rule in case the information sources are in conflict (disjoint subset B and C in Eq. (6.2)). The parameter N in Eq. (6.2) is the CFE and is determined based on the comparative closeness level of two disjoint subsets B and C from different information sources to a reference point (RF). The CFE value can be obtained as

$$CFE = \frac{|\mu(C)-RF|}{|\mu(B)-RF|+|\mu(C)-RF|} \tag{6.4}$$

where $\mu(B)$ and $\mu(C)$ are the mean values of disjoint subsets B and C, respectively. Note that the RF refers to the observed value of an uncertain parameter in uncertainty

representation level or availible experimental value of structural response in uncertainty propagation and measurement levels.

Conceptually, the proposed aggregation rule of evidence divides the BBA of conflict between disjoint subsets of different information sources proportionate to their level of assessed credibility using the observed evidence. When there is no evidence, decision making on most expected values of uncertain variables or simulation response is necessary to determine RF. However, this condition has not been investigated in this research. Without using the CFE, the proposed aggregation rule reduces to the Yager formulation and increases the amount of epistemic uncertainty.

6.2 Uncertainty modeling of large deformation process

The evidential uncertainty quantification framework outlined by Figure 1.1 is adopted in this section. To examine the characteristics of the proposed aggregation rule, JC and ZA plasticity models are considered using two different fitting approaches as presented in (Johnson and Cook, 1983, 1985). The represented uncertainties in each model are propagated through Taylor impact simulation of AISI 4340 Steel resulting in two propagated belief structures. The proposed rule is adopted to generate a consolidated propagated belief structure for modeling model selection uncertainty. Finally, through comparison of this consolidated belief structure with an experiment-based precision interval, epistemic uncertainty is quantified. Results indicate that application of the proposed aggregation rule leads to significant reduction of epistemic uncertainty. Also, a methodology for decision-making on simulation response using the propagated belief structure is explained.

6.2.1 Uncertainty representation of material constants

The experimental data in Table 6.1 offers multiple combinations of stress-strain curves corresponding to different strain rate and temperature ranges. Once again, two fitting methods (Johnson and Cook, 1983, 1985) are employed for determination of JC material constants. Note that fitting method 1 determines all constants simultaneously while fitting method 2 determine them in separate stages. Hence, these choices will result in a wide range of values for each model constant, and capture the sources of uncertainty that will affect both the model constants as well as the simulation results.

Relying on dislocation mechanics, ZA provides a physics-based relationship to describe dynamic material behavior. It offers different formulations for face centered cubic (FCC) and body centered cubic (BCC) materials expressed as

$$\sigma = C_0 + C_2\epsilon^n[EXP(-C_3T + C_4Tln\dot{\varepsilon}^*)] \quad \text{(FCC)} \quad (6.5)$$

$$\sigma = C_0 + C_1[EXP(-C_3T + C_4Tln\dot{\varepsilon}^*)] + C_5\varepsilon^n \quad \text{(BCC)} \quad (6.6)$$

where C_0, C_1, C_3, C_4, C_5 and n are material constants, and $\dot{\varepsilon}^* = \dot{\varepsilon}/\dot{\varepsilon}_o$ is the dimensionless plastic strain rate with $\dot{\varepsilon}_o = 1.0\ s^{-1}$.

Table 6.1 Testing conditions for the experimental source of data

Curve	Type	Strain Rate (s^{-1})	Temperature (K)
1	Tension	0.0004	293
2	Tension	0.009	293
3	Tension	32	293
4	Tension	117	293
5	Tension	604	494
6	Tension	1500	473
7	Tension	2500	298
8	Tension	650	733
9	Tension	2000	873
10	Tension	1500	673

Table 6.2 lists the possible sets of material constants of ZA plasticity model for AISI 4340 Steel derived through the fitting of the model with different sets of stress-strain curves selected from Table 6.1 over the specified ranges of temperatures and strain rates. Note that the fitting method 1 is employed for all listed ZA constants in Table 6.1. As for JC plasticity model, fitting methods 1 and 2 offer 19 and 18 sets of material constants, respectively, and are provided by Table 8.3.

Table 6.2 ZA material constants for AISI 4340 steel obtained using fitting method 1

C_0(MPa)	C_1(MPa)	C_3(1/K)	C_4(1/K)	C_5(MPa)	n
166.56	1882.21	0.09831	0.00363	1288.53	0.209
197.13	505.53	0.07472	0.00588	1327.27	0.212
155.79	3447.38	0.68111	0.10274	839.40	0.052
104.57	873.57	0.41847	0.08235	1402.26	0.180
126.08	2531.80	0.72343	0.15704	930.25	0.074
104.25	4974.52	0.72342	0.04600	1441.82	0.202
97.24	2117.02	0.45640	0.05325	1961.48	0.244
256.62	3581.58	0.79078	0.10171	668.64	0.104
326.83	1789.24	0.324089	0.04125	1342.44	0.397
110.93	803.03	0.39522	0.05033	1330.30	0.132
440.71	1850.45	0.40983	0.02709	1920.87	0.463

Here, the obtained data on material constants of JC plasticity model using the fitting methods 1 and 2 and ZA model using fitting method 1 is used to construct separate belief structures for each of their material constants. Then, the presented aggregation rule of evidence is used to combine different belief structures suggested by fitting method 1 and 2 for final representation of uncertainty in material constants. Combination results are compared with Yager aggregation rule of evidence.

Following the procedure discussed in Chapter 4, a separate belief structure for each uncertain material constant of ZA plasticity model for AISI 4340 Steel is constructed and is given by Table 6.3. As an example, the dataset used to construct a belief structure for constant C5 along with the corresponding belief structure are shown

in Figure 6.1. Fitting method 1 and 2 suggest two different belief structures for material constants of JC plasticity model and are given in Table 8.4.

Table 6.3 Belief structures of material constants of ZA plasticity model for AISI 4340 Steel

Interval No.	C0		C1		C3	
	Range	BBA	Range	BBA	Range	BBA
1	[97.24, 211.73]	8/13	[505.5, 1995.2]	6/13	[0.0747, 0.3599]	3/13
2	[97.24, 326.22]	4/13	[1995.2, 3484]	4/13	[0.3599, 0.6451]	4/13
3	[326.22,440.71]	1/13	[3484, 4974.5]	3/13	[0.6451, 0.9303]	6/13
	C4		C5		n	
1	[0.0036, 0.06305]	7/13	[617.1, 1065.2]	4/13	[0.0522, 0.1893]	6/13
2	[0.0036, 0.18188]	6/13	[1065.2, 1513]	7/13	[0.1893, 0.3263]	4/13
			[1065.2, 1961]	2/13	[0.3263,0.4634]	3/13

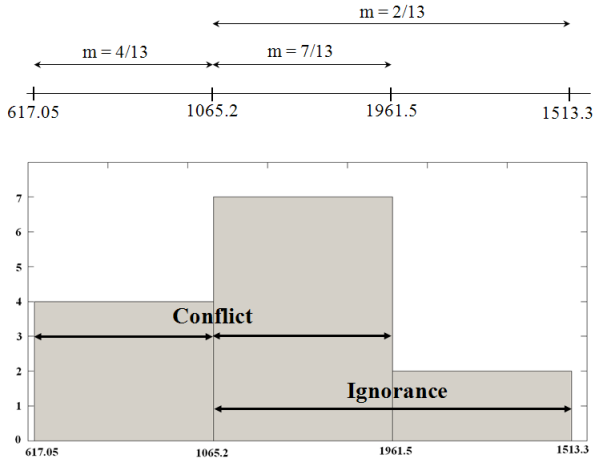

Figure 6.1 Data distribution and the corresponding belief structure for constant C_5

The constructed belief structure of ZA plasticity model material constants as given by Table 6.3 shows final representation of uncertainty, and can be used for uncertainty propagation. However, as for JC plasticity model, the different belief structures of material constants suggested by fitting methods 1 and 2 (see Table 8.4) should be combined into a single belief structure using a proper aggregation rule of evidence.

The combined belief structure of JC material constants using Yager's and the proposed aggregation rule of evidence is given by Table 6.4. As mentioned earlier, in case two intervals of uncertainty from different information sources are disjoint (in conflict), Yager's rule allocates the associated conflicting BBA to the universal set as ignorance or lack of knowledge. Here, the amounts of conflicting BBA between belief structures of constants A, B and n offered by fitting methods 1 and 2 are found to be 0.6316, 0.5789 and 0.5965, respectively, and are assigned to the universal set based on Yager's aggregation rule (see interval No. 3 in Table 6.4). Such high amount of conflict between fitting methods 1 and 2 for constants A, B and n of JC plasticity model gives rise to epistemic uncertainty.

To better deal with conflict and reduce epistemic uncertainty, the proposed aggregation rule of evidence is employed and the combination results are provided in Table 6.4. Note that the material constants of JC plasticity given by Table 6.5 for AISI 4340 Steel (Meyers 1994) are considered as RF for determination of the CFE in the proposed aggregation rule.

As indicated, The BBA of conflict assigned to the universal set (interval No. 3) in Yager's rule is distributed amongst intervals 1 to 4 for constant A, 2 to 5 for constant B and 3 to 6 for constant n in the proposed aggregation rule of evidence (see Table 6.4). In fact, the combined belief structure by the proposed aggregation rule is more informative than that by Yager's rule and includes shorter intervals.

In the context of evidence theory, long intervals (subset) that span over other intervals (other subsets) in a belief structure contribute to ignorance, and the combined belief structure of Yager's rule includes more ignorance than that of the proposed aggregation rule.

It is worth noting that there is no degree of conflict between belief structures of fitting method 1 and 2 for constant *C* and *m*, and the proposed aggregation rule of evidence and the Yager's rule yield the same combined belief structures, hence, the belief structures for C and m are shown only once in Table 6.4. Here, the combined belief structure of JC material constants using the proposed aggregation rule (see Table 6.4) is considered for final representation of uncertainty. As for ZA plasticity model, belief structures of material constants given by Table 6.3 are considered.

Table 6.4 Combined belief structures of material constants of JC plasticity model for AISI 4340 Steel

Combination Using *Yager* Aggregation Rule					
A(MPa)		B(MPa)		n	
Range	BBA	Range	BBA	Range	BBA
[705.0, 724.8]	0.1228	[137.96, 212.95]	0.2807	[0.1218, 0.1547]	0.1404
[764.4, 804.0]	0.2456	[309.35, 405.75]	0.1404	[0.2383, 0.2833]	0.2632
[329.9, 1424.3]	**0.6316**	**[116.54, 532.83]**	**0.5789**	**[0.0710, 0.3220]**	**0.5965**
C		m			
[0.0569, 0.0638]	0.2222	[0.4299, 0.9231]	0.6111		
[0.0637, 0.0881]	0.6959	[0.4299, 1.0354]	0.2456		
[0.0637, 0.1634]	0.0702	[0.4299, 1.4160]	0.0819		
[0.0637, 0.2131]	0.0117	[0.4299, 2.8951]	0.0614		
Combination Using the *Presented* Aggregation Rule					
A(MPa)		B(MPa)		n	
Range	BBA	Range	BBA	Range	BBA
[705.0, 724.8]	0.2877	[137.96, 212.95]	0.2807	[0.1218, 0.1547]	0.1404
[764.4, 804.0]	0.6550	[309.35, 405.75]	0.4277	[0.2383, 0.2833]	0.2632
[877.1, 1150.7]	0.0457	[137.96, 295.91]	0.1441	[0.1218, 0.1756]	0.0108
[1150.7, 1424.3]	0.0116	[453.85, 532.83]	0.1451	[0.2383, 0.3220]	0.0594
		[116.54, 212.95]	0.0024	[0.1756, 0.2833]	0.4358
				[0.0710, 0.1547]	0.0905

Table 6.5 The most commonly used values of Johnson-Cook material constants for AISI 4340

A (MPa)	*B* (MPa)	*n*	*C*	*m*
792	510	0.26	0.014	1.03

6.2.2 Uncertainty propagation and measurement

The represented uncertainty of ZA and JC plasticity models are propagated through Taylor impact simulation of an AISI 4340 Steel cylinder. Again, design and analysis of computer experiments is heavily employed to reduce the computational cost of uncertainty propagation. Multi-model analysis is also performed using Yager and the proposed aggregation rule of evidence and results of uncertainty measurement are compared and discussed. The steps for uncertainty propagation as outlined by Figure 1.1 are as follows:

1. LHS technique is adopted to generate 60 and 50 separate samples (training points) for material constants of ZA and JC plasticity models, respectively. The universal set that spans over the constructed belief structures for all six uncertain material constants of ZA (see Table 6.3) and five material constants of JC plasticity models (see Table 6.4) are considered in selecting the bounds for generation of the random samples (uncertain material constants).

2. For each training point, an FE simulation of Taylor impact test is performed on a solid circular cylinder with a 37.97 mm length and 7.595 mm diameter colliding with a velocity of 270 m/s into a rigid plate using an explicit nonlinear FE code LS-DYNA, v 971.

3. With training points and their responses identified in steps 1 and 2, accurate surrogate models based on RBF are developed to establish an explicit relationship between material constants of both JC and ZA plasticity models with the final deformed length and expanded diameter of the impacted cylinder. Since RBF is an interpolation model, ten randomly selected design points (different from any of the training points) within the global bounds of the material constants of both JC and ZA are used as test

points for the evaluation of error statistics to ensure sufficient accuracy of the constructed RBF-based surrogate models.

4. Finally, with each joint proposition providing the bounds or side constraints for material constants of ZA and JC plasticity models, a global optimization (i.e., Genetic Algorithm) technique is applied to the constructed RBF metamodels to find the minimum and maximum values of structural response (expanded diameter and deformed length of the impacted cylinder). This procedure is repeated for all the joint propositions of material constants to find the corresponding belief structure for expanded diameter and deformed length of cylinder. Hence, different propagated belief structure of structural response for JC and ZA plasticity models is obtained.

6.2.3 Uncertainty measurement results and Multi-model analysis

In (Konokman et al. 2011), an experimental deformed length of 31.3 mm and expanded diameter of 12.1 mm is reported for the cylinder with the same material and geometric properties as those used here for Taylor impact simulations. Here, we define 90% and 95% precision intervals for experimental deformed length and expanded diameter of the cylinder and consider them as target proposition set for estimation of uncertainty measures. For example, precision interval (PI) for the 90% range implies an interval or target proposition (TP) that extends ±10% away from the observed experimental value.

To quantify the uncertainty of the ZA or JC plasticity models, we add BBA of those propagated intervals covered by experimental precision intervals to find belief and add BBA of those intervals intersecting the experimental precision interval to determine plausibility according. The estimated uncertainty measures for 90% and 95%

experimental precision intervals for both expanded diameter and deformed length using the propagated belief structure of both ZA and JC plasticity models are provided in Table 6.6. As indicated, the estimated values of belief and plausibility for experimental precision intervals of deformed length are slightly higher than those of the expanded diameter. Also as expected, for both deformed length and diameter, the estimated values of uncertainty measures of 90% precision intervals are higher than those of 95% precision intervals. The estimated plausibility for ZA plasticity model is slightly higher than that for JC plasticity model. The gap between belief and plausibility for experimental precision intervals is indicative of epistemic uncertainty embedded in the JC and ZA plasticity models. As it can be realized, the estimated values of plausibility decision are low for both plasticity models.

For the purpose of multi-model analysis, the propagated belief structures of JC and ZA plasticity models are combined into a single belief structure using both Yager and the proposed aggregation rules of evidence. Note that the reported experimental values of deformed length and expanded diameter in (Konokman et al. 2011) are considered as RF for estimation of CFE using the proposed aggregation rule. Uncertainty measures of combined propagated belief structures are estimated and are given in Table 6.6. As it can be seen, combined belief structures include a shorter gap between belief and plausibility as opposed to single belief structures of ZA and JC plasticity models which indicates reduction of epistemic uncertainty in simulation of large deformation processes through multi-model analysis. Also, the gap between belief and plausibility for the combined belief structure by the proposed aggregation rule is shorter than that by the Yager's rule. This is because the proposed aggregation rule used observed experimental evidence to deal with conflict between ZA and JC plasticity models and Yager's rule simply assigns

the conflicting BBA to universal set without acquisition of knowledge and information. Also, estimated value of plausibility decision for the proposed aggregation rule is higher than that by Yager's rule.

Table 6.6 Estimated uncertainty measures for experimental precision intervals of deformed length and expanded diameter

Zerilli-Armstrong (ZA) plasticity model						
Precision (%)	Deformed Length (mm)			Expanded diameter (mm)		
	Bel	*Pl*	*Pl_dec*	*Bel*	*Pl*	*Pl_dec*
95	0.002	0.9656	0.019	0.001	0.9458	0.004
90	0.003	0.9824	0.025	0.001	0.9723	0.007
Johnson-Cook (JC) plasticity model						
95	0.001	0.9652	0.014	0.001	0.9369	0.003
90	0.001	0.9789	0.023	0.001	0.9488	0.006
Combined JC and ZA models using Yager's Rule						
95	0.007	0.7684	0.062	0.003	0.7322	0.023
90	0.009	0.8927	0.095	0.005	0.7969	0.048
Combined JC and ZA models using the Proposed Aggregation Rule						
95	0.018	0.7312	0.290	0.008	0.710	0.194
90	0.070	0.8150	0.383	0.011	0.757	0.228

CHAPTER VII

COMPUTATIONAL FRAMEWORK FOR EVIDENCE-BASED OPTIMIZATION OF STRUCTURES

A computational framework for EBDO of structures is developed and combined with advanced modeling of materials and associated uncertainties. The framework uses evidence theory to quantify epistemic uncertainties embedded in dynamic material behavior that can be reflected by constants of plasticity models. Due to the computational cost of nonlinear simulations combined with advanced plasticity modeling, the framework relies on metamodeling of key responses.

The proposed computational framework for EBDO of structures under material model uncertainty includes a deterministic objective function as well as one or more non-deterministic (evidence-based) constraints that are affected by various sources of material uncertainties. The framework for representation, propagation and quantification of uncertainties in plasticity models outlined in Figure 7.1 is employed for evaluation of the evidence-based optimization constraint(s). Therefore, several computational codes written for representation, propagation and quantification of uncertainties along with computational codes written for optimization of structures interact heavily in the proposed EBDO framework.

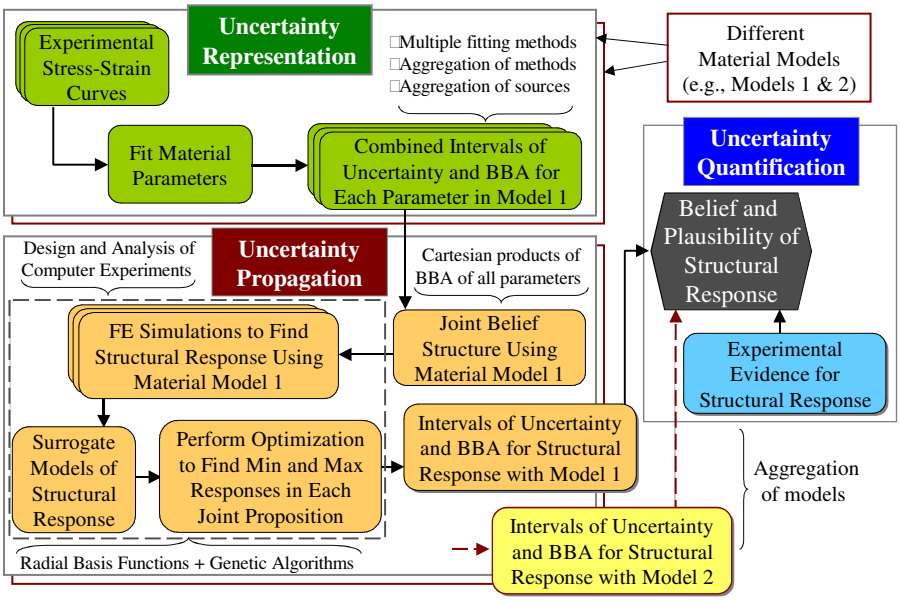

Figure 7.1 Representation, propagation, and quantification of uncertainty in material models

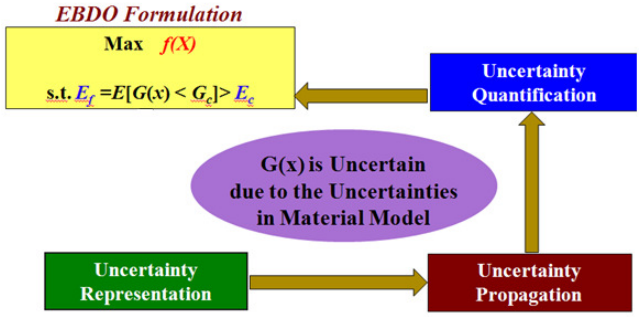

Figure 7.2 Interaction between computational codes for uncertainty modeling and that of optimization in the proposed EBDO framework

Figures 7.1 and 7.2 indicate that a considerable flow of information and data transfer exists among several computational codes in the proposed framework for optimization of structures under material form uncertainty.

7.1 Computational framework for evidence-based design optimization of structures

The proposed evidential framework for optimization of structures under material uncertainties seeks an optimal geometric design for the most favorite structural response of the product under material uncertainties. The framework makes a distinction between design variables in vector $\boldsymbol{X} = [X_1, X_2, \dots, X_n]$ and uncertain variables in vector $\boldsymbol{D} = [d_1, d_2, \dots, d_n]$, and includes two separate mathematical formulation of deterministic objective function and non-deterministic constraint, respectively. Hence, the general EBDO formulation takes the form

$$\begin{aligned} &Maximize && f(X) \\ &s.t && E_f = E[G(X) \leq 0] \leq E_C \\ & && X^L \leq X \leq X^U \end{aligned} \tag{7.1}$$

where E_f, E and E_c are plausibility or plausibility decision of a desired space, one uncertainty measure of plausibility or plausibility decision, and evidence indicator, respectively. The procedures used to construct the objective function and the evidence-based constraints are presented in the following sections.

7.1.1 Objective function

To reduce the computational costs associated with non-linear FE simulations of large deformation process, the framework relies heavily on design and analysis of computer experiments. With generation of random samples within the design space $\boldsymbol{X}$ and performing FE simulations to obtain the corresponding responses, it is possible to construct metamodels that relate the objective function to design variables. Since in the proposed EBDO framework, material uncertainties are not incorporated in the calculation of objective function, an experimentally verified set of JC material constants (Johnson et al., 1996) is used in FE simulation of all generated random samples. Also, it is possible to consider the mean of the constructed belief structure for material constants in FE

simulation of all generated random samples. Hence, computational codes for design and analysis of computer experiments, non-linear FE simulations, and metamodeling are used for construction of the objective function.

7.1.2 Evidence-based constraint function

For evaluation of the evidence-based constraint E_f in Eq. (7.1), material uncertainty should be incorporated. In fact, evaluation of the constraint function for each of the randomly generated samples requires a large number of simulations for determination of the associated propagated belief structure following the uncertainty modeling procedure presented in chapter 4. To reduce the computational complexity, the evidence-based constraint is evaluated for those samples that show completely different structural behavior. Finally, with determination of the constraint for the selected random samples, it is possible to construct metamodels that relate the design variables $\boldsymbol{X}$ to the constraint E_f. After construction of the evidence-based constraint function, Eq. (7.1) can be solved based on the desired system safety using an optimization method. As it can be realized, computational codes for optimization solution and uncertainty modeling interact with each other in the proposed EBDO framework. From the computational standpoint, a brief description of uncertainty modeling procedure and the associated written codes along with their interactions is explained in the following sections.

7.1.2.1 Uncertainty representation

As depicted by Figure 7.3, uncertainty representation of material constants requires 1) data transfer among different computational codes for fitting constants of plasticity models with various combinations of stress-strain curves at different strain rates and temperatures; 2) constructing histograms of collected evidence; 3) identifications of

relationship types between uncertainty intervals as explained in chapter 2; 4) construction of belief structures; and 5) combination of belief structures provided by different experimental sources and different expert opinion for fitting the constants using one of the Dempster, Yager or the suggested combination rule in chapter 6.

As shown by Figure 7.3 briefly, first, all possible constants of plasticity model are obtained through feeding different combination of stress-strain curves at different temperature and strain rates for each experimental source into each fitting code. Secondly, the obtained values of material constants for each experimental source and fitting approach are fed into computational codes that are able to construct their histograms and reduce the number of disjoint intervals in a way that distinction between distributions of data within intervals is identified. Third, such reduced histograms are fed into codes that are able to identify relationship type between disjoint intervals and construct a belief structure following the methodology explained in chapter 2. Finally, constructed belief structures of each material constant are fed into evidence combination codes that follow one of the discussed aggregation rules of evidence for generation of a consolidated belief structure.

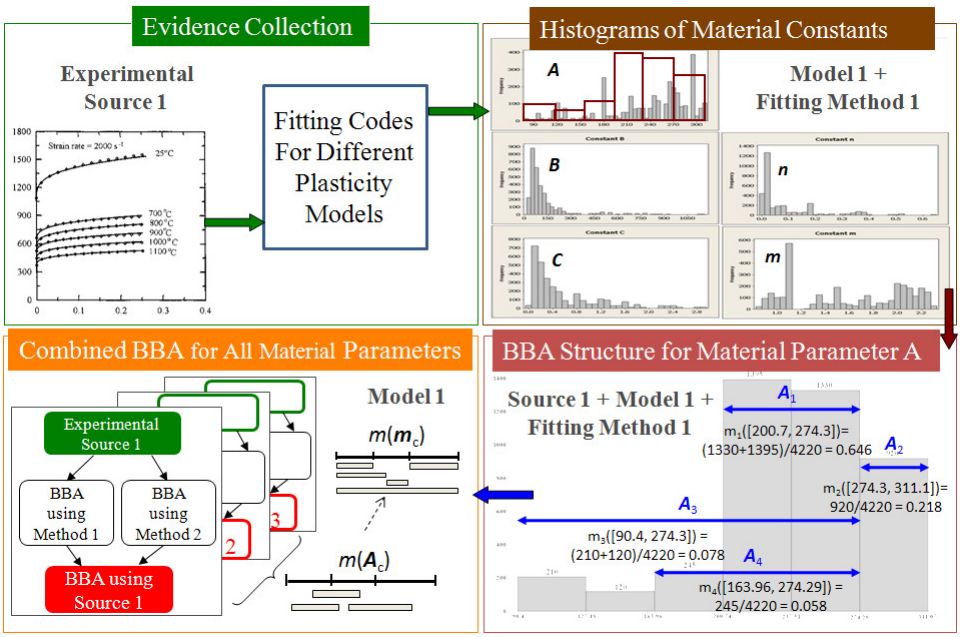

Figure 7.3 Interaction between computational codes for uncertainty representation of material constants

7.1.2.2 Joint belief structure construction

Constructed belief structures of all uncertain variables are fed into computational codes that are able to construct their joint belief structure. As mentioned previously, with propagation of this joint belief structure, effects of uncertainties in all uncertain variables on structural response is considered. However, propagation of this joint belief structure ignores field uncertainty of material caused by spatial variation of material constants. In fact, propagation of a joint belief structure for uncertain material constants in a structure assumes they are uniform across the whole structure. The presented EBDO framework is equipped by computational codes that are able to construct a field joint belief structure and propagate it through FE simulations to accommodate material field uncertainty.

Each cell of such field joint belief structures includes a number of sub-cells that are members of the constructed joint belief structure for all uncertain variables. The number of sub-cells in each cell of the field joint belief structure equals to number of

regions of structure that are more prone to have different material constants as a result of spatial variation in material properties. Each sub-cell that is a member of the constructed belief structure for uncertain material constants represents material properties of the related region of the engineering structure recognized potentially to have different material properties (represented by material constants) as opposed to the other regions.

From the computational side, construction of joint belief structures requires development of computational codes being able to store discrete spaces of represented uncertainty efficiently. This becomes very challenging when considering spatial variation of material behavior among different regions of a product in uncertainty modeling process as the field joint belief structure includes a huge number of disjoint members. To accommodate this, computational codes are developed in this study.

7.1.2.3 Uncertainty propagation

As depicted by Figure 7.4, uncertainty propagation of a joint belief structure with huge numbers of discrete cells requires heavy interaction between different computational codes written for design and analysis of computer experiments, non-linear FE simulations of large deformation process, metamodeling and global optimization methods to obtain bounds of simulation response for each member of the joint belief structure, combination of propagated belief structures provided by different formulation of plasticity models, as well as computational codes for saving the obtained propagated belief structure.

Note that propagation of a field joint belief structure is considerably more computationally challenging than that of a joint belief structure of uncertain material constants. In fact, consideration of field material uncertainty adds to the computational

complexity of the presented EBDO framework considerably. Design and analysis of computer experiments is more computationally complex in propagation of a field joint structure. Detail procedures for EBDO of engineering structures with and without consideration of field material uncertainty using the presented computational framework is explained in the next chapter by two illustrative examples.

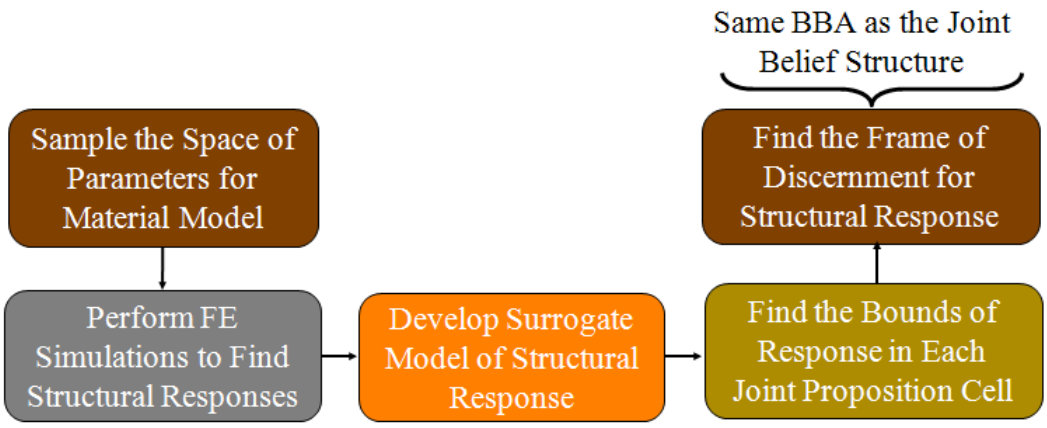

Figure 7.4 Interaction between computational codes for propagation of a constructed joint belief structure

CHAPTER VIII

EVIDENCE-BASED DESIGN OPTIMIZATION OF EXTERNALLY STIFFENED CRUSH TUBES

Recently, Salehghaffari et al. (2011) developed a new design concept to control energy absorption characteristics of thin-walled circular tubes under axial compression. By machining wide circumferential grooves from the outer surface of a thick-walled tube at specific intervals, they arrived at a general design concept for an integrally stiffened (monolithic) tube as shown in Figure 8.1. The thicker portions (rings) essentially act as external stiffeners for the enclosed thin-walled tube sections. When the stiffened tube is subjected to axial compression, the thin-walled sections between two adjacent ring stiffeners fold resulting in enhanced crush energy absorption.

The number of ring stiffeners in Figure 8.1 is defined as $N + 1$, where N represents the number of thin-walled sections along the length of the tube. The stiffener section is defined by parameters d and w whereas the thin-walled portions are defined by parameters t and S. In thick (stiffened) sections, the total wall thickness is defined as $t + d$. The inner diameter, $D_i = 500$ mm and length, $L = 250$ mm of the tube are held fixed while the other geometric parameters are allowed to vary in the optimization process. It should be noted that S, w and N are related as

$$NS + (N+1)\, w = L \tag{8.1}$$

Specific energy absorption (SEA), which is the ratio of absorbed energy to component mass, gives an accurate measure of energy absorption capacity of the

component. (salehghaffari et al. 2010, 2011) On the other hand, as mentioned in the literature (Jones, 1989; Alghamdi, 2001) an ideal energy-absorbing design should provide a desirable constant mean crush force-crush while the tube is crushed under axial loading. The peak reaction force that typically occurs soon after the start of the crush process is due to the initial elastic resistance and is usually much greater than the subsequent peaks.

A deterministic optimization of this tube model, focusing on the geometric properties of the tube with simple model of plasticity with no consideration of uncertainty, appears in Salehghaffari et al. (2010, 2011). Here, the same problem is used as an example to describe the presented EBDO methodology for optimization under uncertainty.

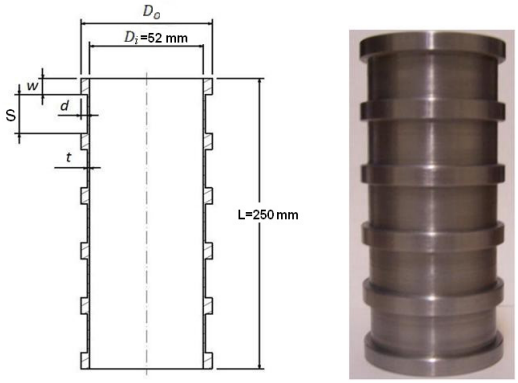

Figure 8.1 Externally stiffened circular tube with associated geometric design parameters (salehghaffari et al. 2010)

For EBDO of externally stiffened tubes, we seek the optimum size of the structure in light of epistemic uncertainty in material behavior over large deformation. With desire to maximize SEA while keeping the peak load less than its critical value P_{max}^{C}, and consideration of epistemic uncertainties embedded in dynamic material behavior that

make the simulation responses (SEA and P_{max}) uncertain, the EBDO problem is formulated as

$$\begin{aligned} & Maximize \quad f = SEA(X) \\ \text{s.t} \quad & Pl\{ P_{max}(X) \leq P_{max}^{C}\} \geq Pl_{all} \\ & X^{L} \leq X \leq X^{U} \end{aligned} \tag{8.2}$$

where *Pl* represents the plausibility of an event . The evidence-based design constraint in Eq. (8.2) imposes a limit on plausibility that the maximum peak load (P_{max}) does not exceed its critical value (P_{max}^{C}) due to the uncertainties. Note that depending on the desired level of reliability, Pl_{all} can change. As can be seen in Eq. (8.2), the objective function (*SEA*) is deterministic whereas the constraint function is non-deterministic, although in a more general EBDO framework, the objective function could also be non-deterministic.

For optimization solution of Eq. (8.2), construction of mathematical functions that relate the objective function (SEA) and evidence-based design constraint ($Pl\{ P_{max}(X) \leq P_{max}^{C}\}$) to design variables ($X$) are necessary. As discussed earlier, metamodels are used for approximation of the constraint function. The procedure to establish a surrogate model for the objective function is considerably less challenging and less expensive than that of the evidence-based design constraint as can be seen in the next section.

8.1 Representation of uncertainties in Johnson-Cook plasticity model

Some of the reported constants of JC plasticity for AISI 4340 are shown in Table 8.1. Using the experimental stress-strain curves provided in the literature (Gray et al., 1994) for AISI 4340 Steel (Table 8.2) and the procedure discussed in chapter 4, a fairly diverse range of material constants is obtained as shown in Table 8.3.

Table 8.1 Johnson-Cook material constants suggested by different references

Reference.	Johnson-Cook material constants				
	A	B	n	C	m
Gray et al, 1994	1579	1316	0.65	0.0028	0.85
Meyers, 1994	792	510	0.26	0.014	1.03
Rule, 1997	396	820	0.397	0.014	1.001

Table 8.2 Testing conditions for the experimental sources of data AISI 4340 Steel

Curve	Type	Strain Rate (s^{-1})	Temperature (K)
1	Tension	0.0004	293
2	Tension	0.009	293
3	Tension	32	293
4	Tension	117	293
5	Tension	604	494
6	Tension	1500	473
7	Tension	2500	298
8	Tension	650	733
9	Tension	2000	873
10	Tension	1500	673

Table 8.3 Johnson-Cook material constants for AISI 4340 Steel using different fitting approaches

Fitting Method 1					Fitting Method 2				
A	B	n	C	m	A	B	n	C	m
638.37	266.95	0.1218	0.0763	0.81	804	365.25	0.151	0.014	1.252
635.82	265.89	0.1218	0.0763	1.60	804	365.25	0.151	0.014	2.895
833.52	373.66	0.2833	0.0157	1.00	804	365.25	0.151	0.122	0.43
832.57	373.23	0.2833	0.0157	2.51	804	365.25	0.151	0.122	0.715
1188.59	532.83	0.2833	0.0633	0.38	804	365.25	0.151	0.083	0.533
1109.75	497.49	0.2833	0.0633	0.68	804	365.25	0.151	0.083	0.94
1102.29	494.14	0.2833	0.0633	0.85	771	405.75	0.322	0.027	1.168
906.46	178.69	0.2239	0.0282	0.89	771	405.75	0.322	0.027	2.433
904.29	178.26	0.2239	0.0282	2.06	771	405.75	0.322	0.137	0.449
1424.29	280.77	0.2239	0.0582	0.35	771	405.75	0.322	0.137	0.715
1308.70	257.98	0.2239	0.0582	0.67	771	405.75	0.322	0.109	0.518
1300.69	256.40	0.2239	0.0582	0.78	771	405.75	0.322	0.109	0.853
738.02	145.48	0.2239	0.0057	3.77	705	116.54	0.071	0.095	0.79
329.90	137.96	0.1218	0.417	0.84	705	116.54	0.071	0.095	1.65
493.58	206.41	0.1218	0.1815	2.08	705	116.54	0.071	0.213	0.474
1005.93	450.95	0.2833	0.0492	0.90	705	116.54	0.071	0.213	0.72
936.69	419.91	0.2833	0.0376	2.71	705	116.54	0.071	0.152	1.016
1139.50	224.63	0.2239	0.0485	0.90	705	116.54	0.071	0.152	0.62
1043.04	205.61	0.2239	0.0414	2.01					

Following the methodology for representation of uncertainty discussed in chapter 2, separate belief structures for each uncertain material constant of JC plasticity model are constructed and shown in Table 8.4. For the purpose of uncertainty propagation, a consolidated belief structure that reflects all fuzzy expert opinions and diverse data from different sources of information should be constructed. Here, we employed Yager's combination rule of evidence to combine belief structures provided by fitting method 1 and 2 into a single belief structure as shown in Table 8.4. As indicated, a large degree of conflict exists between the data provided by the fitting methods 1 and 2 for constants *A, B* and *n*. The combined belief structure for each material constant shown in Table 8.4 will be used for uncertainty propagation.

Table 8.4 Individual and combined belief structures for material constants of Johnson-Cook

Interval	Method 1		Method 2		Combined	
	Range	BBA	Range	BBA	Range	BBA
			Constant *A*			
1	[329.9, 877.1]	2/19	[705.0, 724.8]	6/18	[705.0, 724.8]	0.1228
2	[603.5, 877.1]	5/19	[764.4, 804.0]	12/18	[764.4, 804.0]	0.2456
3	[877.1, 1150.7]	8/19	-	-	[329.9, 1424.3]	0.6316
4	[1150.7,1424.3]	4/19	-	-	-	-
			Constant *B*			
1	[137.96, 295.91]	12/19	[116.54, 212.95]	6/18	[137.96, 212.95]	0.2807
2	[137.96, 453.85]	4/19	[309.35, 405.75]	12/18	[309.35, 405.75]	0.1404
3	[453.85, 532.83]	3/19	-	-	[116.54, 532.83]	0.5789
			Constant *n*			
1	[0.1218,0.1756]	4/19	[0.0710, 0.1547]	12/18	[0.1218, 0.1547]	0.1404
2	[0.1756,0.2833]	15/19	[0.2383, 0.3220]	6/18	[0.2383, 0.2833]	0.2632
3	-	-	-	-	[0.0710, 0.3220]	0.5965
			Constant *C*			
1	[0.057, 0.088]	17/19	[0.0140, 0.0638]	4/18	[0.0569, 0.0638]	0.2222
2	[0.057, 0.417]	2/19	[0.0638, 0.1633]	12/18	[0.0637, 0.0881]	0.6959
3	-	-	[0.0638, 0.2130]	2/18	[0.0637, 0.1634]	0.0702
4	-	-	-	-	[0.0637, 0.2131]	0.0117

Table 8.4 (Continued)

	Constant *m*					
1	[0.3523, 1.0353]	12/19	[0. 43, 0.923]	11/18	[0.4299, 0.9231]	0.6111
2	[0.3523, 3.7671]	7/19	[0. 43, 1.416]	4/18	[0.4299, 1.0354]	0.2456
3	-	-	[0. 43, 2.895]	3/18	[0.4299, 1.4160]	0.0819
4	-	-	-	-	[0.4299, 2.8951]	0.0614

8.2 Mathematical formulation for objective function

Metamodels are used to construct the mathematical model relating objective function to design variables. Since in the presented EBDO framework, material uncertainties are not incorporated in the calculation of objective function, an experimentally verified set of Johnson-Cook material constants (Gray et al., 1994) shown in Table 6.1 is used in FE simulation of all generated random samples.

8.2.1 Design and Analysis of Computer Experiments

RBF metamodels are used to establish surrogate models relating the objective function (*SEA*) to design variable vector $\boldsymbol{X}^T = [w, S, d, t]$. Here, it is found that the multiquadric RBF with $\phi(r) = \sqrt{r^2 + c^2}$ and c = 0.01 is best suited for modeling the objective function.

For the sake of simplifying the optimization problem, we decided to search the optimal design through design samples with six stiffeners. This assumption reduces the number of design variables from 4 to 3 since w is no longer an independent design variable and is related to design variable S by Eq. (8.1). Hence, from Figure 8.1, it can be seen that the upper bound for S is given by

$$S_{upper} = \frac{L}{N} = \frac{250}{5} = 50 \tag{8.3}$$

While stiffeners significantly help to stabilize the collapse process, they may not contribute to plastic deformation and energy absorption. We are seeking an optimal

design that produces stroke efficiency of more than 50%. That is at least 50% of the tube length is crushed. Considering this design criterion, the lower bound for *S* is found to be

$$S_{lower} = \frac{L}{2N} = \frac{250}{2\times5} = 25 \tag{8.4}$$

Also, based on previous observation of the effect of *t* and *d* on plastic collapse mode and the corresponding mean crush force, the following bounds are imposed.

$$1 \leq t \leq 2.6 \qquad\qquad 0 \leq d \leq 3 \tag{8.5}$$

Using Latin hypercube sampling (LHS) technique and the selected bounds on the design variables, we selected 25 design (training) points as shown in Table 8.5. Note that the total wall thickness in the stiffened regions is $d + t$.

To assess the overall accuracy of the constructed surrogate model, PRESS, and $R^2_{Prediction}$ error statistics were considered. To estimate these error statistics, the accuracy of the RBF predictions were based on fitting a model using responses at 24 training points and measuring the prediction at the $25th$ point excluded from the set. The average of 24 different surrogate models was used to obtain the associated error statistics. This offers *PRESS* = 512.9 and $R^2_{Prediction} = 0.8512$ for the metamodel constructed for the objective function.

Table 8.5 Design points used in RBF fitting of the objective function

Design #	d (mm)	t (mm)	S (mm)	w (mm)	weight (Kg)	Design #	d (mm)	t (mm)	S (mm)	w (mm)	weight (Kg)
1	0.375	1.733	46.875	2.604	0.580	14	0.750	2.267	26.042	19.965	0.885
2	1.875	1.200	45.833	3.472	0.447	15	2.375	1.400	43.750	5.208	0.564
3	0.625	2.067	32.292	14.757	0.765	16	0.875	1.000	39.583	8.681	0.388
4	1.625	2.467	38.542	9.549	0.962	17	2.625	2.000	33.333	13.889	0.935
5	1.750	2.400	42.708	6.076	0.895	18	1.375	1.933	48.958	0.868	0.65
6	2.750	1.333	37.500	10.417	0.680	19	2.875	1.667	44.792	4.340	0.66
7	0.100	1.867	29.167	17.361	0.634	20	0.125	2.200	36.458	11.285	0.746
8	1.500	1.600	25.000	20.833	0.789	21	1.125	1.133	31.250	15.625	0.513
9	0.250	1.533	40.625	7.813	0.52	22	1.250	1.067	35.417	12.153	0.474
10	2.000	2.533	34.375	13.021	1.076	23	2.250	1.467	41.667	6.944	0.616
11	0.500	2.133	30.208	16.493	0.778	24	1.000	2.333	28.125	18.229	0.934
12	2.125	1.267	47.917	1.736	0.447	25	2.500	1.800	27.083	19.097	1.000
13	1.500	1.800	37.500	10.417	0.728						

8.2.2 Description of the FE Models

Axial crush simulations are performed using explicit FEA code LS-DYNA, version 971. The basic geometry of the FE model (Figure 8.2) was created according to the user code. (Hallquist, 1993) Through parameterization, it was possible to readily update the FE mesh for different combinations of design variables.

The impact loading is modeled by a rigid wall of 150 kg mass impacting the top edge of the tube with an initial velocity of $40\ \mathrm{m/s}$. Also, all nodes on the bottom edge of the tube are constrained in all degrees of freedom. A "single-surface" interface is selected to prevent penetration of contacting elements in the tube elements. Friction coefficient for rigid wall contact is set to 0.25 and for single-surface contact is set to 0.15.

Solid (hex8) elements are used in all computer simulations. The sensitivity of the simulated results to the mesh density for each computer experiment was analyzed in order to choose a suitable element size for the simulation. In some computer experiments, program termination due the appearance of negative volume of solid elements was observed. This is mainly caused by the element Jacobian calculation at geometric points of the outer boundary of highly deformed solid elements. (Salehghaffari et al., 2011) In

some computer experiments, rapid compression of elements in the stiffener sections as well as the nearby elements in the thin-walled sections results in occurrence of negative volume in solid elements. To avoid this, we follow suggestions provided in our previous study in nonlinear FE simulations of externally stiffened crush tubes. Generally, increasing element size, using hourglass and Interior contact setting option can resolve the problem of negative volume in solid elements.

All numerical simulations of design samples were performed on a Pentium PC 3.2 GHz with a typical simulation time of 7 to 9 hours.

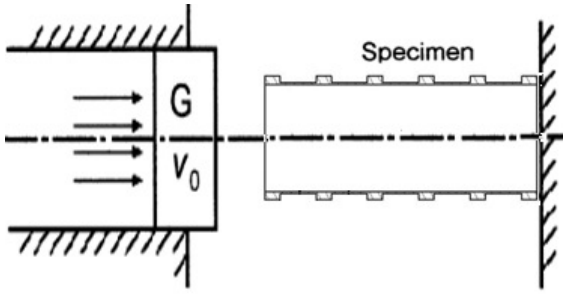

Figure 8.2 FE model of the externally stiffened tube under axial impact load

8.2.3 FE Simulation Results

The simulation results for different tube samples are given in Table 8.6. They include the values for SEA, maximum and average crush forces (P_{max}, P_{mean}), crushing time and stroke or crush length. As Table 8.6 shows, a wide range of simulation results can be obtained. Figure 8.3 also shows the diverse collapse modes of stiffened tubes of different geometric parameters. This implies the value of optimization analysis for stiffened tubes in order to design a structure with the desired energy absorption characteristics.

Here, the crush length refers to the maximum distance traveled by the rigid wall before crushing time exceeds 5 ms; the crush load at final stages of deformation exceeds the initial peak load due to the deformation of thick areas of tube; unstable crushing happens due to the local bending of the structure. Similar to the study performed by Salehghaffari et al., (2011), a lateral rotation or bending of 10 degree in the tube axis is used as a criterion for identifying the mixed crush modes that are buckling dominated.

All simulation responses provided in Table 8.6 are based on the mentioned criterion for determination of crush length. For all samples, the simulation is set to stop at 5 ms. However, in some cases, this simulation time is shortened to a time that the observed crush load exceeds the peak load (P_{max}) at the initial stages of crushing. A dramatic increase of crush load at final stages of progressive crushing relates to deformation of stiffened areas of the structure requiring larger crush loads than that of the un-stiffened areas. This can be verified by giving a closer attention to the different stages of deformation of stiffened tubes along with their corresponding load-displacement relationship as shown in Figures 8.4 and 8.5 for sample 8.

Simulation results indicate that samples with considerable difference in thickness between thick and thin areas of the stiffened tube experience significant increase in crush load at their final stages of the crushing process. Despite the deformation of their stiffened areas during the crushing process, the crush load of some samples do not change significantly and exceed the peak load allowing the progressive crushing to continue until the crush time of 5 ms is reached. As mentioned, this is mainly because of the fairly close thickness of stiffened and un-stiffened areas of the structure. Also, note that in some special cases, deformation reaches a point that significant increase in crush load is needed for further deformation of the tube.

Table 8.6 FEA results for the randomly selected DOE design points

Design	SEA (kJ/kg)	P_{max} (kN)	P_{mean} (kN)	L (mm)	Time (ms)	Design	SEA (kJ/kg)	P_{max} (kN)	P_{mean} (kN)	L (mm)	Time (ms)
1	37.28	299.41	127.71	169.3	4.50	14	58.82	436.12	295.31	176.27	5
2	31.79	186.29	73.99	192.09	5	15	34.36	238.02	102.26	189.53	5
3	46.95	379.25	197.51	181.84	5	16	29.69	168.71	59.4	193.82	5
4	42.95	676.47	256.60	161.04	4.50	17	28.59	378.56	196.18	136.27	3.65
5	45.13	408.56	227.25	177.73	5	18	43.91	327.62	154.41	184.83	5
6	27.46	283.38	111.37	167.75	4.4	19	38.13	269.99	139.18	180.83	4.85
7	51.81	335.19	178.83	183.68	5	20	51.08	392.92	212.10	179.65	5
8	28.75	359.27	170.28	133.23	3.5	21	27.27	238.76	80.68	173.36	4.5
9	42.42	253.54	116.71	188.99	5	22	33.03	205.27	81.25	192.67	5
10	31.56	499.98	252.45	134.53	3.7	23	34.41	236.82	120.69	175.65	4.65
11	58.58	376.3	251.68	181.1	5	24	60.27	476.5	319.58	176.14	5
12	32.73	201.89	76.29	191.79	5	25	18.14	586.7	158.76	114.26	3
13	36.15	321.19	148.356	180.06	4.85						

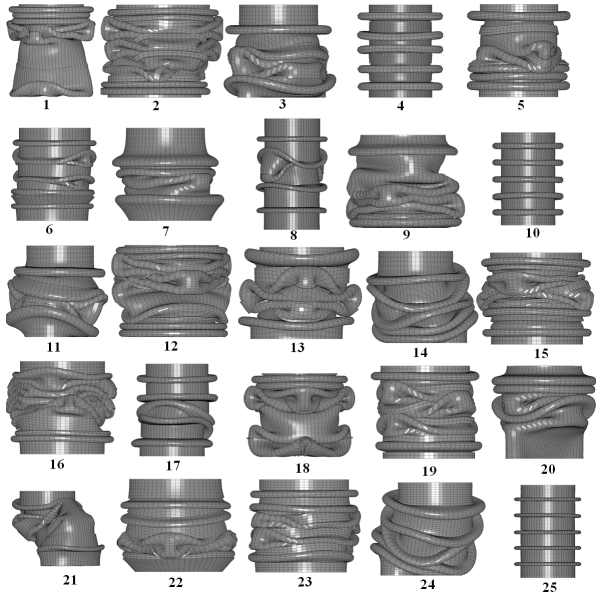

Figure 8.3 Collapsed shapes of design samples obtained from FE simulations (not to scale)

Comparison of the dynamic loading simulation results of samples in Table 8.6 with those obtained in our previous study (Salehghaffari et al., 2011) under a quasi-static loading condition reveals the effect of strain hardening of AISI 4340 Steel in increasing

the energy absorption of the structure. Dynamic impact loading gives an SEA that is twice as high as that in quasi-static compression.

For a more thorough understanding of mechanics of deformation of externally stiffened tubes, the reader is referred to our previous work (Salehghaffari and Rais-Rohani, 2011).

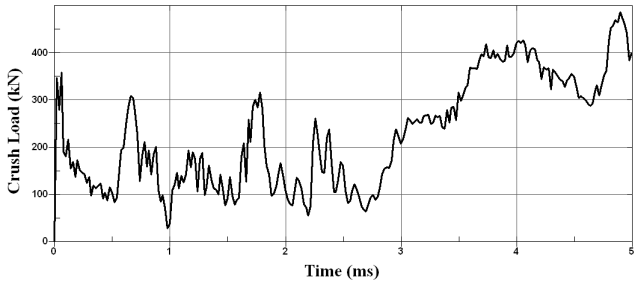

Figure 8.4 Load history of sample 8 during its crushing process

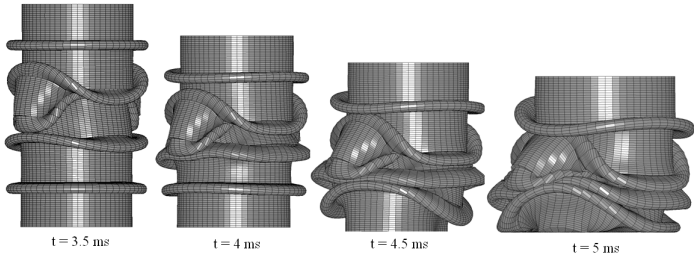

Figure 8.5 Collapse shapes of sample 8 at different time steps

8.3 Mathematical modeling of evidence-based constraint function

Evaluation of evidence-based constraint function $Pl\{ P_{max}(X) \leq P_{max}^{C}\}$ for each design point given in Table 8.5 requires construction of a propagated belief structure for P_{max} that can be derived through propagation of the represented material uncertainties shown in Table 8.4. This is a very computationally expensive and tedious task. To reduce the computational cost of the presented EBDO framework, instead of propagating the

material uncertainty for all design variables (see Table 8.5), design points 1, 4, 11, 14, 18 and 24 are selected. As can be seen in Figure 8.3 and Table 8.6, these design points have completely different collapse behavior, and their crushing simulation results are more likely to be affected by uncertainties in dynamic material behavior. Through propagation of material uncertainties for these selected design points, the associated value of $Pl\{P_{max}(X) \leq P_{max}^{C}\}$ for each of them can be determined. Hence, with consideration of design points 1, 4, 11, 14, 18 and 24 and their associated plausibility function $Pl\{P_{max}(X) \leq P_{max}^{C}\}$, it is possible to construct the evidence-based constraint function with less computational effort.

8.3.1 Propagation of material uncertainties

The represented uncertainties of Johnson-Cook material model for AISI 4340 Steel (see Table 8.4) are propagated through FE crush simulation of design points 1, 4, 11, 14, 18 and 24 under axial impact load with the aim to determine the propagated belief structure of peak load for each of them.

Surrogate models are developed to facilitate the uncertainty propagation process. LHS technique is adopted to generate 12 training points for uncertain material constants as identified in Table 8.7. Intervals of uncertainty (universal set) for all uncertain material constants that are provided by Table 8.4 are considered in selecting the bounds on uncertain variables.

Table 8.7 Training points used in generating the RBF metamodels for peak load

Uncertain point	A (MPa)	B (MPa)	n	C	m
1	429.39	494.99	0.231	0.0853	2.447
2	628.37	267.92	0.094	0.1562	1.102
3	1026.34	457.14	0.1176	0.0711	0.654
4	1225.32	343.61	0.254	0.2130	1.326

Table 8.7 (Continued)

5	1424.30	419.30	0.208	0.1279	0.430
6	827.35	532.83	0.322	0.0995	1.774
7	926.85	116.54	0.071	0.1704	1.550
8	329.90	230.07	0.185	0.1420	2.895
9	528.88	305.76	0.139	0.0569	1.999
10	727.86	192.23	0.276	0.1988	2.671
11	1125.83	381.45	0.299	0.1137	2.223
12	1324.81	154.38	0.162	0.1846	0.878

FE crush simulation of the selected design points 1, 4, 11, 14, 18 and 24 as described earlier are performed using all the provided sets of material constants in Table 8.7. Table 8.8 summarizes the simulation responses of the selected design points using each set of material constants in Table 8.7. A wide range of variation in simulation responses can be observed due to the variation in material constants of the JC plasticity model. This indicates the importance of considering material uncertainties in analysis and design of structures experiencing large deformation process. As an example, to show the significance of JC material constants on the simulation response, the predicted collapse shapes of design point 1 using each set of material constants given in Table 8.8 are shown in Figure 8.6.

Considering the calculated peak load values shown Table 8.8, it is possible to construct metamodels that relate the uncertain variables to peak crush load. Again, $R^2_{Prediction}$ error statistic described earlier is used to assess the overall accuracy of the constructed surrogate model, and its estimated values are provided in Table 8.9 for each of the selected design points. Note that the multiquadric formulation with c = 1 is used for all the constructed metamodels except that of the design point 18 with c = 0.85. Results indicate that the constructed metamodel can be employed acceptably in determination of the propagated belief structure for peak load.

Table 8.8 E simulation response of each selected design point using the provided randomly selected sets of Johnson-Cook material constants

point	Design#1					point	Design#4				
	SEA (kJ/kg)	P_{max} (kN)	P_{mean} (kN)	L (mm)	Crushing Stability		SEA (kJ/kg)	P_{max} (kN)	P_{mean} (kN)	L (mm)	Crushing Stability
1	31.78	200.01	96.97	190.06	5	1	30.44	391.65	160.40	182.59	4.4
2	33.77	251.36	103.32	189.60	5	2	36.19	430.76	212.00	164.22	4.5
3	45.70	388.61	143.03	185.33	5	3	52.75	584.01	249.83	172.13	4.9
4	53.59	404.77	169.06	183.86	5	4	53.06	587.40	305.79	166.91	4.8
5	44.315	443.74	166.47	154.4	4.1	5	55.94	644.75	312.65	172.12	5
6	44.17	301.33	137.39	186.45	5	6	44.27	552.43	265.24	160.57	4.5
7	39.31	316.84	121.62	187.45	5	7	51.58	542.85	280.31	177.02	5
8	23.00	147.97	69.21	192.78	5	8	22.08	292.17	129.19	164.45	4.4
9	31.03	228.61	94.62	190.26	5	9	32.63	391.37	189.67	165.51	4.5
10	32.35	245.91	100.37	189.49	5	10	36.36	468.70	193.5	164.18	4.5
11	50.18	376.29	157.59	184.7	5	11	48.12	563.45	294.22	157.33	4.5
12	42.52	423.41	157.47	156.6	4.2	12	53054	611.28	300.02	171.68	5
	Design#11						Design#14				
1	38.390	276.43	160.8	185.74	5	1	41.36	331.92	201.69	181.48	4.9
2	45.37	314.65	192.71	183.17	5	2	47.12	362.4	230.3	181.06	5
3	57.11	504.16	248.85	178.55	5	3	64.87	571.15	328.16	174.94	5
4	62.44	516.34	273.91	177.34	5	4	60.81	611.15	332.56	161.82	4.6
5	61.29	556.7	269.11	177.18	5	5	58.09	650.38	295.29	174.11	5
6	55.85	360.03	240.58	180.6	5	6	61.15	435.17	306.72	176.44	5
7	53.44	386.12	230.86	180.08	5	7	57.57	434.65	286.94	177.54	5
8	27.67	192.35	113.71	189.35	5	8	28.83	227.36	135.85	187.80	5
9	37.87	288.93	159.28	185.00	5	9	38.26	342.17	187.30	180.76	5
10	43.88	311.19	186.27	183.27	5	10	48.16	361.59	235.39	181.05	5
11	63.86	472.95	280.30	177.24	5	11	71.51	555.84	367.72	172.11	5
12	50.30	534.47	241.82	161.82	4.5	12	61.25	631.58	312.65	173.37	5
	Design#18						Design#24				
1	35.23	218.32	121.91	187.89	5	1	43.93	327.38	231.10	177.18	4.9
2	36.47	279.76	126.54	187.33	5	2	46.37	427.45	256.63	168.77	4.7
3	50.12	432.41	178.56	182.46	5	3	65.50	589.4	350.80	174.40	5
4	56.89	454.17	204.56	180.77	5	4	74.57	673.79	408.92	170.33	5
5	49.38	503.60	216.86	148	4	5	64.34	698.72	347.81	172.79	5
6	45.70	331.84	161.64	183.78	5	6	63.20	497.7	337.08	175.12	5
7	42.48	346.32	149.01	185.20	5	7	60.22	502.71	327.94	171.51	4.8
8	24.90	203.28	84.42	191.72	5	8	26.71	228.5	147.27	169.4	4.5
9	33.20	259.53	114.60	188.29	5	9	46.00	353.58	236.44	181.72	5
10	36.28	274.28	125.89	187.30	5	10	50.78	370.11	263.76	179.83	5
11	52.92	418.91	188.87	182.12	5	11	74.20	568.8	405.99	170.71	5
12	54.89	477.23	196.61	181.46	5	12	70.98	661.13	385.06	172.18	5

Table 8.9 Error estimation of RBF models to relate uncertain material constants to peak load

Design Point	$R^2_{prediction}$	Design Point	$R^2_{prediction}$
1	0.9231	14	0.8718
4	0.9109	18	0.8370
11	0.8651	24	0.9363

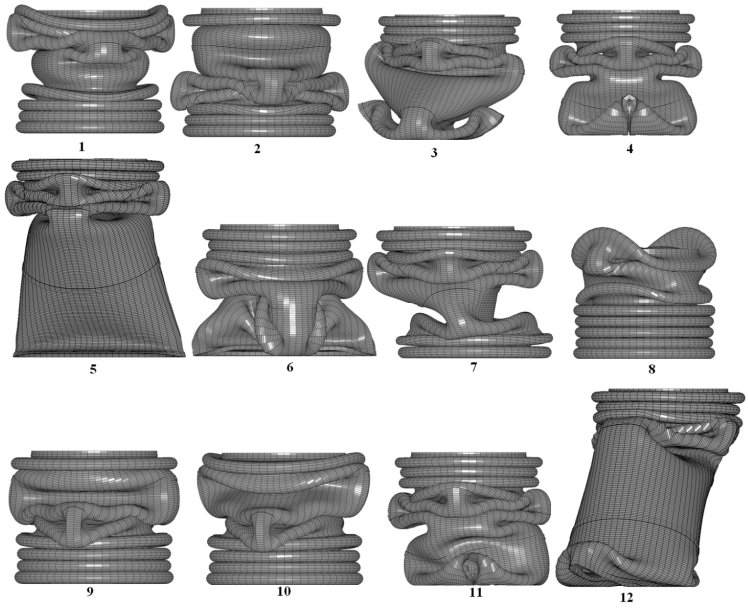

Figure 8.6 Collapsed shapes of design point 1 for each randomly selected set of uncertain material constants

A joint BBA is obtained by the Cartesian product of the belief structures of all uncertain variables for a structural system. (Bae et al, 2004, 2004a) This involves the multiplication of final BBA found for each subinterval of one uncertain variable with those of the other variables involved in the Cartesian product. In this case, the constructed joint belief structure contains 432 Cartesian products.

Propagation of uncertainty requires the determination of the maximum and minimum values (bounds) of the response for each Cartesian product of the constructed joint belief structure, where each uncertain constant can take any value within the corresponding subinterval range. Thus, the constructed metamodels for each selected design points 1, 4, 11, 14, 18 and 24 relating the peak load to five uncertain material constants of Johnson-Cook material model, is maximized and minimized 432 times with side constraints defined by the associated Cartesian products of the constructed joint belief structure using Genetic Algorithm (GA) . This provides bounds of peak load

associated with each Cartesian product of the constructed joint belief structure that can be interpreted as the propagated belief structure for each of the selected design points.

It should be noted that the BBA of each interval of uncertainty for peak load equals to that of the corresponding Cartesian product of the joint belief structure. The original constructed propagated belief structure of peak load includes 432 intervals with BBA for each of the selected design points. The reduced propagated BBA is shown in Table 8.10. In the reduced propagated BBA, when the difference between the minimum and maximum peak loads in two Cartesian products was less than 20, 35, 30, 25, 20 and 20 kN for each of design points 1, 4, 11, 14, 18 and 24 respectively, the Cartesian products were treated as one with BBA equal to the sum of BBA of the underlying products. As a result of this size reduction, the belief structure for peak load was reduced significantly from 432 to 16 for design points 1, 4, 14 and 24 and to 14 for design points 11 and 18. Of course, the amount of reduction in belief structure size depends on the tolerance value selected. Note that for the purpose of plausibility estimation discussed later, the original (unreduced) propagated belief structures are used.

Table 8.10 Reduced propagated belief structures of peak load for the selected design points

Design#1		Design#4		Design#11	
Range	BBA	Range	BBA	Range	BBA
[280.47, 309.97]	0.086872	[473.39,535.17]	0.196340	[328.66,374.90]	0.066382
[253.42, 310.79]	0.010100	[411.42,534.43]	0.034354	[297.99,362.14]	0.002974
[233.32, 291.82]	0.000128	[452.13,494.37]	0.004183	[363.13,420.36]	0.050294
[233.33, 321.93]	0.003202	[401.87,494.43]	0.000301	[332.37,430.18]	0.092276
[276.92, 340.83]	0.175230	[438.25,576.78]	0.121110	[298.28,414.16]	0.003809
[253.45, 335.60]	0.006415	[385.64,576.96]	0.002953	[321.18,467.76]	0.146060
[244.13, 356.14]	0.005969	[437.59,613.53]	0.001336	[289.55,461.70]	0.002353
[301.82, 343.06]	0.000922	[385.28,612.12]	0.005423	[372.92,457.56]	0.004290
[286.25, 371.15]	0.079033	[478.01,572.80]	0.007828	[221.95,588.28]	0.178820
[265.56, 368.91]	0.000569	[401.60,688.53]	0.405600	[187.00,584.80]	0.033020
[200.18, 466.39]	0.278770	[312.91,685.17]	0.043561	[253.36,619.46]	0.045334
[168.93, 466.18]	0.123400	[360.64,671.45]	0.057289	[219.61,628.58]	0.312590
[144.91 ,454.19]	0.001305	[362.07,707.21]	0.101510	[187.78,617.45]	0.048288
[194.17, 486.55]	0.192530	[294.07,648.56]	0.003358	[183.34,655.74]	0.013613
[148.51, 482.50]	0.027303	[300.75,727.88]	0.013391		
[174.11, 495.30]	0.008356	[365.82,748.62]	0.001559		
Design#14		**Design#18**		**Design#24**	
[384.70,436.27]	0.058999	[316.12,355.89]	0.100110	[440.49,480.89]	0.047423
[347.58,436.72]	0.005715	[290.58,352.49]	0.024467	[372.29,480.26]	0.003805
[417.96,478.44]	0.050754	[287.35,372.80]	0.026792	[467.59,531.18]	0.133750
[389.36,478.67]	0.034041	[266.41,336.71]	0.000065	[394.78,531.00]	0.019928
[382.94,510.39]	0.101970	[266.38,368.35]	0.000228	[440.41,575.76]	0.152570
[343.67,510.42]	0.009592	[316.21,382.90]	0.119070	[354.38,558.71]	0.010453
[350.25,482.18]	0.004581	[287.16,397.82]	0.024860	[399.29,581.46]	0.000511
[434.42,503.56]	0.018055	[266.17,395.82]	0.000183	[339.21,681.45]	0.073737
[395.40,548.69]	0.079520	[320.24,414.70]	0.072656	[266.59,682.21]	0.009574
[350.15,549.95]	0.005207	[238.42,523.48]	0.269120	[336.37,730.13]	0.298650
[266.29,673.90]	0.248310	[214.38,523.50]	0.129640	[257.86,729.76]	0.030226
[227.24,674.42]	0.035364	[187.84,520.02]	0.005838	[222.15,680.40]	0.000360
[297.91,696.19]	0.034934	[227.45,545.07]	0.196770	[214.71,727.25]	0.001016
[264.20,702.84]	0.257600	[202.46,544.90]	0.030285	[336.97,773.68]	0.190810
[236.03,700.31]	0.036154			[257.71,773.37]	0.026187
[208.35,706.95]	0.019300			[213.41,772.99]	0.001097

As expected, predicted values of peak load for each of the selected design points using the experimentally verified JC material constants shown in Table 8.6 are included in almost all propagated uncertainty intervals (see Table 8.10). This verifies the correctness of the presented uncertainty representation and propagation approach.

8.3.2 Evaluation of EBDO constraints

Using the propagated belief structure, the values of the evidence-based constraint in Eq. (8.2) for the selected design points are obtained through belief or plausibility estimation of the desired space of peak load, $P_{max}(X) \leq P_{max}^{C}$, with P_{max}^{C} = 250, 300 and 350 kN as given in Table 8.11. The large gap between the belief and plausibility of the peak load is indicative of the amount of epistemic uncertainty embedded in the JC material models and makes it difficult to evaluate simulation accuracy of JC material models with only belief and plausibility measures. Hence, the plausibility decision function is also used as a possible evidence-based design constraint with the corresponding results also provided in Table 8.11.

Table 8.11 Assessment of evidence based constraint for different values of P_{max}^{C}

Design No.	$P_{max} \leq 250\ kN$			Design No.	$P_{max} \leq 250\ kN$		
	Bel	Pl	Pl_dec		Bel	Pl	Pl_dec
1	0.000	0.640	0.146	14	0.000	0.355	0.008
4	0.000	0.000	0.000	18	0.000	0.632	0.063
11	0.000	0.630	0.069	24	0.000	0.026	0.001
	$P_{max} \leq 300\ kN$				$P_{max} \leq 300\ kN$		
1	0.009	0.999	0.398	14	0.000	0.632	0.071
4	0.000	0.027	0.001	18	0.000	0.712	0.169
11	0.000	0. 650	0.146	24	0.000	0.074	0.005
	$P_{max} \leq 350\ kN$				$P_{max} \leq 350\ kN$		
1	0.221	1	0.705	14	0.000	0.647	0.014
4	0.000	0.080	0.006	18	0.014	1	0.469
11	0.000	0.966	0.301	24	0.000	0.619	0.043

8.4 EBDO results of externally stiffened crush tubes

The EBDO formulation for the stiffened tubes under material uncertainty and specific bounds on Pmax and plausibility are formulated as

$$\begin{aligned} &Maximize && f = SEA(S,d,t) \\ &s.t && Pl\{P_{max}(S,d,t) \leq 250\} \geq 0.03 \\ & && 25 \leq S \leq 50 \\ & && 0 \leq d \leq 3, 1 \leq t \leq 2.6 \end{aligned} \tag{8.6}$$

$$
\begin{aligned}
&Maximize && f = SEA(S,d,t) \\
&s.t && Pl\_dec\{P_{max}(S,d,t) \le 250\} \ge 0.03 \\
& && 25 \le S \le 50 \\
& && 0 \le d \le 3 \\
& && 1 \le t \le 2.6
\end{aligned}
\tag{8.7}
$$

Where the evidence-based constraints in Eqs. (8.6) and (8.7) are expressed by plausibility and plausibility decision function, respectively. The desired space for design of optimum stiffened tube in these equations is $P_{max}(S,d,t) \le 250\,kN$. With assessment of evidence-based constraint for the selected designs points 1, 4, 11, 14, 18 and 24 given by Table 8.11, it is possible to establish mathematical formulations relating design variables to these constraints using RBF metamodels. Inverse multiquadratic formulations with c = 0.45 and 0.75 are found to provide best fits for the evidence-based constraints of Eqs. (8.6) and (8.7), respectively. Evaluation of error metrics for the constructed metamodels of Eqs. (8.6) and (8.7) results in PRESS of 0.1191 and 0.0009 and $R^2_{prediction}$ of 0.7786 and 0.9476, respectively. This indicates the acceptable accuracy of these metamodels.

Due to the availability of analytical surrogate models for objective function and evidence-based design constraints and a relatively small set of design variables, we used GA (in Global Optimization toolbox of MATLAB) to setup and solve the optimization problems. A stochastic search approach such as GA offers a viable strategy to explore different regions of the design space in search of the global optimum design point. First, a random population of 20 design points is selected based on the specified bounds on the design variables. The scattered cross-over fraction is set at 0.8, and constraint dependent option is adopted for mutation function.

For linearly constrained optimization problems, the GA solver in MATLAB identifies active linear constraints and bounds to generate search directions, or mutants for the GA. For non-linearly constrained optimization problems that are the case for the

EBDO Eqs. (8.6) and (8.7), it formulates a subproblem subject to linear constraints and bounds using penalty and Lagrange parameters. Once an approximate solution to the subproblem is found, the penalty and Lagrange parameters are updated for a new subproblem, and the solution process continues until convergence at a specified accuracy is reached.

Here, the solution of EBDO problems requires 12 integrations with results given in Table 8.12. These solutions suggest the optimized geometric design of stiffened tubes for maximized *SEA* while providing the confidence that the peak loads do not exceed the critical value of 250 kN by the plausibility of 0.65 for Eq. (8.6) or plausibility decision of 0.003 for Eq. (8.7).

Table 8.12 EBDO solution for externally stiffened tubes

Equation No.	Pl^c	Pl_dec^c	SEA (kJ/kg)	Optimal Design Variables			
				t (mm)	d (mm)	S (mm)	w (mm)
6.6	0.65	-	52.72	2.47	0.15	29.80	16.83
6.7	-	0.03	56.33	2.52	0.31	25.50	20.42

8.5 Evidence-Based Field Uncertainty modeling of stiffened Tubes

Besides the random nature of material properties, their tendency to vary spatially across the structure (material field uncertainty) due to the manufacturing process or history effects can significantly influence the structural behavior. Random field theory has been used in the previous investigations (Xiaolei et al, 2009; Choi et al, 2007) to model material field uncertainty emanating from variability in the material microstructure in different locations of a structural component. In such investigations, the material model is kept the same from one location to another while the information related to the microstructural parameters are allowed to change according to a specified random field

description. The research results indicate the significant influence of microstructure variability on damage and structural failure.

In addition, there are various sources of vagueness (epistemic uncertainty) in determination of material constants of plasticity models that are the key in simulation of dynamic material behavior of structures under extreme loading condition. Depending upon the testing machine, the data acquisition system, associated measurement errors, material samples that can be collected from different regions of a component, the resulting data may show different stress-strain responses that are used to derive the material constants. Other sources of epistemic uncertainty include vagueness in the procedure to determine material constants from experimental stress-strain curves. In fact, depending on the selected initial point in the numerical procedure, the selected random data points in different regions of experimental stress-strain curves, the selected stress-strain curves covering a range of strain rates and temperatures, and the selected numerical method of fitting, the estimated material constants may be different.

Based on the capability of evidence theory to model both epistemic and aleatory uncertainties, it is adopted here to capture the inherent randomness in the material as well as the incertitude in material behavior in describing material field uncertainty in components that undergo large plastic deformation.

As a way of demonstrating the overall approach, an isotropic-elastic-plastic plasticity model is used to establish a relationship between material uncertainty and structural responses. Material uncertainty is viewed in terms of the uncertainty in the model parameters of the adopted plasticity model. To demonstrate the application of the presented evidence-based field uncertainty modeling approach, we focus on design optimization of externally stiffened tubes in Fig. 8.1 with consideration of material

uncertainties. Because of machining effects, the thin-walled sections may follow different material properties, and this indicates the significance of material field uncertainty consideration in design of stiffened crush tubes.

Here, an isotropic-elastic-plastic material model (Material Model 012 in LS-DYNA) is adopted in all nonlinear FE simulations to predict the collapse behavior and structural response of stiffened tubes under axial impact load. The material model includes two material parameters that can be determined from an experimental stress-strain curve. The first unknown parameter is yield stress of the material and the second unknown parameter is the plastic hardening modulus of the material to account for stain hardening effects.

However, determination of these unknown parameters is subject to epistemic uncertainty, and this could impact the tube crush simulation results. Depending upon the testing machine, the data acquisition system, associated measurement errors, and material samples that can be collected from different regions of the crush tube, the resulting data may show different stress-strain responses that are used to derive the material parameters. Also, the stress-strain curve can be selected from a range of strain rates and temperatures, and it is not obvious which curve provides the most realistic behavior of material in stiffened tubes under axial impact load. The plastic hardening modulus can be measured by a tangent to the stress-strain curve at the point where strain hardening commences, and this involves uncertainties and errors.

To consider such sources of material uncertainty in design of stiffened crush tubes, we consider a number of stress-stain curves for AISI Steel 4340. These curves cover a range of temperatures and strain rates and are obtained by using different experimental approaches. Based on the collected information, the yield stress and plastic

hardening modulus are found to be those shown in Table 8.13. Note that each derived set of material parameters in Table 8.13 represents a piece of evidence that will be used in representation of material uncertainty as discussed in the next section.

Table 8.13 Possible values of material parameters of the adopted isotropic-elastic-plastic material model from different stress-strain curves

Curve No	Strain Rate s^{-1}	Temperature (K)	Yield Stress (MPa)	Plastic Hardening Modulus (MPa)
1	0.1	293	830	615
2	1.1	293	884	625
3	117	293	1147	658
4	32	293	905	627
5	0.009	293	824	596
6	0.0004	293	805	570
7	4	293	897	631
8	604	494	757	420
9	650	733	754	460
10	2000	873	841	410
11	1500	673	1207	545
12	1500	473	1422	563

Once again, we performed nonlinear FE simulations of the stiffened tube impacted by a mass of 150 kg moving at an initial velocity of 40 m/s. Isotropic-Elastic-Plastic material model (Material Model 012 in LS-DYNA) is adopted in all simulations while material parameters in each simulation take different values provided by different curves in Table 8.13.

The final collapse shape of three samples using different material parameters is shown in Fig. 8.7 (a) through (c). While material parameters of samples (a) and (b) are assumed to be uniform taking the values provided by curves number 3 and 8 in Table 8.13, respectively, they are assumed to be non-uniform in sample (c). In fact, sample (c) is considered to be affected by material field uncertainty as a result of machining of its three different areas. Top, middle and bottom machined thin-walled sections of this

sample are assumed to take the material parameters provided by curves number 8, 4 and 3 in Table 8.13, respectively while the un-machined areas (rings) are considered to take material parameters of curve number 3. The observed different collapse shapes of the same tube using different material parameters, as shown by Figure 8.7, reveals the significance of material uncertainty consideration in design of stiffened tubes.

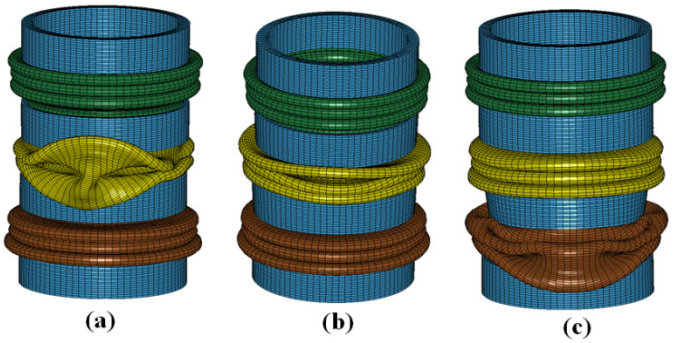

Figure 8.7 Collapse shapes of the same stiffened tube with different material parameters

Here, the aim is to solve the EBDO problem with consideration of material field uncertainties. This problem seeks to maximize SEA (specific energy absorption) while keeping the maximum crush force less than its critical value P_{max}^{C}, and is formulated as

$$\begin{aligned} \max \quad & f(\boldsymbol{X},\boldsymbol{Y}) = SEA \\ \text{s.t.} \quad & Pl\{P_{max}(\boldsymbol{X},\boldsymbol{Y}) \le P_{max}^{c}\} \ge Pl_a \\ & X_k^l \le X_k \le X_k^u; k = 1,3 \end{aligned} \tag{8.8}$$

where $\boldsymbol{X}$ is the vector of design variables defining the geometric attributes of the stiffened tube (i.e., *S*, *d*, *t*). The evidence-based design constraint in Eq. (8.8) imposes a limit on plausibility that P_{max} does not exceed its critical value (P_{max}^{C}) due to the material uncertainty present in the system and denoted by $\boldsymbol{Y}$. Note that depending on the desired level of reliability, Pl_a can take a different value.

To limit the scope of analysis and optimization, the number of external stiffeners is held fixed at four. This reduces the number of geometric design parameters to three since *w* is related to *S* by Eq. (8.1). Based on the geometric relationships noted earlier, the following side constraints for geometric parameters are considered in Eq. (8.8).

$$1 \leq t \leq 2.6;\ 0 \leq d \leq 3;\ 40 \leq S \leq 80 \tag{8.9}$$

Surrogate models based on RBF are developed for use in approximation of response functions that are non-deterministic. The procedure is described in the following section.

8.5.1 Evidence-based uncertainty modeling procedure

Evaluation of $Pl\{P_{max}(\boldsymbol{X},\boldsymbol{Y}) \leq P_{max}^{C}\}$ as well as non-deterministic evidence-based objective function in Eq.(8.8) for stiffened tubes with different geometric parameters require propagation of a field joint belief structure of material parameters, accommodating both material field and model uncertainties, for each training point.

8.5.1.1 Uncertainty representation

Separate belief structures for each uncertain material parameter (yield stress and plastic hardening modulus) are constructed. Here, the derived data for material parameters of the Isotropic-Elastic-Plastic plasticity material model (see Table 8.13) reflecting uncertainty in behavior of the AISI 4340 Steel is used as available evidence in the construction of belief structures. Following the procedure explained in Section 8.1, belief structures for material parameters are constructed and given by Table 8.14. As an example, the dataset used to construct a belief structure for yield stress material parameter along with the corresponding belief structure is shown in Figure 8.8.

Table 8.14 Belief structures of material parameters of Isotropic-Elastic-Plastic material model

Interval	Yield Stress (MPa)		Plastic Hardening Modulus (MPa)	
	Range	BBA	Range	BBA
1	[754.0, 976.7]	9/12	[410.0, 575.3]	6/12
2	[754.0, 1422.0]	3/12	[575.3, 658.0]	6/12

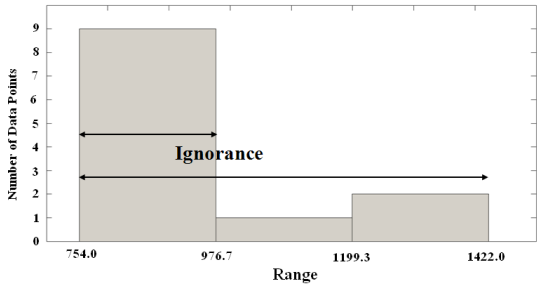

Figure 8.8 Data distribution and the corresponding belief structure for yield stress material parameter

8.5.1.2 Field joint belief structure of material parameters

To consider the combined influence of uncertain material parameters on structural response, a joint belief structure is constructed. Each proposition cell of this joint belief structure is two-dimensional corresponding to yield stress and plastic hardening modulus. The assigned BBA to each joint proposition cell is obtained through multiplication of the BBA of each involved uncertainty interval.

Let sets *A* and *B* denote the constructed belief structures of yield stress and plastic hardening modulus, respectively, and consider a_i and b_j as their uncertainty intervals, where $i, j = 1, 2$. A joint belief structure of material parameters denoted by *C* takes the following form

$$C = A \times B = \{(a_i, b_j) | a_i \in A, b_j \in B\};\ i, j = 1, 2 \tag{8.10}$$

The BBA of each proposition cell of joint belief structure *C* is determined as

$$BBA[(a_i, b_j)] = BBA[a_i] \times BBA[b_j] \tag{8.11}$$

Each proposition cell of C, (a_i, b_j), defines the material properties of the whole product, and assumes that they are uniform. Without consideration of material field uncertainty that is caused by spatial variation of material properties across the whole product due to the manufacturing effects, C can be employed in uncertainty propagation stage. Otherwise, definition of a field joint belief structure that distinguishes between material properties of different regions of the product is necessary.

Here, due to the machining effects on top, middle and bottom regions of the stiffened tubes, it is necessary to consider material field uncertainty effects through construction of a joint field belief structure that make distinction between material properties of machined regions of the structure. The constructed joint field belief structure denoted by D takes the following mathematical form

$$D = C \times C \times C =$$
$$\left\{\left((a_i, b_j)_k, (a_i, b_j)_l, (a_i, b_j)_m\right) \middle| (a_i, b_j)_k, (a_i, b_j)_l, (a_i, b_j)_m \in C\right\};\ k, l, m = 1, 4 \quad (8.12)$$

The BBA of each proposition cells of D is determined as

$$BBA\left[\left((a_i, b_j)_k, (a_i, b_j)_l, (a_i, b_j)_m\right)\right] = BBA\left[(a_i, b_j)_k\right] \times BBA\left[(a_i, b_j)_l\right] \times BBA\left[(a_i, b_j)_m\right] \quad (8.13)$$

Note that in each proposition cell of D, $\left((a_i, b_j)_k, (a_i, b_j)_l, (a_i, b_j)_m\right)$, sub-cells, $(a_i, b_j)_k$, $(a_i, b_j)_l$ and $(a_i, b_j)_m$, define the material properties of the machined top, middle and bottom regions of the stiffened tubes, respectively.

8.5.1.3 Uncertainty propagation

In the context of evidence theory, uncertainty propagation means determination of bounds (intervals) of structural response in each proposition cell of the joint belief structure. Here, the aim is to propagate the constructed joint field belief structure of the

material parameters, D, through nonlinear FE simulations of stiffened tubes impacted by a mass of 150 kg with initial velocity of 40 m/s at different training points sampled within geometric space of the structure.

Unlike the joint probability density function, a joint field belief structure cannot be expressed by an explicit function as it includes a number of disjoint propositions, each of which gives one possible combination of intervals for uncertain variables (see Eq. (8.10)). Propagation of the joint field belief structure requires the evaluation of system response for every combination of uncertain parameter values within each joint proposition with the aim of finding the corresponding bounds of the structural response. Performing a nonlinear FEA for every point within each joint proposition is impractical. To reduce the computational cost, we rely on design and analysis of computer experiments and take the following steps for uncertainty propagation:

1. With the aim to construct surrogate models that relate both geometric parameters as well as material parameters of top, middle and bottom regions of stiffened tubes to structural responses (SEA and P_{max}), the determined geometric space of the structure along with uncertain material parameters space are sampled with an initial set of 30 training points using LHS method.

To make sure accurate surrogate models are obtained, the steps provided by the flowchart in Figure 8.9 are followed. The MATLAB routine lhsdesign and maximin criterion is adopted to select the locations of the training points such that the minimum distance between the design points is maximized, and this makes it possible to add new training points to a previously sampled space if necessary.

We found that by adding 24 training points in two separate stages to the initially sampled space of 30 training points, we can obtain RBF-based surrogate models of

sufficient accuracy. As an example, from this DOE, eight training points that provide different structural responses are selected and are given by Table 8.15. Note that, σ_y^1, σ_y^2 and σ_y^3 in Table 8.15 represent the yield stress of the material in the top, middle and bottom regions of the stiffened tubes, respectively, and $E_{st}^1, E_{st}^2$and E_{st}^3 represent the plastic hardening modulus of the material in the top, middle and bottom regions, respectively.

The corresponding collapse shapes and structural responses of these selected training points derived from nonlinear FEA of stiffened tubes impacted by a mass of 150 kg with initial velocity of 40 m/s are shown by Figure 8.10 and Table 8.16, respectively. The recognized wide range of variations in structural responses of different training points along with their different final collapsed shapes reveals the significant effects of geometric parameters and material properties on energy absorption characteristics of the stiffened tubes. Note that in all FE simulations of different samples, the top, middle and bottom regions of the stiffened tubes follow different material parameters as provided by the training points.

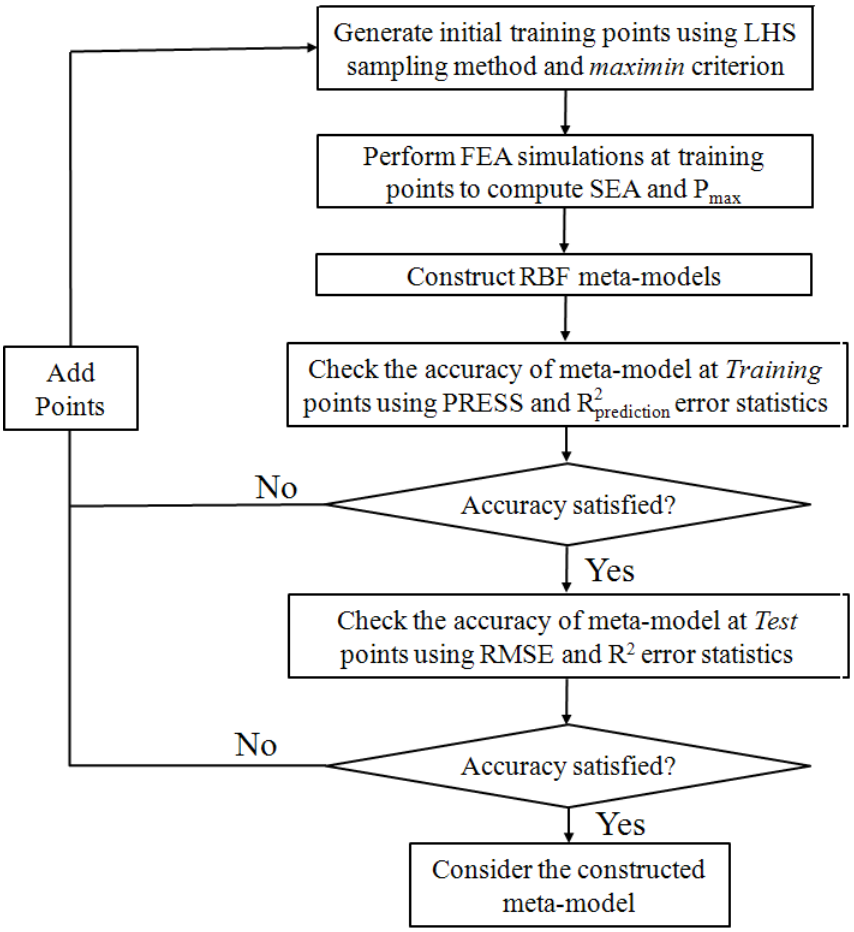

Figure 8.9 Flowchart for constructing accurate RBF metamodels used in uncertainty propagation

Table 8.15 Selected training points sampled within the space of geometric and material parameters

Sample No.	Geometric Parameters			Material Properties					
	t (mm)	d (mm)	S (mm)	σ_y^1 (MPa)	E_{st}^1 (MPa)	σ_y^2 (MPa)	E_{st}^2 (MPa)	σ_y^3 (MPa)	E_{st}^3 (MPa)
1	1.09	2.44	79.12	1119.02	426.47	1243.77	568.69	833.86	495.93
2	2.58	0.52	67.73	860.59	532.31	1217.04	654.69	1074.46	479.39
3	1.53	2.64	74.13	1270.51	608.38	1003.17	439.70	1252.68	562.08
4	1.24	0.92	67.20	1003.17	502.54	994.26	658.00	1110.11	601.77
5	1.68	2.72	77.33	753.66	575.31	1279.42	634.84	1243.78	552.16
6	2.45	2.16	78.40	1083.37	581.92	1065.55	446.31	1092.29	413.24
7	2.39	0.88	70.40	949.70	624.92	1038.82	472.77	816.03	618.30
8	2.15	2.00	76.80	878.41	525.69	1127.93	466.16	1136.84	519.08

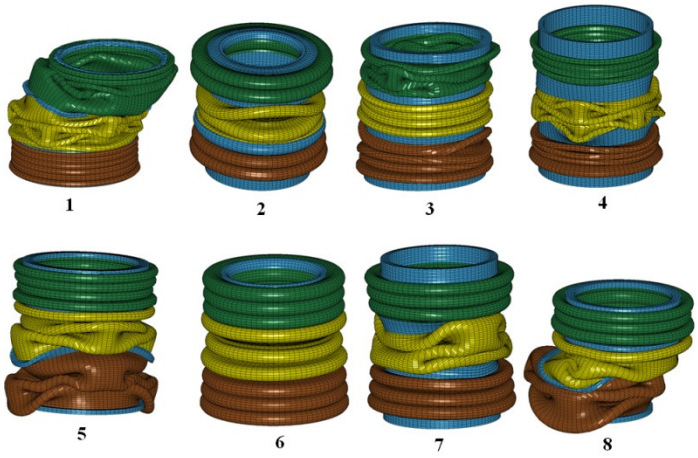

Figure 8.10 Collapsed shapes of the stiffened tube at the selected training points in Table 3

Table 8.16 FE Simulation-based responses at the training points

Sample No.	SEA (kJ/kg)	P_{max} (kN)	P_{mean} (kN)	Stroke Length (mm)	Crush Time (ms)
1	36.89	182.38	66.67	194.10	4.65
2	59.56	777.81	290.72	175.71	5.00
3	39.98	323.64	126.07	174.51	4.60
4	32.76	238.04	86.08	166.37	4.34
5	44.19	319.25	140.58	177.27	3.75
6	57.84	479.27	261.35	177.53	5.00
7	48.71	538.58	233.49	167.21	4.61
8	48.16	480.02	188.10	183.00	5.00

2. Assume functions $f(\mathbf{X},\mathbf{Y})$ and $g(\mathbf{X},\mathbf{Y})$ *re*present the constructed surrogate models found in the previous step for *SEA* and P_{max}, respectively, where **X** and **Y** are the vectors of geometric parameters and uncertain material parameters of the stiffened crush tubes. With the aim to determine the bounds (intervals) of structural response corresponding to each proposition cell of the constructed joint field belief structure for each training point sampled only within the geometric space of the structure, the following optimization problems should be solved using a global search optimization method such as GA

$$\begin{aligned} &\text{max and min} && f(\mathbf{X},\mathbf{Y}) \text{ and } g(\mathbf{X},\mathbf{Y}) \\ &\text{s.t} && X_i - x_i = 0;\ \ i = 1,3 \\ & && Y_j^l \le Y_j \le Y_j^u;\ \ j = 1,6 \end{aligned} \tag{8.14}$$

where in the above equations, x_i is the value of geometric parameters at each training point, $Y_j^l \ and \ Y_j^u$ are lower and upper bounds of material parameters in the top, middle and bottom reigns of the stiffened tubes provided by each proposition cell of the constructed field joint belief structure.

Note that the equality constraint in Eq. (8.14) means the problem must be solved for each geometric training point x_i, and the side constraints limit the search of structural response to each joint field proposition cell of the material parameters. Thus, Eq. (8.14) should be solved 64 times (the number of proposition cells of the constructed field joint belief structure) for each of 54 geometric training points generated in the previous step to obtain the propagated belief structures for all of them. Note that the BBA of the determined intervals of structural response is equal to that of joint field proposition cell from which they are obtained. Hence, the propagated belief structures at each geometric training point are constructed, and can be used in the next section to determine the non-deterministic evidence-based values of SEA and constraint function.

With propagation of the material uncertainties at each geometric training point, it is possible to plot the corresponding Cumulative Belief Function (CBF) and Cumulative Plausibility Function (CPF) of $P_{max} \le \mathrm{P}_{\max}^{\mathrm{c}}$. As an example, these diagrams for samples 3 and 6 in Table 8.15 are shown in Figure 8.11.

Such diagrams provide useful information on the confidence level of uncertainty quantification results of an engineering system with imprecise information. In fact, the gap between CPF and CBF is the indicative of epistemic uncertainty in the system, and can be reduced through acquisition of more knowledge and information. The belief and

plausibility of $P_{max} \leq P_{max}^{c}$ in Figure 8.11 are determined through adding the BBA of intervals in the obtained propagated belief structure that is covered and intersected by the limited space of P_{max}, respectively. Note that in this case, $0 \leq P_{max} \leq P_{max}^{c}$ is the target set and its belief and plausibility should be determined. Here, based on design requirements of stiffened tubes, we consider the value of 300 kN for P_{max}^{c} and evaluate $Pl\{P_{max} \leq 300 \text{ kN}\}$ at each geometric sampling points using the derived the graphs in Figure 8.11. With determination of the evidence-based constraint values at each geometric sampling point, RBF-based surrogate models whose accuracies are checked at both the training and test point are developed to construct a mathematical formulation for the constraint function.

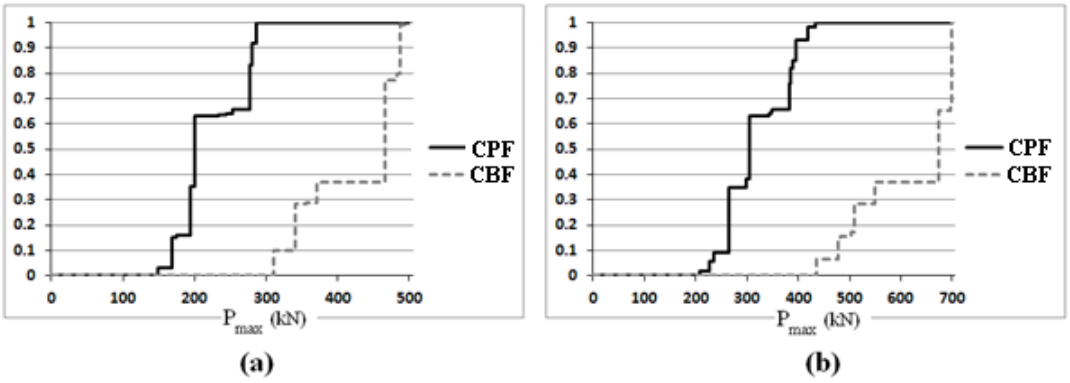

Figure 8.11 CBF and CPF plots of $P_{max} \leq P_{max}^{c}$ for samples (a) 3 and (b) 6

8.5.1.4 Construction of the EBDO formulations and optimization results

The average of the obtained propagated belief structure for *SEA* at each geometric training point is considered as the non-deterministic evidence-based value of the objective function . Suppose the belief structure *M* includes *n* uncertainty intervals $[a_i, b_i]$ with BBA of m_i. The average of this belief structure $\mu(M)$, can be determined by the following equation

$$\mu(M) = \sum_{i=1}^{n} m_i \left(\frac{a_i + b_i}{2}\right) \tag{8.15}$$

where $\left(\frac{a_i + b_i}{2}\right)$ corresponds to the average of interval $[a_i, b_i]$.

Again, with determination of the evidence-based objective function value at each geometric sampling point, an RBF surrogate model is developed for mathematical representation of the objective function.

Following the completion of surrogate models for the objective and constraint functions, the EBDO problem in Eq. (8.8) can be solved. Effectively, the non-deterministic EBDO problem based on material model uncertainty is converted into a representative deterministic optimization problem with the effect of material uncertainty built into the surrogate models used for the calculation of the evidence-based constraint. This problem can be formulated as

$$\begin{aligned} \max \quad & f(\boldsymbol{X}) = \mu(\mathrm{M}) \\ \text{s.t.} \quad & g(\boldsymbol{X}) = Pl\{P_{max}(\boldsymbol{X}, \boldsymbol{Y}) \leq 300\} \geq Pl_a \\ & 1 \leq t \leq 2.6;\ 0 \leq d \leq 3;\ 40 \leq S \leq 80 \end{aligned} \tag{8. 16}$$

where *M* represents the propagated belief structure of *SEA* at geometric training points, and $\mu(\mathrm{M})$ denotes the average of this propagated belief structure.

Due to the availability of analytical surrogate models for the objective function and the evidence-based design constraint as well as a small set of design variables, we used GA in Global Optimization toolbox of MATLAB to setup and solve the EBDO problem defined by Eq. (8.15) with consideration of different values of reliability factor Pl_a (0.6, 0.7 and 0.8).

A stochastic search approach such as GA offers a viable strategy to explore different regions of the design space in search of the global optimum design point. First, a random population of 20 design points is selected based on the specified bounds on the design variables. The scattered cross-over fraction is set at 0.8, and constraint dependent

option is adopted for mutation function. For linearly constrained optimization problems, the GA solver in MATLAB identifies active linear constraints and bounds to generate search directions, or mutants for the GA. For non-linearly constrained optimization problems such as the EBDO problems in Eq. (8.16), it formulates a sub-problem subject to a linear set of constraints and bounds using penalty and Lagrange parameters. Once an approximate solution to the sub-problem is found, the penalty and Lagrange parameters are updated for a new sub-problem, and the solution process continues until convergence at a specified accuracy is reached.

Here, the solution of the EBDO problems requires 72 iterations with results given in Table 8.17. For the first problem, the plausibility constraint is under an upper bound of 0.6 whereas for the second and third problems, it is under the bounds of 0.7 and 0.8, respectively. These solutions represent the optimized geometric design of AISI 4340 externally stiffened circular tubes for maximized *SEA* under uncertainty in material parameters of an Isotropic-Elastic-Plastic plasticity model while meeting the requirement that the peak load does not exceed the critical value of 300 kN with different values of reliability factor.

The results in Table 8.17 reveal that EBDO problems with higher values of reliability factors yield lower values of optimal *SEA*.

Table 8.17 EBDO solutions for externally stiffened tubes under material uncertainty

Reliability Factor, Pl_a	SEA (kJ/kg)	Optimal Design Variables			
		t (mm)	*d* (mm)	*S* (mm)	*w* (mm)
0.6	65.76	2.56	2.04	75.73	3.20
0.7	59.30	2.02	1.20	77.87	1.60
0.8	47.82	1.28	1.12	74.67	4.00

CHAPTER IX

CONCLUSION AND FUTURE WORK

This dissertation sought to apply the mathematical tools of evidence theory to quantify both epistemic and aleatory uncertainties embedded in plasticity models. The evidential uncertainty quantification framework was employed for optimization of structures with consideration of all sources of material uncertainty. Based on the results of this research, the following conclusions can be drawn:

- Evidence theory provides an appropriate mathematical tool to consider both epistemic and aleatory uncertainties involved in an engineering or a physical system.
- Identification of the relationship types (agreement, conflict and ignorance) between adjacent intervals of uncertainty and their consideration in development of a belief structure is the key for accurate representation of parametric uncertainty.
- Since in evidence theory, the joint belief structure of uncertain variables is defined in a discrete space, employment of surrogate models is a major step to reduce the heavy computational cost associated with the uncertainty propagation process.
- Construction of a joint field belief structure that describes representation of uncertainty in different regions of a product can effectively consider spatial variation of uncertain variables in an evidential uncertainty quantification procedure. However, propagation of a joint field belief structure is very computationally expensive.
- The measured large gap between belief and plausibility of both Johnson-Cook and BCJ plasticity models indicates the presence of epistemic uncertainty. However, the

estimated large value of plausibility for both BCJ and Johnson-Cook plasticity models indicates the validity of these plasticity models in simulation of large deformation processes.

- Application of surrogate models is inevitable in evidence based design optimization (EBDO) of structures to reduce the high computational costs.

The presented methodology for uncertainty quantification and optimization of structures under uncertainty can be adopted in the following way as future work:

- It can be adopted in concurrent design of material and product system through decoupling of different scales.
- For more realistic application of the presented approach, the computational cost of uncertainty propagation and design optimization under uncertainty should be reduced.

REFERENCES

1. Alghamdi, A.A.A., "Collapsible impact energy absorbers: An overview," *Thin Walled Structures*,Vol. 39, pp. 189–213, 2001.

2. Acar, E., Rais-Rohani, M., and Eamon, C., "Structural Reliability Analysis using Dimension Reduction and Extended Generalized Lambda Distribution," *International Journal of Reliability and Safety*, Vol. 4, Nos. 2/3, pp. 166-187, 2010.

3. Acar, E., Solanki, K., Rais-Rohani, M., and Horstemeyer, M., "Stochastic Uncertainty Analysis of Damage Evolution Computed Through Microstructure-Property Relations," *Journal of Probabilistic Mechanics*, Vol. 25, No. 2, pp. 198-205, 2010.

4. Acar, E., Rais-Rohani, M., Najafi, A., Marin, E., and Bammann, D., "Concurrent Design of Product-Material Systems using Multilevel Optimization," Proceedings of the 5th AIAA Multidisciplinary Design Optimization Specialist Conference, Palm Springs, CA, May 4-7, 2009.

5. Agarwal, H., Renaud, J.E., Preston, E.L., and Padmanabhan, D., "Uncertainty Quantification Using Evidence Theory in Multidisciplinary Design Optimization," *Reliability Engineering and System Safety*, Vol. 85, pp. 281-294, 2004.

6. Alyanak, E., Grandhi, R., and Bae, H.R., "Gradient Projection for Reliability-Based Design Optimization Using Evidence Theory," *Engineering Optimization*, Vol. 40, No. 10, pp. 923-935, 2008.

7. Bae, H., Grandhi, R.V., Canfield, R.A., "Epistemic Uncertainty Quantification Techniques Including Evidence Theory for Large-Scale Structures," *Computers and Structures*, Vol. 82, pp. 1101–1112, 2004.

8. Bae, H., Grandhi, R.V., Canfield, R.A., "An Approximation Approach for Uncertainty Quantification Using Evidence Theory," *Reliability Engineering and System Safety*, Vol. 86, pp. 215–225, 2004a.

9. Bae, H., Grandhi, R.V., Canfield, R.A., "Sensitivity Analysis of Structural Response Uncertainty Propagation Using Evidence Theory," *Structural and Multidisciplinary Optimization*, Vol. 31, No. 4, pp. 270-279, 2006.

10. Bammann, D.J., "An Internal Variable Model of Viscoplasticity, *International Journal of Engineering Science*, Vol. 22, pp. 1041-1053, 1984.

11. Bammann, D.J., Chiesa, M.L., Horstemeyer, M.F., and Weingarten, L.I., Failure in ductile materials using finite element methods, *Structural Crashworthiness and Failure*, edited by T. Wierzbicki and N. Jones, Elsevier Applied Science, The Universities Press (Belfast) Ltd., 1993.

12. Bammann, D.J., Chiesa, M.L., and Johnson, G.C., "Modeling Large Deformation and Failure in Manufacturing Processes," *Theoretical and Applied Mechanics*, T. Tatsumi, E. Wannabe, and T. Kambe (Eds), Elsevier Science, pp. 359-376, 1996.

13. Beynon, M., Curry, B., Morgan, P., "The Dempster-Shafer Theory of Evidence: An Alternative Approach to Multicriteria Decision Making," *International Journal of Management Science*, Vol. 28, pp. 37-50, 2000.

14. Brown, A.A., Bammann, D.J., Chiesa, M.L., Winters, W.S., Ortega, A.R., Antoun, B.A., and Yang, N.Y.C., "Modeling Static and Dynamic Recrystallization in FCC Metals", Proceeding of International Journal of Plasticity Conference, Halifax, Nova Scotia, Canada, July 17-22, 2006.

15. Chappel, D., "Enterprise Service Bus: Theory and Practice," O'Reilly Media, 2004.

16. Choi, K.K., Du, L., and Youn, B.D., "A New Fuzzy Analysis Method for Possibility-Based Design Optimization," Proceedings of the 10th AIAA/ISSMO Multidisciplinary Analysis and Optimization Conference, Albany, NY, Aug 30-Sep 1, 2004.

17. Choi, S. K., Fathianathan, M., and Schaefer, D., "Optimization of Complex Engineered Systems Under Risk and Uncertainty," Proceedings of ASME. 2007 International Design Engineering Technical Conferences and Computers and Information in Engineering Conference, Las Vegas, NV, Sept. 4–7, 2007.

18. Coleman, B. and Gurtin, M., "Thermodynamics with Internal State Variables," *Journal of Chemical Physics*, Vol. 47, pp. 597-613, 1967.

19. Dempster, A.P., "A Generalization of Bayesian Inference," *Journal of the Royal Statistical Society*, Series B, Vol. 30, pp. 205-247, 1968.

20. Dong, W. and Shah, H., "Vertex Method for Computing Functions on Fuzzy Variables," *Fuzzy Set Systems*, Vol. 24, pp. 65-78, 1987.

21. Droguett, E.L. and Mosleh, A, "Bayesian Methodology for Model Uncertainty Using Model Performance Data," *Risk Analysis*,, Vol. 28, pp. 1457-1476, 2008.

22. Du, X. and Chen, W., "Sequential Optimization and Reliability Assessment Method for Efficient Probabilistic Design," *Journal of Mechanical Design*, Vol. 126, No. 2, pp. 225-233, 2004.

23. Edwards, G., "A Bayesian Procedure For Drawing Inference From Random Data," *Reliability Engineering*, Vol. 9, pp. 1-17, 1984.

24. Enevoldsen, I. and Sorensen, J.D., "Reliability-Based Optimization in Structural Engineering," *Structural Safety*, Vol. 15, pp. 169-196, 1994.

25. Fang, H., Rais-Rohani, M., Liu, Z., Horstemeyer, M.F., "A comparative study of metamodeling methods for multi-objective crashworthiness optimization," *Computers and Structures*, Vol. 83, pp. 2121-2136, 2005.

26. Fang, H., Wang, Q., "On the effectiveness of assessing model accuracy at design points for radial basis functions," *Communications in Numerical Methods in Engineering*, Vol. 24, pp. 219-235, 2008.

27. Florence, A.L. and Goodier, J.N., "Dynamic Plastic Buckling of Cylindrical Shells in Sustained Axial Compressive Flow," *Journal of Applied Mechanics*, Vol. 23, pp. 80-86, 1968.

28. Follansbee, P.S., and Kocks, U.F., "A Constitutive Description of the Deformation of Copper Based on the Use of the Mechanical Threshold Stress as an Internal State Variable," *Acta Metall.*, Vol. 36, pp. 81–93, 1988.

29. Frangopol, D.M., "Reliability-Based Optimum Structural Design," Probabilistic Structural Mechanics Handbook, *Theory and Industrial Applications*, edited by Sundararajan, C., Chapman & Hall, 1995.

30. Gottstein, G. and Kocksa, U.F., "Dynamic Recrystallization and Dynamic Recovery in <111> Single Crystals of Nickel and Copper," *Acta Metallurgica*, Vol. 31, pp. 175-188, 1983.

31. Gray, G.T., Chen, S.R., Wright, W., Lopez, M.F., "Constitutive Equations for Annealed metals Under Compression at High Strain Rates and High Temperatures," Los-Alamos National Laboratory, LA-12669-MS, 1994.

32. Guedes Soares, C., "Quantification of Model Uncertainty in Structural Reliability," in Guedes Soares, C., editor, Probabilistic Methods for Structural Design, Kluwer Academic Publishers, Netherlands, pp. 17-38, 1997.

33. Guoa, Y.B., Wena, Q., Horstemeyerb, M.F., "An internal state variable plasticity-based approach to determine dynamic loading history effects on material property in manufacturing processes" *International Journal of Mechanical Science*, Vol. 47, pp. 1423–1441, 2005.

34. Gu, L. and Yang, R.J., "On reliability-based optimisation methods for automotive structures," *International Journal of Materials and Product Technology*, Vol. 25, No.1/2/3pp. 3-26, 2006.

35. Hallquist, J.O., "LS-DYNA 3D: Theoretical Manual," Livermore Software Technology Corporation, Livermore, 1993.

36. He, L.P. and Qu, F.Z., "Possibility and Evidence Theory-Based Design Optimization: An Overview," *Kybernetes*, Vol. 37, No. 9/10, pp. 1322-1330, 2008.

37. Helton, J.C., "Treatment of Uncertainty in Performance Assessments for Complex Systems," *Risk Analysis*, Vol. 14, No. 4, pp. 483–511, 1994.

38. Helton, J.C., "Uncertainty and Sensitivity Analysis in the Presence of Stochastic and Subjective Uncertainty," *Journal of Statistical Computation and Simulation*, Vol. 57, pp. 3-76, 1997.

39. Helton, J.C., Johnson, J.D., and Oberkampf, W.L., "An Exploration of Alternative Approaches to The Representation of Uncertainty in Model Predictions," *Reliability Engineering and System Safety*, Vol. 85, pp. 39–71, 2004.

40. Hoge. K.G., "Influence of strain rate on mechanical properties of 6061-T6 aluminum under uniaxial and biaxial states of stress," *Experimental Mechanic*, Vol. 6, pp. 204-211, 1966.

41. Holmquist, T.J. and Johnson, G.R., "Determination of Constants and Comparison of Results for Various Constitutive Models," *Journal of Physics IV France*, Vol. 1, No. C3, pp. 853- 860, 1991.

42. Holt D.L., Babcock S.G., S.J. Green, C.J. Maiden, "The strain-rate dependence of the flow stress in some Aluminum alloys," *ASMe Transaction Quarterly*, Vol. 60, pp. 152-159,1967.

43. Horstemeyer, M.F., "From Atoms to Autos, A New Design Paradigm Using Microstructure-Property Modeling, Part 1: Monotonic Loading Conditions," Sandia National Laboratories, Rep. No. Sand2000-8662, 2001.

44. Inagaki, T., "Interdependence Between Safety-Control Policy and Multiple-Sensor Schemes via Dempster-Shafer Theory," *IEEE Transactions on Reliability*, Vol. 40, pp. 182-188, 1991.

45. Johnson, G.R. and Cook, W.H., "A Constitutive Model and Data for Metals Subjected to Large Strains, High Strain Rates and High Temperatures," Proceedings of 7th International Symposium on Ballistics, The Hague, The Netherlands, pp. 541–547, 1983.

46. Johnson, G.R. and Cook, W.H., "Fracture Characteristics of Three Metals Subjected to Various Strains, Strain Rates, Temperatures and Pressures, *Engineering Fracture Mechanics, Vol. 21, pp. 31-48,* 1985.

47. Johnson G.R., Holmquist T.J., Test data and computational strength and fracture model constants for 23 materials subjected to large strains, high strain rates, and high temperatures, LA-11463-MS, Los Alamos National Laboratory, 1989.

48. Johnson G.R., Stryk R.A., Holmquist, T. J., Beissel SR. User Instruction for the 1996 Version of the EPIC Code, Alliant Techsystems Inc,1996.

49. Jones, N., Structural Impact. Cambridge Press, Cambridge, UK, 1989.

50. Jordon, J.B. , Horstemeyer, M.F., Solanki, K., Xue, Y., "Damage and stress state influence on the Bauschinger effect in aluminum alloys," Mechanics of Materials, Vol. 39, pp. 920-931, 2007.

51. Karagiozovaa, D., Jones, N., "Dynamic elastic-plastic buckling of circular cylindrical shells under axial impact,"*International Journal of Solids and Structures* ,Vol. 37, pp. 2005-2034, 2000.

52. Klir, G.J., "The Many Faces of Uncertainty," In: Ayyub, B.M. and Gupta, M.M., editors, Uncertainty Modeling and Analysis: Theory and Applications, pp. 3-19, 1994.

53. Konokman, H. E., Çoruh, M., Kayran, A., Computational and experimental study of high-speed impact of metallic Taylor cylinders, *Acta Mechanica*. Vol. 220, pp. 61–85. 2011

54. Lee W., Shyu J., Chiou S., "Effect of strain rate on impact response and dislocation substructure of 6061-T6 Aluminum alloy*," Scripta material*, Vol. 42, pp. 51–56, 2000.

55. Mourelatos, Z.P. and Zhou, Z., "A Design Optimization Method Using Evidence Theory," *Journal of Mechanical Design*, Vol. 128, pp. 901-908, 2006.

56. Marin, E.B., Bammann, D.J., Regueiro, R.A., and Johnson, G.C., "On the Formulation, Parameter Identification and Numerical Integration of the EMMI Model: Plasticity and Isotropic Damage," SAN D2006-0200, Sandia National Laboratories, Jan 2006.

57. Meyers, M.A., Dynamic Behavior of Materials, p. 328, Wiley, New York, 1994.

58. Nikolaidis, E., Chen, S., Cudney, H., Haftka, R.T., and Rosca, R., "Comparison of Probability and Possibility for Design Against Catastrophic Failure Under Uncertainty," *Journal of Mechanical Design*, Vol. 126, No. 3, pp. 386-394, 2004.

59. Nicholas, T., "Material behavior at high strain rates." In: Zukas, J.A. et al., Impact Dynamics, John Wiley, New York, 27–40,1982.

60. Oberkampf, W.L., Helton, J.C., and Sentz, K., "Mathematical Representation of Uncertainty," AIAA Non-Deterministic Approaches Forum, Seattle, WA, Apr 16-19, 2001.

61. Oberkampf, W.L., Helton, J.C., Joslyn, C.A., Wojtkiewicz, S.F., and Ferson, S., "Challenge Problems: Uncertainty in Systems Response Given Uncertain Parameters," *Reliability Engineering and System Safety*, Vol. 85, pp. 11-19, 2004.

62. Oden, T.J., Belytschko, T., Fish, J., Hughes, T.J.R., Johnson, C., Keyes, D., Laub, A., Petzold, L., Srolovitz, D., Yip, S., and Bass, J., "Simulation-Based Engineering Science: Revolutionizing Engineering Science Through Simulation," Report of the NSF Blue Ribbon Panel on Simulation-Based Engineering Sciences, 2006.

63. Park, I. and Grandhi, R., "Quantification of Multiple Types of Uncertainty in Computer Simulation Using Bayesian Model Averaging," 51st AIAA/ASME/ASCE/AHS/ASC Structures, Structural Dynamics, and Materials Conference, Orlando, FL, 12 - 15 Apr 2010.

64. Qu, X. and Haftka, R.T., "Reliability-Based Design Optimization Using Probabilistic Safety Factor," *Structural and Multidisciplinary Optimization*, Vol. 27, No. 5, pp. 314-325, 2004.

65. Rahman, S., and Xu, H., "A Univariate Dimension-Reduction Method for Multi-dimensional Integration in Stochastic Mechanics," *Probabilistic Engineering Mechanics*, Vol. 19, pp. 393-408, 2004.

66. Rais-Rohani, M. and Xie, Q., "Probabilistic Structural Optimization under Reliability, Manufacturability, and Cost Constraints," *AIAA Journal*, Vol. 43, No. 4, pp. 864-873, 2005.

67. Rais-Rohani, M., Solanki, K., Acar, E., and Eamon, C., "Shape and Sizing Optimization of Automotive Structures with Deterministic and Probabilistic Design Constraints," *International Journal of Vehicle Design*, Vol. 54, No. 1, pp. 309-338, 2010.

68. Reynolds, A.P. and Baxter, S.C., Kinematic hardening in a dispersion strengthened aluminum alloy: experiment and modeling, *Materials Science and Engineering A*. Vol. 285, pp. 265–279, 2000.

69. Rule, W.K., "A Numerical Scheme for Extracting Strength Model Coefficients From Taylor Test Data," *International Journal of Impact Engineering*, Vol. 19, No. 9-10, pp. 797-810, 1997.

70. Salehghaffari, S., Tajdari, M., Panahi, M., Mokhtarnezhad, F., Attempts to improve energy absorption characteristics of circular metal tubes subjected to axial loading. *Thin-Walled Structures*,Vol. 48, pp. 379-390, 2010.

71. Salehghaffari, S., Rais-Rohani, M., and Najafi, A., "Analysis and Optimization of Externally Stiffened Crush Tubes," *Thin-Walled Structures*, Vol. 49, pp. 397-408, 2011.

72. Savage, L.J., The Foundations of Statistics, Dover, New York, 1972.

73. Sentz, K. and Ferson, S., "Combination of Evidence in Dempster-Shafer Theory," Sandia Report SAND2002-0835, 2002.

74. Shafer, G., A Mathematical Theory of Evidence, Princeton University Press, Princeton, NJ, 1976.

75. Shirakashi, T., Maekawa, K., and Usui, E., "Flow Stress of Low Carbon Steel at High Temperature and Strain Rate, Part 1: Property of Incremental Strain Method in Impact Compression Test With Rapid Heating and Cooling Systems," *Bulletin of the Japan Society of Precision Engineering*, Vol. 3, pp. 161-166, 1983.

76. Solanki, K.N., Acar, E., Rais-Rohani, M., Horstemeyer, M., and Steele, G., "Product Design Optimization Using Microstructure-Property Relations and Associated Uncertainties," *International Journal of Design Engineering*, Vol. 2, No. 1, pp. 47-79, 2009.

77. Solanki, K.N., Horstemeyer, M.F., Steele, W.G., Hammi, Y., Jordon, J.B., "Calibration, Validation, and Verification Including Uncertainty of a Physically Motivated Internal State Variable Plasticity and Damage Model, *International Journal of Solids and Structures*, Vol. 47 pp. 186–203, 2010.

78. Tu, J., Choi, K.K., and Park, Y.H., "A New Study on Reliability Based Design Optimization," *Journal of Mechanical Design*, Vol. 121, No. 4, pp. 557–564, 1999.

79. Tanner AB, McGinty RD, McDowell DL, "Modeling Temperature and Strain Rate History Effects in OFHC Cu, "International Journal of Plasticity, Vol. 15, pp. 575–603, 1999.

80. Tanaka, K. and Klir., G. J. , "A design condition for incorporating human judgement into monitoring systems." Reliability Engineering and System Safety, Vol. 65, pp. 251-258.

81. .Xiaolei, Y., Sanghoon, L., Wei, C., Wing, K.L., Efficient Random Field Uncertainty Propagation in Design Using Multiscale Analysis, Journal of Mechanical Design, Vol. 131, Issue 2, 2009.

82. Yager, R., "On the Dempster-Shafer Framework and New Combination Rules," Information Sciences, Vol. 41, pp. 93-137, 1987.

83. Yager, R., "Quasi-Associative Operations in the Combination of Evidence," Kybernetes, Vol. 16, pp. 37-41, 1987.

84. Yager, R., Kacprzyk, J., and Fedrizzi, M., "Advances in the Dempster-Shafer Theory of Evidence," Wiley, New York, NY, 1994.

85. Zerilli, F.J. and Armstrong, R.W., "Dislocation-Mechanics-Based Constitutive Relations for Material Dynamics Calculations," *Journal of Applied Physics*, Vol. 61, pp. 1816-1825, 1987.

86. Zhang, R. and Mahadevan, S., "Model Uncertainty and Bayesian Updating in Reliability-Based Inspection," *Structural Safety*, Vol. 22, pp. 145-160, 2000.

87. Zhang, Y., He, X., Liu, Q., and Wen, B., "Reliability-based optimization of automobile components," International Journal of Vehicle Safety, Vol. 1, pp. 52-63, 2005.